Thermalization, diffusion and photoluminescence of statistically-degenerate indirect excitons in coupled quantum wells

Lois Elenid Smallwood

UMI Number: U584877

UMI

Dissertation Publishing

ProQuest

iv

78445

Diolchiadau

Yn gyntaf, hoffwn ddiolch i fy ngoruchwyliwr, Alex Ivanov, sydd wedi rhannu ei wybodaeth gyda mi a rhoi arweiniad i mi dros y tair blynedd a hanner ddiwethaf. Rydw i hefyd yn hynod o ddiolchgar am gael gweithio gyda Leonid Butov a'i gyd-weithwyr ym Mhrifysgol California yn San Diego. Diolch yn arbennig i Aaron Hammack am ei gymorth di-ffael ac am ateb fy holl gwestiynau ynglŷn â'r arbrofion. Yn ogystal, rydw i yn ddiolchgar am drafodaethau gyda Prof. M Kuwata-Gonokami a chymorth cyffredinol gan N Naka and M Matsuya yn ystod fy nghyfnod yn Japan.

Carwn ddiolch i Helen, Dave, Iain, Gustav, Cele a Leonidas am gymorth, cefnogaeth a chyfeillgarwch gwerthfawr tu hwnt. Diolch yn enwedig i Helen am ddarllen fy ngwaith a rhoi sylwadau, i Iain am fy helpu gyda Fortran ac i Gustav am ddatrys llawer o broblemau a gefais gyda Latex. Hoffwn ddatgan fy ngwerthfawrogiad i Cele a Leonidas am eu cymorth hael a pharod gyda'm gwaith ac am amryw o drafodaethau diddorol; roedd yn bleser gweithio yn yr un swyddfa â nhw.

Yn olaf, diolch i fy rhieni am eu cymorth a'u cefnogaeth ar hyd y blynyddoedd.

Acknowledgements

Firstly, I would like to thank my supervisor, Alex Ivanov, who has patiently shared his knowledge with me for the duration of my studies, and given me guidance. I am also very grateful for the fruitful collaboration with Leonid Butov and his group at the University of California, San Diego. Thanks in particular to Aaron Hammack for being extremely helpful and for answering all my questions about the experimental data and procedures. I would also like to thank Prof. M Kuwata-Gonokami for discussions and N Naka and M Matsuya for help during my stay in Japan.

Many thanks to Helen, Dave, Iain, Gustav, Cele and Leonidas for valuable help, support and friendship. Thanks in particular to Helen for reading through my thesis and giving suggestions, to Iain for helping me with Fortran and to Gustav for solving many problems I had with Latex. I'd like to express my gratitude to Cele and Leonidas for help with my work, many interesting discussions, and for providing a pleasant working environment.

Finally, thanks to my parents for their support and encouragement during the last three and a half years.

ABSTRACT

This thesis is a theoretical investigation into the properties of indirect excitons in coupled quantum wells at low lattice temperatures. The relaxational thermodynamics, optical decay and diffusion of the statistically-degenerate excitons are modelled theoretically and numerically.

The excitons' thermalization from an initial energy, $E_i/k_B = 20 - 300\,\mathrm{K}$, to the lattice temperature, $T_b \sim 1\,\mathrm{K}$, is investigated. The exciton optical creation and decay mechanisms are then included, as well as the change in the exciton effective temperature due to these mechanisms. While the optical creation heats the excitons, their optical decay produces an effect called 'recombination heating and cooling', and whether it produces a net cooling or a net heating of the exciton system depends on the exciton effective temperature, T.

The system of excitons is also studied in two dimensions by using a quantum diffusion equation. The excitons are created by a laser pump with a cylindrically-symmetric spatial intensity profile. The created excitons move outwards from the excitation spot by drift and diffusion, and cool down while doing so. They become more optically-active as they cool, creating a ring of photoluminescence around the excitation spot. This ring was also seen in experiments of this kind. Theoretical results are fitted to experimental results, and the diffusion coefficient for exciton concentrations in the range of $0 < n_{2D} < 2.5 \times 10^{10}\,\mathrm{cm}^{-2}$ varies from 0.06 to $\sim 25\,\mathrm{cm}^2/\mathrm{s}$ when $T_b = 1.5\,\mathrm{K}$, and the disorder amplitude in the sample is $U^0 \sim 0.9\,\mathrm{eV}$.

Finally, a novel kind of laser trap used in experiments to spatially confine the excitons is modelled theoretically. While the experiments were carried out at $T_b = 1.5\,\mathrm{K}$ giving an occupation number of the ground state of ~ 8, theoretical simulations show that for a lattice temperature of $T_b = 0.4\,\mathrm{K}$ the occupation number of the ground state is ~ 500. The trap is also modelled as a homogeneous trap, and simulations show that when T_b is decreased further the fraction of excitons in the ground state increases dramatically.

PUBLICATIONS

L E Smallwood and A L Ivanov. Photoluminescence and In-Plane Diffusion of Indirect Excitons. *Phys. stat. sol. (c)*, **2**, 3932 (2005).

A L Ivanov, L E Smallwood, A T Hammack, S Yang, L V Butov and A C Gossard. Photoluminescence and In-Plane Diffusion of Indirect Excitons. *Europhys. Lett.*, **73**, 920 (2006).

A T Hammack, M Griswold, L V Butov, L E Smallwood, A L Ivanov and A C Gossard. Trapping of Cold Excitons in Quantum Well Structures with Laser Light. *Phys. Rev. Lett. (Accepted)*.

PRESENTATIONS

L E Smallwood and A L Ivanov. Thermalization Dynamics of Quantum Well Excitons. *Semiconductor and Integrated Optoelectronics Conference (SIOE)*, Cardiff (14-16 April 2003).

L E Smallwood and A L Ivanov. Optical Evaporation of Statistically-Degenerate Excitons in GaAs Coupled Quantum Wells. *Condensed Matter and Materials Physics Conference (CMMP)*, Warwick (4-7 April 2004).

L E Smallwood and A L Ivanov. Effective Heating of Statistically-Degenerate Quantum Well Excitons due to Optical Evaporation. *First International Conference on Spontaneous Coherence in Excitonic Systems (ICSCE)*, Pittsburgh (25-28 May 2004).

L E Smallwood and A L Ivanov. In-plane Diffusion and Photoluminescence of Indirect Excitons. *5th International Conference on the Physics of Light Matter Coupling in Nanostructures (PLMCN-5)*, Glasgow (8-11 June 2005).

CONTENTS

LIST OF FIGURES

3

1 INTRODUCTION

This thesis is a theoretical investigation into the properties of indirect excitons in coupled quantum wells. There is extensive research being conducted at present into the behaviour of indirect excitons in coupled quantum wells. They are of particular interest because in the low density limit they are bosons, and therefore obey Bose-Einstein statistics. It is for this reason that excitons have been studied as potential candidates for Bose-Einstein condensation. The excitons have a finite lifetime, which can be an obstacle for them to reach low temperatures because they must thermalize before they optically decay.

The exciton properties that are investigated in this thesis include their temperature, distribution in space, optical lifetime and velocity. Their behaviour under various conditions is analysed theoretically.

The theoretical results presented in this thesis are compared with experimental results where possible, and by fitting the theoretical results to the experimental results, values can be found for parameters such as the disorder in the quantum well samples, and the diffusion coefficient of the excitons.

1.1 OVERVIEW

This first chapter contains the background information for the work presented in this thesis. It includes details of the system under study, as well as an introduction to the theoretical description of the system.

Chapter 2 is entitled 'Relaxational Thermodynamics of Quantum Well Excitons'. The first part of the chapter contains a detailed description of the temperature dynamics for a constant concentration of excitons, with derivations of the equations used. The second part of the chapter details the inclusion of the exciton creation pump and optical decay of the excitons, and how these creation and decay processes affect the temperature of excitons.

The third chapter is entitled 'Diffusion of Quantum Well Excitons' and details the movement of excitons. It experimental results taken by Butov *et al.* at the University of California, San Diego. These experiments were all carried out at relatively low temperatures, around 1 K, and feature a laser focused on the sample to create the excitons. The created excitons subsequently move away from the excitation spot, cooling down while doing so. Theoretical results are fitted to the experimental data. The screening of disorder is discussed, as well as the mean-field energy conversion effect, and the suppression of optical decay of excitons due to their velocity.

Chapter 4 is entitled 'Trapping and Possible Bose-Einstein Condensation of Quantum Well Excitons' and is about a novel kind of laser trap that is used to spatially confine the quantum well excitons. Again, theoretical results are compared with experimental results, and an estimate for the occupation number of the ground state is made, as well as predictions for experiments conducted at lower temperatures.

General conclusions on the main results are discussed in Chapter 5.

1.2   EXCITONS

In a semiconductor an electron can be excited from the valence band to the conduction band and still be bound to the hole it left in the valence band. The electron and the hole form a complex which is bound by the Coulomb attraction and called an exciton. The exciton can move through the crystal and transport energy, but does not transport charge because it is electrically neutral. Excitons are unstable because the electron and hole eventually recombine.

In a direct band gap semiconductor, excitons can be created in two ways: (i) by the absorption of a photon with an energy that is less than the band gap energy but sufficient to excite an electron to the excitonic bound state, or (ii) by the absorption
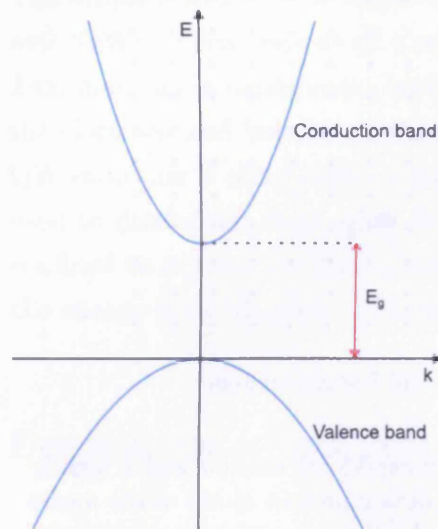
Figure 1.1: Dispersion relations for electrons near the top of the valence band and the bottom of the conduction band, in a direct band gap semiconductor.

of a photon with an energy equal to or larger than the band gap energy, which creates a free electron and a free hole which then relax in energy (usually by the emission of phonons) until they eventually form a bound state. In a direct band gap semiconductor, the minimum energy needed to create a free electron and a free hole is E_g (the band gap energy), see Fig. 1.1.

Excitons exist in many different materials [9–11]. There are two different kinds of excitons, depending on the properties of the material in question. Excitons which are weakly bound, where the attraction between the electron and hole is small in comparison with E_g, are called Wannier-Mott excitons, and extend over many lattice constants (see Fig. 1.2). Wannier-Mott excitons are mainly found in semiconductors, e.g. in gallium arsenide (GaAs), cadmium sulfide (CdS), zinc selenide (ZnSe), copper chloride (CuCl) and cuprous oxide (Cu_2O). The other limiting case is when the exciton is more tightly bound, and is associated with a single atom. These excitons are called Frenkel excitons.

In this thesis the exciton radius is much larger than the inter-atomic distance, therefore it is a Wannier-Mott exciton. When studying these excitons, the discrete structure of the lattice can be disregarded because the exciton Bohr radius, a_B, is much larger than the lattice constant. The parabolic approximation for the electron and hole kinetic energies is valid, and the effect of the lattice potential is incorporated into the effective masses of the electron and hole.

(a) Wannier-Mott exciton.   (b) Frenkel exciton.
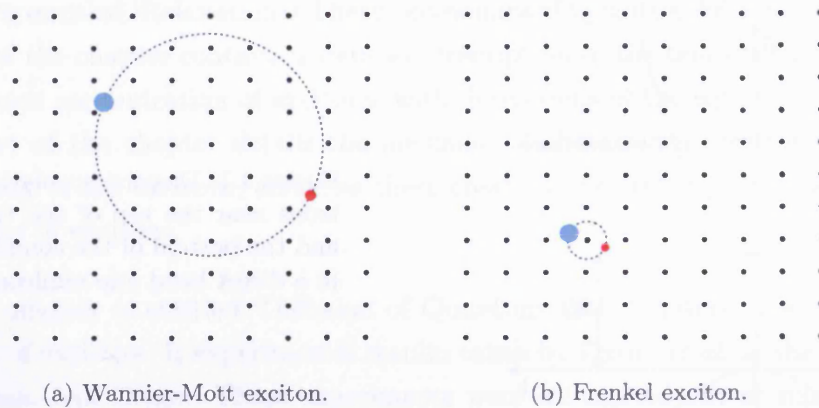
Figure 1.2: A schematic diagram of a free (or Wannier-Mott) exciton and a tightly bound (or Frenkel) exciton, not to scale. The black dots represent atoms of the media they exist in, and the blue and red circles represent the electron and hole respectively.

1.3   QUANTUM WELL EXCITONS

SINGLE QUANTUM WELLS

If the motion of a particle is confined in one direction and the confinement becomes of the order of the particle's de Broglie wavelength, quantum effects begin to dominate the particle's behaviour, and the momentum and energy of the particle in that direction becomes quantised. The particle's motion in the other two dimensions is not affected.
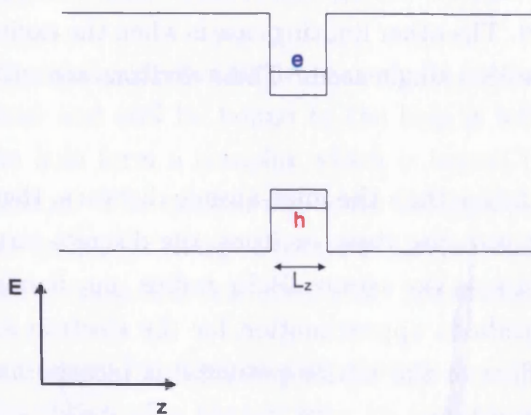
Figure 1.3: Energy band diagram of a single quantum well structure with electron and hole energy levels shown. L_z is the width of the QW.

The simplest structure in which this effect can be observed for excitons is a quantum well (QW), which consists of a very thin ($\sim 10\,$nm) layer of semiconductor material. This material is sandwiched between thicker layers of a wider-gap material, so that the electrons and holes (and therefore the excitons) are contained in the well. This QW structure is often called a 'quasi–two-dimensional' structure. The term 'quasi' is used to distinguish from exact 2D systems in which the wave function is completely confined to a plane *i.e.* has no extension outside the plane. As illustrated in Fig. 1.3, the energy band diagram of a single QW structure has a rectangular shape.

COUPLED QUANTUM WELLS

These structures are similar to single QWs, but consist of two wells, separated by a barrier. The exciton's constituent electron and hole are located in the QWs, but now the electron and hole can be located in different wells. If the electron and hole are in the same well, the exciton is called a 'direct exciton', and if they are in different wells, it is called an 'indirect exciton' (see Fig. 1.4).

(a) No applied electric field.   (b) Electric field applied in the z-direction.
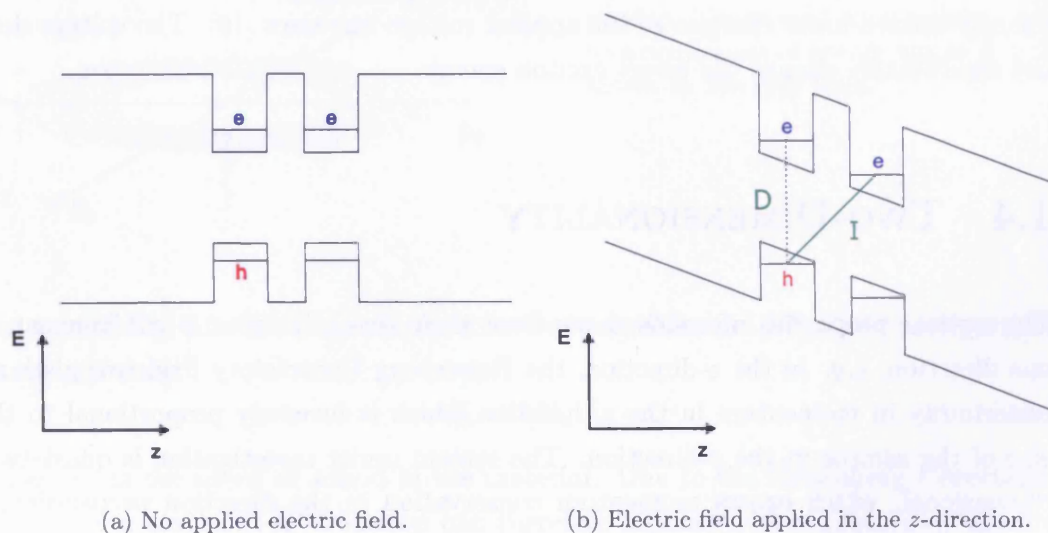
Figure 1.4: Energy band diagrams of a coupled quantum well structure. In (b), the solid line shows how an indirect exciton forms: the electron in the right hand side well binds with the hole in the left hand side well. A direct exciton is a bound electron and hole from the same well, as shown by the dashed line.

Due to the spatial separation of the electron and hole wavefunctions, indirect excitons have a longer radiative lifetime than direct excitons, *i.e.* the electron and hole take a longer time to recombine.

In order to create a greater proportion of indirect excitons a potential difference is applied in the z-direction, controlled in experiments by an external gate voltage, V_g. The resulting effect on the energy band structure is shown in Fig. 1.4(b). For a sufficiently high voltage, the indirect exciton will be the most energy-favourable state [12]. In Fig. 1.4(b), an electron in the left well will tend to tunnel through to the right well, which has a lower potential; and in the same way, a hole will tend to tunnel through and be confined to the left well. Only a small part of the wavefunction of the electron (hole) will still be in the left (right) well. Indirect excitons can have lifetimes of up to three orders of magnitude larger than direct excitons [13–15], and in QWs composed of GaAs, depending on the voltage applied and widths of the wells and barrier, their lifetimes can range from less than 1 ns to a few μs.

The energy of the indirect exciton changes with the applied voltage, V_g, because changing the voltage changes the energy difference between the electron and hole. Above a critical voltage, the indirect exciton energy line in experiments shifts almost linearly toward lower energies as the applied voltage increases [16]. The voltage does not significantly change the direct exciton energy.

1.4 TWO-DIMENSIONALITY

The optical properties of solids depend on their size. If there is confinement in one direction, *e.g.* in the z-direction, the Heisenberg Uncertainty Principle gives an uncertainty in momentum in the z-direction which is inversely proportional to the size of the sample in the z-direction. The system under investigation is quasi–two-dimensional, which causes momentum conservation in the direction perpendicular to the plane of the sample to be relaxed (so if the system lies in the $x - y$ plane, momentum conservation in the z-direction is relaxed).

Excitons interact with 3D ('bulk') phonons. Figure 1.5 is a simple diagram showing how bulk LA phonons interact with the quasi-2D excitons. This will be discussed in detail in Chapter 2.
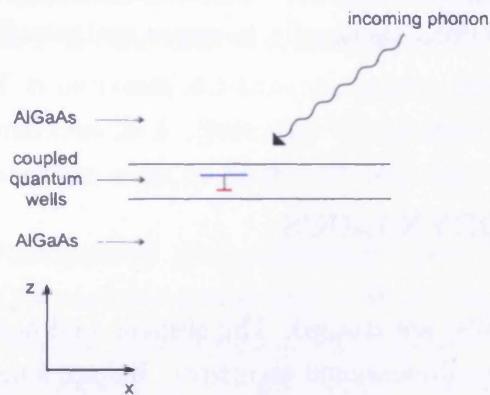
Figure 1.5: A schematic diagram demonstrating how an incoming bulk phonon interacts with a quasi-2D exciton in the QW. The blue disc represents the electron and the red disc represents the hole; their sizes are inversely proportional to their masses.
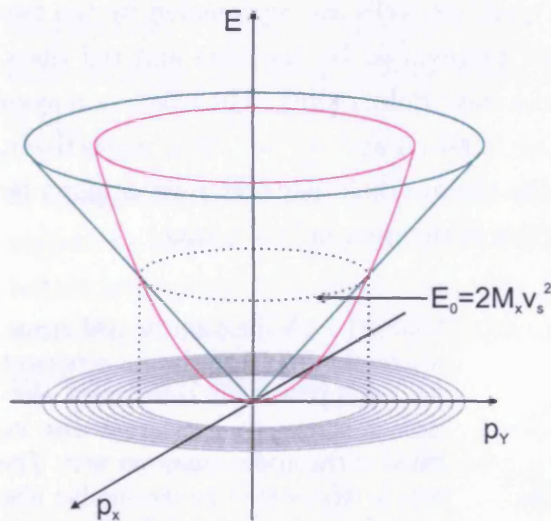
Figure 1.6: A plot of exciton and phonon dispersion relations. The parabolic surface shows excitonic dispersion; the conical surface shows acoustic phonon dispersion. The ground state mode couples to a continuum of energy states $E > E_0$ shown by the grey lines.

As seen in Fig. 1.6, E_0 is the crossover between exciton and LA-phonon dispersions, and is given by

$$E_0 = 2M_x v_S^2, \tag{1.1}$$

where v_S is the speed of sound in the material. Due to the Heisenberg Uncertainty Principle, a scattered QW exciton can therefore interact with a continuum spectral band of scattering LA phonons, $E \geq E_0$, in a given direction, whereas in bulk semiconductors an exciton can couple via Stokes or anti-Stokes scattering with only one phonon mode in a given direction. As a result, the cooling of hot photoexcited excitons down to the temperature of the lattice is generally much more effective for two-dimensional systems, compared with bulk semiconductors. This fast cooling rate and the long radiative lifetime allow excitons to accumulate in the lowest energy

states before they decay; therefore, hot photoexcited excitons can cool down to low temperatures so that the gas of indirect excitons eventually becomes statistically degenerate.

1.5   RELAXATIONAL THERMODYNAMICS

In this thesis, excitons in coupled QWs (CQWs) are studied. The electron and hole move together as a bound complex in the two-dimensional structure. Relaxational thermodynamics, optical decay equations and a quantum diffusion equation are used to model excitons in GaAs/AlGaAs CQWs. A simple diagram of the system in real space is shown in Fig. 1.7, where the quantum wells are represented by the two grey layers, and the electron and hole are represented by the blue and red discs, respectively. The size of the discs represents their Bohr radius. The effective masses of the electron and hole in GaAs are $m_e = 0.067m_0$ and $m_h \sim 0.2m_0$ respectively, where m_0 is the free electron mass, and the electron-hole reduced mass is given by $m_e m_h/(m_e + m_h) = 0.05m_0$. The Bohr radius of the exciton is $\sim 14\,\text{nm}$.
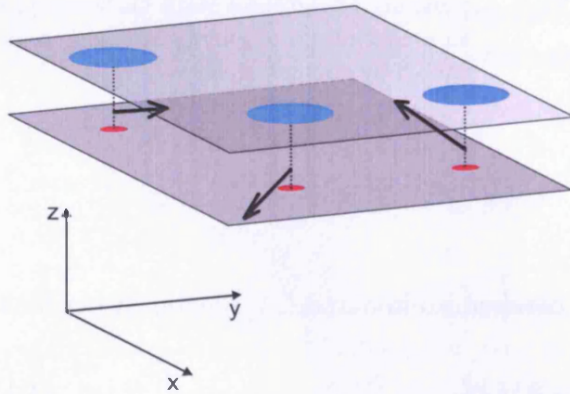
Figure 1.7: A diagram in real space, where the two grey layers represent the two QWs. The constituent electron is shown by the larger disc located in the upper quantum well. The hole is represented by the smaller disc in the lower quantum well. Their sizes are inversely proportional to their masses.

An exciton has integer spin because it consists of two fermions and therefore in the low-density limit is a boson, and obeys Bose-Einstein statistics. The crossover from classical to quantum statistics occurs near the degeneracy temperature T_0, given by

$$k_B T_0 = \frac{2\pi}{g}\left(\frac{\hbar^2}{M_x}\right) n_{2D}, \qquad (1.2)$$

where g is the spin degeneracy factor of quantum well excitons, n_{2D} is the concentration of excitons, M_x is the in-plane translational mass of an exciton and k_B is the

Boltzmann constant. The gas of quantum well excitons is classical at $T \gg T_0$, and as T is decreased and approaches T_0, Bose-Einstein statistics smoothly develop. If T is decreased further, the lowest energy states have large, non-classical occupation numbers $\gg 1$. Note that the exciton mass, M_x, is small, even smaller than the free electron mass, so T_0 is relatively high because it is inversely proportional to M_x.

Relaxational thermodynamics refers to phonon-assisted thermalization kinetics of QW excitons, and is used to study how Bose-Einstein statistics affect the thermalization and photoluminescence of quasi 2D excitons. This approach assumes a hierarchy of interactions: exciton–exciton interaction has to be much stronger than exciton–LA-phonon interaction. The concentration of excitons, n_{2D}, has to be larger than some critical concentration so that the system is able to establish a quasi-equilibrium temperature, T, and the thermalization of the excitons occurs through a series of quasi-equilibrium thermodynamic states. For GaAs QWs, this critical concentration is $n_{2D}^c \sim 1 - 3 \times 10^9 \, \text{cm}^{-2}$ [17].

In Chapter 2, an equation is derived which describes the temperature of excitons with respect to time, $T(t)$, from the initial value $T_i = T(t = 0)$, where $t =$ time, to the lattice temperature T_b (or at least very close to it). This equation deals with the scattering of excitons by bulk LA phonons, where the distribution of the phonons is given by the Planck formula:

$$n_\varepsilon^{\text{ph}} = \frac{1}{e^{\varepsilon E_0 / k_B T_b} - 1} \, .$$

(1.3)

Here ε is the dimensionless phonon energy and is given by $\varepsilon = E/E_0$, where E is the phonon energy. When the excitons are created they can be hot, but the initial distribution of excitons is assumed to be below the threshold where optical phonon scattering becomes the dominant mechanism (which is $\sim 200 \, \text{K}$, and the threshold for optical phonon emission is $\sim 400 \, \text{K}$ in GaAs [18]). The excitons then cool down because the lattice is kept very cold. Instead of treating an approximation of the Boltzmann equation as was done in Ref. [17], a 'microscopic' equation is derived that takes into account all of the excitons in the system. Although this complicates the equations considerably, it should give more accurate results.

Exciton–LA-phonon coupling was researched experimentally by Damen et al. [19], and in Ref. [20] Damen et al. discussed the results of experimental measurements of LA-phonon scattering of hot QW excitons. Piermarocchi et al. made calculations of the photoluminescence rise and decay times, and scattering rates with LA-phonons [21].

1.6 PHOTOLUMINESCENCE

Photoluminescence (PL) emitted during exciton recombination allows the study of excitons in experiments. With an increase in exciton concentration, the position of the exciton line moves to higher energies due to a net repulsive interaction between indirect excitons. This interaction is repulsive because the excitons are oriented in the same direction: electrons are always in one well, and holes in the other. They have a well-defined repulsive interaction potential $\propto 1/r^3$ at distances r from each other, where $r \gg d_z$ and d_z is the distance between the electron and hole layers. This is discussed further in Sections 1.9 and 3.3. Due to energy and momentum conservation laws, the excitons can only decay resonantly and emit PL from the lowest energy states. This is discussed further in Section 1.11. Since only the lowest energy excitons decay, this can give information about the temperature of the excitons in experiments. It also means that their decay affects the effective temperature, T, so in theoretical modelling this has to be taken into account. This is discussed in detail in Section 2.8.

1.7 BOSE-EINSTEIN CONDENSATION IN 3D

Bose-Einstein condensation (BEC) is a macroscopic occupation of the lowest energy state, $E = 0$. A Bose-Einstein condensate forms when a liquid or gas of bosons is cooled below a critical temperature T_c. For a gas of bosons of mass m and concentration n_{3D}, the phase transition to a Bose-Einstein condensed phase occurs when their thermal de-Broglie wavelength becomes comparable to their inter-particle distance [22–24]. For example, BEC takes place when $n_{3D}\lambda_{dB}^3 = 2.612$ in 3D systems, where λ_{dB} is the de Broglie wavelength and is given by $\lambda_{dB} = \sqrt{2\pi\hbar^2/(mk_BT)}$. This is of the order of $n_{3D} \sim 10^{17} \text{cm}^{-3}$ for $T_c \sim 1\,\text{K}$ and m of the order of the electron mass $e.g.$ excitons in bulk Cu_2O.

The possibility of condensation depends on the form of the density of states, d_E. Assuming that the system is in thermal equilibrium at a temperature T and chemical potential μ, then the total number of particles in a box, N, is equal to the sum of the occupation numbers for the single-particle states [25, 26]:

$$N = \sum_{E=0}^{\infty} N_E \qquad (1.4)$$

where E is the energy of a particle and N_E is the occupation number given by the Bose-Einstein distribution function, $N_E = 1/(e^{(E-\mu)/k_B T} - 1)$. In the semi-classical approximation, the spacing between the energy levels of the particle states is assumed to be negligible, so that the sum in Eq. 1.4 can be replaced by an integral:

$$N = \int_0^\infty d_E \, N_E \, \mathrm{d}E \,, \tag{1.5}$$

and in this case the spin degeneracy, g, is not taken into account. Equation 1.5 determines the chemical potential, μ, of the particles. For an ideal noninteracting gas in 3D, the density of states, $d(E) \propto E^{1/2}$. In this case, the integral in Eq. 1.5 is finite and approaches a finite value as μ approaches zero. This implies a critical concentration above which no more particles can be added to the excited states, so that any additional particles must then go into the $E = 0$ state; this is Bose-Einstein condensation.

The condensation temperature, T_c, in a 3D system is given by [27, 28]

$$k_B T_c = 3.31 \frac{\hbar^2}{m} \left(\frac{n_{3D}}{g} \right)^{\frac{2}{3}} \,, \tag{1.6}$$

where m is the mass of the particles, n_{3D} is the concentration of the gas and g is the spin degeneracy factor.

What if the number of particles is finite? This is always the case in real-life experiments. Ketterle and van Druten found that BEC in 3D, in a harmonic potential with a finite number of particles, is very similar to the case of an infinite number of particles, the main difference being the shifted and smeared out onset of the macroscopic occupation of the $E = 0$ state [7]. They showed that the behaviour of a system with finite N (even as small as $N \sim 10^4$) is very similar to a system in the thermodynamic limit ($N = \infty$). A slight lowering of T_c was found for lower N. In experiments, a macroscopic occupation of the $E = 0$ state was regarded as evidence for BEC [29-31].

THE SEARCH FOR BOSE-EINSTEIN CONDENSATION IN 3D

Atomic BEC was first seen in 1995 by Cornell and Wieman's group [29]. The vapour of rubidium atoms was confined by a magnetic field, and cooled by evaporation. In

this evaporative cooling technique, high-energy atoms evaporate leaving only the low-energy atoms in the trap, so that when the remaining atoms re-thermalize there is a net cooling effect [23, 31].

The subject of BEC has been investigated thoroughly [32], and condensation of many elements has been reported, including atoms of cesium [33], potassium [1], hydrogen [34] and lithium [30]. Figure 1.8 shows how BEC of potassium was observed by Modugno *et al.* [1].
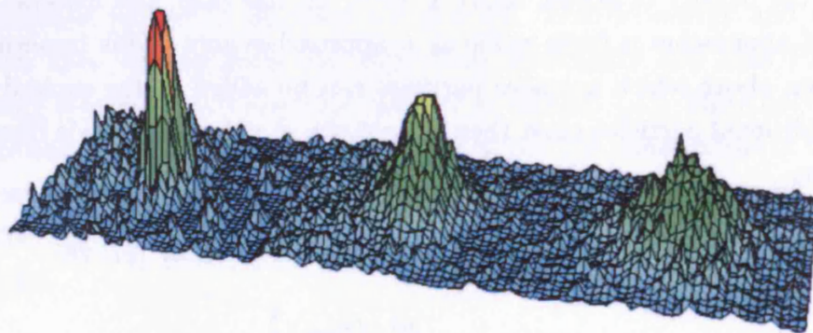
Figure 1.8: Taken from Ref. [1], this shows the density profiles of a potassium cloud after 15 ms of ballistic expansion, across the phase transition to BEC. The increasing height represents an increasing density. From right to left, profiles are as follows: thermal cloud at $T > T_c$; partially condensed sample at $T \approx T_c$; and almost pure condensate at $T < T_c$, containing about 10^4 atoms.

An extensive amount of research has been devoted to the trapping of these atoms, as it is essential to confine the atoms when trying to achieve BEC. Optical trapping (by radiation pressure) was discussed by Ashkin in 1970 [35], where micron-sized particles were trapped in a laser beam. This concept was used in several further experiments *e.g.* in experiments discussed in Ref. [36]. Optical confinement was used by Stamper-Kurn *et al.* [37] to confine a condensate in an optical dipole trap using a single focused infrared laser beam. Magnetic traps have also been widely used, and recently offered more capabilities by becoming much smaller [38].

In 1962, the possibility of the observation of BEC of *excitons* was first considered [39, 40]. In the low-density limit, these excitons are composite Bose quasi-particles, similar to hydrogen atoms. In Ref. [40] Blatt *et al.* concluded that BEC of excitons would be possible, and further investigation into the subject of BEC of excitons was

done in 1968 by Keldysh and Kozlov [41].

Excitons in semiconductors are good candidates for BEC because they should undergo BEC at temperatures much higher than atoms, due to their extremely small translational mass. In fact, the critical temperature for BEC, T_c, is about six orders of magnitude higher for excitons than it is for atoms [42]. Another factor that makes this a promising system for experiments on BEC is the possibility of controlling the exciton density by varying the laser excitation power that creates the excitons.

The past two decades have seen extensive theoretical and experimental research into excitons in bulk semiconductors [43–55], and most of this work was on excitons in bulk Cu_2O. Much of the research focused on the excitons' behaviour at low temperatures, and a significant amount of the work has been dedicated to achieving BEC of excitons in 3D. The experiments conducted dealt mainly with Cu_2O, a material whose exciton ground state is optically dipole-inactive, which means a low exciton radiative recombination rate. Although it seemed that the experimental conditions necessary for BEC in Cu_2O were reasonable, there were some unforseen effects that caused problems. A high Auger recombination rate at high excitation levels reduces exciton densities and heats the exciton gas (in a typical Auger process, two excitons collide, and one exciton gives its band gap energy to the remaining e-h pair). There is much debate on how strongly the Auger processes affect the system and whether Cu_2O is a good candidate for exhibiting BEC or not [50, 56, 57].

1.8   BOSE-EINSTEIN CONDENSATION IN 2D

The density of states of an ideal gas in a 2D box has the form d_E = constant, and in this case the integral in Eq. 1.5 is infinite as μ approaches zero. Therefore the integral does not converge, which means that N has no upper bound; thus there is no temperature below which the ground state is macroscopically occupied in comparison to all the other states. Hence, there is no BEC in the thermodynamic limit in 2D.

The situation above is for infinite systems; in reality, systems are always finite. Although Bose-Einstein condensation is not possible for an infinite 2D system, a kind of a Bose-Einstein condensate can be achieved in finite 2D systems, if a large fraction of particles occupy the $E = 0$ state [26]. The integration in Eq. 1.5 can only be carried out if the separation between the energy levels of the exciton states is negligible, but

when the system is finite and at a low temperature this assumption cannot be made.

In Ref. [58], Bagnato *et al.* stated that 2D systems display BEC in a potential trap for any finite value of κ where the trap potential, $U(x) \sim x^\kappa$, and $\kappa < 2$. In Ref. [7], BEC in 1D, 2D and 3D systems with a finite number of particles was discussed, and Ketterle and van Druten showed that corrections due to the finite number are small (but observable in the case of a 3D harmonic oscillator). They also stated that the number of particles needed to reach BEC is lower in 2D than in 3D. They focused on the harmonic potential because of its relevance to experiments and its mathematical simplicity.

For BEC of noninteracting particles in a harmonic trap in 2D where every energy level is separated by an energy $\hbar\omega$, the fugacity, z, can be found from

$$N = \sum_{j=1}^{\infty} z^j \frac{1}{(1 - x^j)^2} , \tag{1.7}$$

where $x = e^{\hbar\omega/k_{\rm B}T}$, and N is the number of particles in the trap. The BEC temperature is given by

$$k_{\rm B}T_{\rm c} = \frac{\sqrt{6}}{\pi}\hbar\omega\sqrt{\frac{N}{g}} . \tag{1.8}$$

The possibility of condensation in a *homogeneous trap* is discussed in Chapter 4. where optically-induced traps for indirect excitons are discussed.

THE SEARCH FOR BOSE-EINSTEIN CONDENSATION IN 2D

Bose-Einstein condensation of sodium atoms in low dimensions (1D and 2D) was reported on by Gorlitz *et al.*, where the atoms were confined in optical and magnetic traps [59]. There have been theoretical investigations into the possible BEC of atoms in thin films [60], quasi-2D trapped gases [61, 62], ideal gases in 2D [63] and excitons in CQWs. The possibility of BEC of excitons in CQWs is discussed further in this section.

Extensive research, both experimental and theoretical, is being carried out into the possibility of BEC of excitons in coupled QWs. The concentration of excitons can be generated and varied both simply and effectively by using a laser. In addition to

this, their lifetime is long and their cooling is very efficient, which makes this system a favourable one for achieving BEC of excitons.

Many experiments have been conducted to investigate excitons in coupled QWs [3, 42, 64–69]. In one case, excitons in a 2D trap were investigated [42]. The trap was 'natural' *i.e.* it was not created specifically for this purpose, but was present in the sample because of imperfections. Although technology allows the creation of very high quality samples, there are always unavoidable fluctuations in the well and barrier widths. The sample was excited nearly uniformly with a laser, and a strong PL signal was detected at particular locations on the sample. In another experiment the sample was excited non-uniformly, and a strong PL signal was detected at the same locations, even though they were hundreds of micrometers away from the excitation spot. It was deduced that the excitons collected at these locations because they were places of local potential minima.

An observation of a build-up of indirect excitons in a 'lateral potential well', far away from the excitation spot (> 100 µm) was reported on by Larionov *et al.* [16]. This well was constructed by depositing a narrow strip of gold on the mesa surface of the structure. Harmonic-potential traps created by pressing a pin against the 2D structure were used by Negoita *et al.* [70, 71], and they observed an accumulation of excitons in this trap. It was proposed by Zhu *et al.* that an excitonic condensate may form in a CQW structure if the width of one of the wells is slightly larger in a particular area.

Rapaport *et al.* applied a potential across a CQW sample with a small circular optically semitransparent metallic gate, and the bottom substrate was made conductive so as to act as the ground electrode [72]. The indirect excitons in this kind of sample tend to stay in the region under the gate contact when sufficient voltage is applied. A minimum vertical applied electric field is required to overcome dipole-dipole repulsion energy to prevent excitons from escaping. However, the exciton concentration is limited because of the ionisation of excitons at the trap boundaries. This method of trapping was also used by Hammack *et al.* [73], but in this case an evaporative cooling technique was used, so that the most energetic particles overpassed the potential barrier and left the trap. They overcame the problem of ionisation of excitons by placing the CQWs closer to the bottom gate, which made exciton ionisation negligible.

Initial results on exciton localisation in a QW system with an interdigitated gate of small period was published in Ref. [74]. Lateral superlattices as voltage-controlled

traps for excitons were used in experiments discussed in Refs. [75, 76]. Electric-field induced exciton transport was discussed in Ref. [77], where the average drift velocity reached $v_{\text{drift}} = 5 \times 10^3 \, \text{cm/s}$.

The effects of applying a magnetic field to a QW structure have also been investigated over the years. Magnetic fields have been applied either perpendicularly or parallel to the sample, to observe what effect this has on the exciton dynamics [12, 78–85].

More results from experiments on excitons in CQWs are discussed in Section 3.1, where a detailed explanation of particular results is given. These experiments are also modelled theoretically, and the results are compared with experimental results.

1.9   EXPERIMENTS

Where possible, the theoretical work in this thesis is compared with experimental data taken by Butov *et al.* at the University of California, San Diego. Where parameters were previously unknown, they could be estimated by fitting the theory results to the experimental results. The samples used to obtain experimental data are of extremely high quality, but of course not perfect, so interface disorder and localisation effects have to be taken into account when comparing theory with experiments.

In most of the experiments modelled in this thesis, the initial energy of excitons, E_i, is very high compared with the lattice temperature, T_b ($E_i/k_B \sim 200 \, \text{K}$ and $T_b \sim 1 \, \text{K}$), and they need to cool down to the temperature of the lattice before a large number of them can occupy the ground state. There are two main ways of studying the cold exciton 'gas': by conducting a time-resolved experiment (*i.e.* study the excitons after the exciting laser is turned off) or by conducting a spatially-resolved experiment (*i.e.* study the excitons after they have moved away from the excitation spot).

The information that can be obtained directly from typical experiments on excitons in CQWs is the time- and spatially-resolved PL intensity, angle of PL emission and energy of the PL signal (or position of the exciton line). In the experiments discussed in this thesis, the PL signal is collected from a small angle and then integrated. The angle of emission depends on the in-plane velocity of the exciton, so a very small angle ensures that only the lowest-energy excitons are detected. This angle is used in the theoretical model when the PL intensity is calculated so that an accurate comparison

can be made. The emitted PL is detected within an angle, η, from the z-axis.

Since the excitons repel each other, at high densities a mean-field energy arises due to the dipole-dipole repulsion. This causes a blue-shift in the energy of the exciton, which has been reported in several publications. In Ref. [65] Negoita et al. proved that in experiments, this blue-shift, $E_{shift} \propto n_{2D}$, for concentrations in the range of $10^9 < n_{2D} < 10^{12} \, cm^{-2}$. Calculations were made in Ref. [86] for this blue-shift, and the results were compared with experiments. The value deduced by Negoita et al. for the linear blue-shift is about half this calculated value; this could be due to the presence of many free carriers in the experiment. When comparing the calculated results with experiments by Butov et al. [4], very similar results were obtained for the concentration of excitons, where Butov et al. used the plate capacitor formula to calculate the concentration. Therefore, in experiments, the energy of the PL signal depends on the mean-field energy of the excitons, which in turn depends on the concentration of excitons, so that the concentration of excitons can be roughly estimated from the energy of the emitted PL. This is accurate for concentrations in the range of $10^8 \leq n_{2D} \leq 10^{11} \, cm^{-2}$ [87]. This mean-field energy is discussed further in Section 3.3.

1.10   SAMPLES AND PARAMETERS

Figure 1.9 is a simple diagram of the mesa. The GaAs/AlGaAs CQW sample studied consists of two 8 nm GaAs wells separated by a 4 nm $Al_{0.33}Ga_{0.67}As$ barrier. This structure is sandwiched between layers of $Al_{0.33}Ga_{0.67}As$, 200 nm thick ('spacer' layers). Either side of those two layers are heavily n-doped GaAs electrode layers which have an excess number of electrons $\sim 5 \times 10^{17} \, cm^{-3}$. These top (or cap) and bottom layers are 105 and 305 nm thick respectively. An alloy was deposited to form ohmic contacts on these layers. Under the bottom layer is a superlattice (AlAs/GaAs), buffer layer (GaAs) and substrate layer (GaAs).

Some parameters will be the same throughout this thesis, in accordance with experimental values quoted by L. V. Butov and co-workers.

- The well width is $L_z = 8$ nm.

- The distance between the electron and hole layers is $d_z = 11.5$ nm [87, 88] which
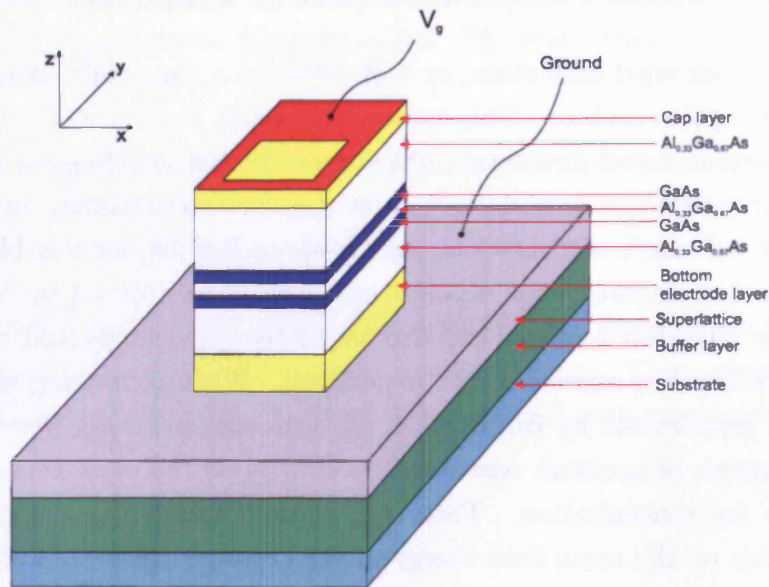
Figure 1.9: A schematic diagram of the structure, not to scale.

is close to 12 nm, the distance between the QW centres.

- The effective mass of the excitons is $M_x = 0.215\,m_0$ [83, 87] where m_0 is the free electron mass; this gives $E_0 = 2M_x v_S = 0.38\,\text{K}$.

- There is a slight uncertainty in the value for the deformation potential, D, in literature, ranging from ~ 7.0 to $15.5\,\text{meV}$ [89–91]. Three different values for D are used in this thesis, $D = 6.5$, 9.6 and $15.5\,\text{eV}$.

- The radiative lifetime of ground state excitons τ_R depends on the applied voltage in the z-direction and lies in the range of $6.75\,\text{ns} < \tau_R < 31.50\,\text{ns}$ in this thesis.

- The degeneracy factor, $g = 4$ [17].

- The sound velocity, $v_S = 3.7 \times 10^5\,\text{cm/s}$ [92].

- The crystal density, $\rho = 5.3\,\text{g/cm}^3$ [93, 94].

- The dielectric constant for GaAs is $\varepsilon_B = 12.9$ [18].
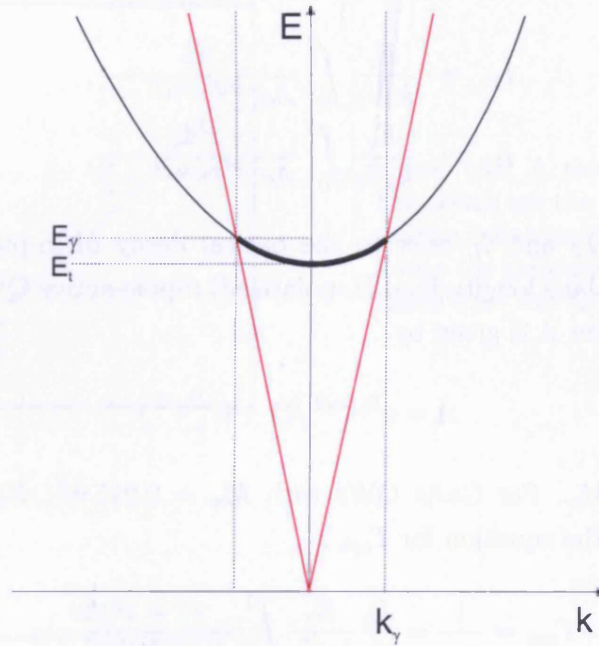
Figure 1.10: A plot of photon and exciton dispersion relations, represented by the red and black lines respectively. The bold part of the exciton dispersion line shows the excitons that can decay resonantly by emitting PL (note that they are the lowest-energy excitons). The crossover between photon and exciton dispersions is shown by k_γ; this corresponds to an energy E_γ.

1.11   OPTICAL DECAY

In perfect QWs a quasi-2D exciton can only emit a bulk photon from radiative modes, which are located inside the photon cone, $k = k(\omega) = (\sqrt{\varepsilon_B}\,\omega)/\hbar c$, where ω is the frequency of the light and ε_B is the background dielectric constant. See Fig. 1.10 to visualize the photon cone. The point where the exciton dispersion crosses the y-axis is given by E_t. The radiative zone of QW excitons is given by $k_\parallel < k_\gamma$ where k_γ corresponds to the photon and exciton dispersions crossing point. The effective radiative decay rate of Bose-Einstein distributed QW excitons is given by [17]

$$\Gamma_{\text{opt}} = \frac{\Gamma_0}{2}[I_{\text{T}}(T, T_0) + I_{\text{L}}(T, T_0)], \qquad (1.9)$$

where

$$I_{\mathrm{T}} = \frac{E_\gamma}{k_\mathrm{B} T_0} \int_0^1 \frac{dz}{Ae^{-z^2 E_\gamma / k_\mathrm{B} T} - 1},$$

$$I_{\mathrm{L}} = \frac{E_\gamma}{k_\mathrm{B} T_0} \int_0^1 \frac{z^2 dz}{Ae^{-z^2 E_\gamma / k_\mathrm{B} T} - 1}, \qquad (1.10)$$

and the integrals I_{T} and I_{L} refer to the optical decay of in-plane transverse (T-polarized) and in-plane longitudinal (L-polarized) dipole-active QW excitons, respectively [95]. The term A is given by

$$A = e^{E_\gamma / k_\mathrm{B} T} / (1 - e^{-T_0/T}) \qquad (1.11)$$

and $E_\gamma = \hbar^2 k_\gamma^2 / 2 M_{\mathrm{x}}$. For GaAs QWs with $M_{\mathrm{x}} = 0.215\, m_0$, $E_\gamma \simeq 141\,\mu\mathrm{eV}$. From Eqs. 1.9 and 1.10, the equation for Γ_{opt} is

$$\Gamma_{\mathrm{opt}} = \frac{1}{\tau_{\mathrm{opt}}} = \frac{\Gamma_0}{2} \frac{E_\gamma}{k_\mathrm{B} T_0} \int_0^1 \frac{(1 + z^2) dz}{Ae^{-z^2 E_\gamma / k_\mathrm{B} T} - 1}. \qquad (1.12)$$

The radiative rate $\Gamma_0 = \Gamma_{\mathrm{T}}(k_{\parallel} = 0) = \Gamma_{\mathrm{L}}(k_{\parallel} = 0)$ for the ground state mode $k_{\parallel} = 0$ determines the intrinsic radiative lifetime τ_{R} of QW excitons, which is $\tau_{\mathrm{R}} = 1/\Gamma_0$. The optical decay of highly-degenerate QW excitons is given by $\tau_{\mathrm{opt}}^{\mathrm{quantum}}(T \to 0) = 2\,\tau_{\mathrm{R}}$ [17]; the factor 2 appears because half of the excitons are dipole-inactive, or 'dark'.

In experiments it is possible to deduce the value of τ_{R} by analysing the decay rate of the PL signal at large delay times and low T_{b} [2, 6, 64]. Since the excitons will be very close to the lattice temperature at large delay times. and $T_{\mathrm{b}} \ll E_\gamma / k_\mathrm{B}$, the optical decay time τ_{opt} saturates and approaches $2\,\tau_{\mathrm{R}}$, which can then be measured; see Fig. 1.11.

Since τ_{R} depends on the applied voltage, V_{g}, for the numerical modelling it is essential to know what τ_{R} is for the voltage used. It is possible to construct a plot of τ_{R} against V_{g}. In the experiments modelled in this thesis, $1.2 < V_{\mathrm{g}} < 1.6\,\mathrm{V}$, and the value of τ_{R} is found from Fig. 1.12.
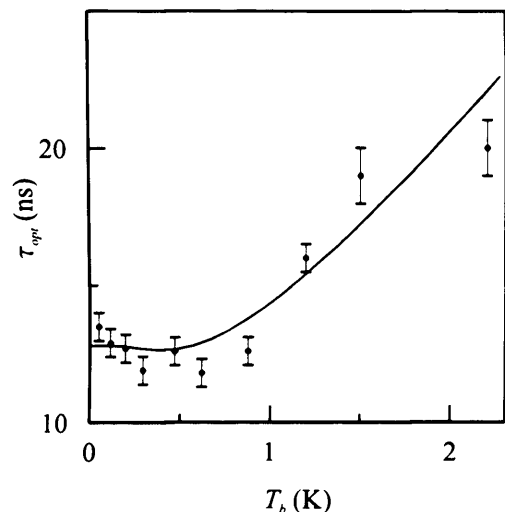
Figure 1.11: A plot of τ_{opt} against T_b. The points are the experimental results, and the line shows the theoretical results. Notice the saturation of τ_{opt} as $T_b \to 0$. Taken from Ref. [2].
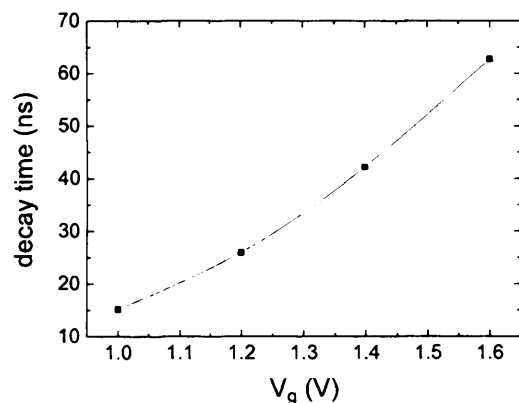
Figure 1.12: The exciton decay time = $2\tau_R$ calculated from experiments against the voltage applied across the whole structure, V_g [3, 4]. The points are experimental data and the line is a guide for the eye.

1.12   THE FORMATION OF EXCITONS

There are two ways of creating an exciton, depending on how much energy the electron obtains; this was mentioned briefly in Section 1.2. If the electron is given enough energy to create an exciton but not enough to become free, it is called a *resonant* creation, also sometimes called 'sub-barrier excitation'. This would mean that the energy the electron receives is below E_g; see Fig. 1.1. If a free electron and free hole are created, which then relax by phonon emission and become a bound pair, it is a *nonresonant* creation. In this thesis, excitons created resonantly and nonresonantly are modelled: in Chapters 2 and 4 only nonresonant creation is used, but in Chapter 3 both mechanisms are used.

RESONANT CREATION

In this case, the excitation energy creates a direct exciton. The generation of indirect excitons is a secondary process, mainly due to quantum tunnelling of the direct excitons to the energetically more favourable states of indirect excitons. There is no significant free carrier generation when resonant excitation is used [96].

NONRESONANT CREATION

If an exciton is created nonresonantly and then relaxes to an indirect exciton, the excess energy E_i of the created indirect exciton is large: it exceeds the energy splitting between the direct and indirect excitons, which is about 20 meV.

A substantial amount of research has been conducted into the creation of excitons from e-h pairs. The formation of an exciton from a free electron and a free hole happens very quickly (on the ps time scale) by LO-phonon emission. At temperatures below $\sim$ 200 K, LA-phonon emission is the most important relaxation mechanism for exciton formation from free e-h pairs [97]. Yoon et $al.$ in Ref. [98] state that carrier cooling due to LO-phonon emission occurs on the subpicosecond timescale, and after this emission, the exciton temperature is of the order of 100 K. Kusano et $al.$ found the formation time to be $\sim$ 190 ps [99], and in Ref. [100] it was deduced from experiments that excitons formed within 20 ps of creation of electron-hole pairs by sub-picosecond optical excitation. Blom et $al.$ studied very narrow GaAs/Al_xGa$_{1-x}$As QWs in which the time for exciton relaxation to the lowest energy states was expected to be small. They measured the exciton formation time to be about 25 − 40 ps for $n_{2D} = 5 \times 10^{10}$ cm^{-2} [101]. Robart et $al.$ stated that the formation time is less than 10 ps for $n_{2D} = 7 \times 10^{10}$ cm^{-2} [102]. In GaAs quantum wells, Kumar et $al.$ deduced an exciton formation time of 50 ps for an initial carrier density of 4×10^{10} cm^{-2} [103].

Thilagam and Singh were the first to calculate the formation time of excitons theoretically as a function of QW width, by considering the formation of excitons by LA-phonon emission [104]. They calculated generation rates of excitons and found the exciton formation time from an e-h pair in single GaAs/AlGaAs QWs to be $\sim$ 0.25 − 1 ns; however, they state that detailed comparison of their theoretical results with experiments may not be possible because of various assumptions involved in the calculations. In Ref. [97], Zhang et $al.$ theoretically investigated the formation

of excitons from an e-h plasma which was created by nonresonant excitation, and calculated a value of 108 ps for the formation of the excitons. More recently, theoretical research by Oh and Singh showed that the rate of formation depends strongly on the temperature of the e-h plasma [105].

Very recently, Szczytko et al. performed experiments and made calculations for the exciton formation time, and reported that it could vary from 10 ps (for a high concentration of carriers) to several of hundreds of ps (for a low concentration of carriers) [106, 107]. However, a lower exciton formation time was found at lower temperatures. They stated that the spread of experimental values for the formation time found in literature is likely to be related to the different experimental conditions.

In this thesis, only the scattering of excitons with LA-phonons is taken into account, which assumes that the initial energy of excitons does not exceed $E_i/k_B \sim 200$ K. At temperatures higher than this LO-phonon scattering becomes an increasingly significant effect.

1.13 DIFFUSION

DIFFUSION IN BULK MATERIALS

It has proven to be quite difficult to see the diffusion of excitons over large distances in both 3D and 2D samples. The main reason for this is the short lifetime of excitons. In 1983, the diffusion constant of paraexcitons in Cu_2O was measured to be 600 cm^2/s at 2 K, by using time-resolved luminescence imaging [108]. Here, the diffusion coefficient was found to be strongly dependent on the temperature of the sample, and it was concluded that exciton-phonon scattering was the dominant scattering mechanism, and that impurity scattering has a very small effect. Note that in this case, the exciton is very small (~ 1 nm), in contrast with excitons in CQWs.

In 1980, measurements were made for the mobility, μ_x, of free excitons in Si by Tamor et al. [109]; the mobility is related to the diffusion coefficient by $\mu_x = D_x/k_B T$. Tamor et al. found a $T^{-3/2}$ temperature dependence for the mobility over a wide range of low temperatures (1.3 − 20 K), well explained by acoustic-phonon scattering. This $T^{-3/2}$ dependence was also verified in 1986 for paraexcitons in Cu_2O [110], where the

diffusion coefficient and drift mobility were also found to be dependent on applied stress.

Diffusion in Quantum Wells

The diffusivity of *electrons* in QWs has been the subject of research for many years [111–115], and in more recent years, so has the diffusivity of *excitons* in QWs [116–124]. In 1990, GaAs/AlGaAs multiple quantum well structures were studied at temperatures between 2.5 and 15 K by Wang *et al.*, and the diffusion coefficient of excitons was estimated to be $D_x \sim 4\,\text{cm}^2/\text{s}$ [116].

Time-resolved imaging of 2D transport of excitons was carried out in microcavities by Yoon *et al.*, where the structure consisted of 30 GaAs wells, 21 nm thick, and 10 nm barriers of $Al_{0.25}Ga_{0.75}As$ [117]. The effective diffusivity was seen to vary from ~ 50 to $300\,\text{cm}^2/\text{s}$ initially to $< 100\,\text{cm}^2/\text{s}$ after 4 ns. The numbers also depended on the excitation power: for higher powers, there was more diffusion. This initial high diffusivity was attributed to the higher carrier temperature generated by large excess energies (excitons were created at $\sim 30\,\text{meV}$ above the hh exciton energy). The motion of direct excitons in GaAs/AlGaAs microcavities was discussed in Ref. [125]: here the fast initial decay (which depended on excitation intensity) was ignored, and the slow exponential decay was studied, where the diffusion coefficient was found to be in the range of $1\,\text{cm}^2/\text{s} \lesssim D_x \lesssim 15\,\text{cm}^2/\text{s}$ for a concentration of $n_{2D} \sim 10^{10}\,\text{cm}^{-2}$ and lattice temperature, $T_b = 5\,\text{K}$.

Recently, measurements of the diffusion of *indirect excitons* in CQW structures were made, by using time-resolved optical imaging [123]. Vörös *et al.* used structures with QWs of various widths, and applied a different voltage across each sample so that the excitons had a similar lifetime in all the samples (up to 30 μs). They plotted the distribution of the excitons at different times after the excitation pulse, and measured the variance of the distribution at each stage. At short time delays, the excitons experienced a strong 'pressure' due to dipole-dipole repulsive interaction, which caused a drift motion. To observe only the diffusive motion (*i.e.* no drift motion), they used the variance at long time delays to measure the diffusion coefficient. For well widths of 8 nm and an applied electric field of $7\,\text{V}/\mu\text{m}$ the diffusion constant was found to be $D_x \sim 0.25\,\text{cm}^2/\text{s}$. A model including drift and diffusion effects has been proposed by Rapaport *et al.* to explain the transport of dipole-oriented QW excitons in CQWs

[124].

Disorder, or 'interface roughness' means variations in the QW and barrier thickness due to imperfections in the sample. These cause an inevitable change in the widths of the wells and consequently the energy levels. Effect of disorder in QWs has been examined experimentally and theoretically in Refs. [112, 113, 122, 126–132]. In Ref. [126], Martelli *et al.* reported on an observation of a PL peak on the low-energy side of the hh free exciton in InGaAs/GaAs QWs at low temperatures, which was attributed to an exciton bound to potential fluctuations due to interface roughness. Similar conclusions were drawn in Ref. [127]. Interface roughness was reported to be the dominant scattering mechanism for *electrons* in thin QWs with well thicknesses $L_z < 6$ nm [112], and was found to have much more of an effect on *exciton* relaxation in thin QWs than in wide QWs [128].

In Ref. [129], Hillmer *et al.* used time-of-flight studies to obtain a diffusion coefficient of $D_x \sim 15$ cm^2/s for direct excitons in an 8 nm-thick QW, with $T = 64$ K and optical lifetime $\tau_{opt} \sim 2.35$ ns. Low-temperature mobilities were found to be mainly determined by interface roughness scattering. This was also confirmed in Ref. [130], where it was shown that in a typical QW sample in which the excitonic diffusion is limited by interface roughness, the diffusivity increases exponentially with increasing QW width.

Recently it was proved that at relatively high concentrations, indirect excitons in CQWs can effectively screen the disorder potential, due to their dipole-dipole repulsive interaction [87]. This is discussed in detail in Section 3.3.

1.14 SUMMARY

In this introduction, a description of the properties of excitons in coupled quantum wells was given: their thermodynamic properties, optical decay, diffusion and possible Bose-Einstein condensation. Many published results on these subjects were discussed and in some cases these were compared with each other.

In the remainder of the thesis, where appropriate, references are made to these and other published results. In the next chapter the temperature dynamics of excitons in CQWs is discussed.

2 RELAXATIONAL THERMODYNAMICS OF QUANTUM WELL EXCITONS

As stated in Section 1.5, relaxational thermodynamics refers to phonon-assisted thermalization kinetics of QW excitons. The thermalization dynamics of quantum well excitons from their initial temperature, $T_i = T(t = 0)$, to the lattice temperature, T_b, is studied in this chapter, where $T_i \gg T_b$. The thermalization of QW excitons occurs through a series of thermodynamic states, characterized by an effective temperature $T = T(t)$ and chemical potential $\mu = \mu(t)$. Relaxational thermodynamics requires that exciton–exciton interaction is much stronger than the exciton–LA-phonon coupling, and is appropriate if the concentration of quantum well excitons is larger than some critical concentration n_{2D}^c, which is $n_{2D}^c \sim 1 - 3 \times 10^9\,\mathrm{cm}^{-2}$ for GaAs QWs [17]. If this is the case, an effective exciton temperature is well-defined.

2.1 THERMODYNAMIC PROPERTIES OF QUANTUM WELL EXCITONS

The concentration of excitons is given by the total number of excitons in the system divided by the area:

$$n_{2D} = \frac{1}{S} \sum_{k_\parallel} N_{k_\parallel} = \frac{gM_x k_B T}{2\pi\hbar^2} \int_0^\infty \frac{dz}{e^{-\mu/k_B T} e^z - 1} \tag{2.1}$$

where $N_{k_{\parallel}}$ is the equilibrium distribution function of QW excitons, and $k_{\parallel}$ is their in-plane momentum. Using Eq.1.2 for the degeneracy temperature, T_0, Eq.2.1 can be written as

$$\frac{T_0}{T} = \int_0^{\infty} \frac{dz}{e^{-\mu/k_{\mathrm{B}}T}e^z - 1}.$$

(2.2)

Integrating this gives

$$\frac{T_0}{T} = -\ln(1 - e^{\mu/k_{\mathrm{B}}T})$$

(2.3)

and therefore

$$\mu = k_{\mathrm{B}}T \ln(1 - e^{-T_0/T}).$$

(2.4)

The equation for equilibrium distribution of N is

$$N_{E_k} = 1/(e^{(E_k - \mu)/k_{\mathrm{B}}T} - 1),$$

(2.5)

where E_k is the energy of an exciton with momentum $k_{\parallel}$. If Eq.2.4 is substituted into Eq.2.5 the result is as follows:

$$N_{E_k} = \frac{1 - e^{-T_0/T}}{e^{E_k/k_{\mathrm{B}}T} + e^{-T_0/T} - 1}.$$

(2.6)

If $E_k = 0$ is substituted into this equation, an equation for the occupation number of the ground state is obtained:

$$N_{E=0} = e^{T_0/T} - 1.$$

(2.7)

In the classical limit, where $T \gg T_0$,

$$N_{E=0} = \frac{T_0}{T} \quad \text{and} \quad \mu = k_{\mathrm{B}}T \ln(T_0/T),$$

(2.8)

and in the quantum limit, where $T < T_0$,

$$N_{E=0} = e^{T_0/T} \quad \text{and} \quad \mu = -k_{\mathrm{B}}T e^{-T_0/T}.$$

(2.9)

These equations summarise the thermodynamic relations for an ideal 2D gas of bosons. Next, the quantum Boltzmann equation (QBE) in momentum space is introduced, and changed to an equation in energy space.

2.2 THE QUANTUM BOLTZMANN EQUATION IN MOMENTUM SPACE

The relaxation kinetics of QW excitons coupled to thermal bulk LA-phonons is given by the quantum Boltzmann equation (QBE). This equation deals with an isotropic in-plane distribution of QW excitons. The QBE in momentum space [92] is given by

$$
\begin{aligned}
\frac{\partial}{\partial t} N_{k_\parallel} = -\frac{2\pi}{\hbar} \sum_q |W(q)|^2 \Bigg\{ & \left[N_{k_\parallel}(1 + n_q^{\mathrm{ph}})(1 + N_{k_\parallel - q_\parallel}) - (1 + N_{k_\parallel})n_q^{\mathrm{ph}} N_{k_\parallel - q_\parallel} \right] \\
& \times \delta(E_{k_\parallel} - E_{k_\parallel - q_\parallel} - \hbar q v_S) + \left[N_{k_\parallel} n_q^{\mathrm{ph}}(1 + N_{k_\parallel + q_\parallel}) \right. \\
& \left. - (1 + N_{k_\parallel})(1 + n_q^{\mathrm{ph}}) N_{k_\parallel + q_\parallel} \right] \delta(E_{k_\parallel} - E_{k_\parallel + q_\parallel} + \hbar q v_S) \Bigg\},
\end{aligned}
\tag{2.10}
$$

where $N_{k_\parallel}$ and n_q^{ph} are the occupation numbers of exciton in-plane mode $k_\parallel$ and phonon bulk mode $q = \{q_\parallel, q_z\}$, respectively, and $q_\parallel$ is the in-plane projection of q. The phonon energy is given by $E = \hbar q v_S$. The terms in the first and second square brackets on the right-hand-side of Eq. 2.10 describe Stokes and anti-Stokes LA-phonon–assisted scattering processes, respectively, from mode $k_\parallel$. The matrix element is given by [90]

$$
W(q) = \sqrt{\frac{\hbar q}{2\rho v_S V}} \, D \, F_z\left(\frac{q_z L_z}{2}\right),
\tag{2.11}
$$

where D is the deformation potential, v_S is the phonon velocity in the crystal, ρ is the crystal density, V is the volume and L_z is the thickness of a quantum well. For an infinitely deep, square quantum well, the form factor is given by [133]

$$
F_z(x) = \frac{\sin x}{x} \frac{e^{ix}}{1 - \frac{x^2}{\pi^2}},
\tag{2.12}
$$

and describes the relaxation of momentum conservation in the z-direction. It is assumed that the quantum well width, L_z, is so small that only the ground state of the well needs to be considered, and therefore F_z is only valid for the ground state.

2.3 THE QUANTUM BOLTZMANN EQUATION IN ENERGY SPACE

If the initial distribution of quantum well excitons is isotropic in momentum space, the QBE in momentum space can be transformed to an equation in terms of energy. In this derivation, it is assumed that excitons interact via phonon emission and absorption only, and in-plane momentum is conserved (in-plane is the $x - y$ plane).

The excitons move in the $x - y$ plane. In this derivation the phonon momentum, q is summed over in spherical coordinates. The discrete summation over momentum states, $\sum_q$, can be replaced by an integral in spherical coordinates:

$$\sum_q \rightarrow \frac{V}{(2\pi)^3(\hbar v_S)^3} \int \int \int E^2 \, \mathrm{d}E \, \mathrm{d}\phi \, \mathrm{d}(\cos\theta), \qquad (2.13)$$

where E is the energy of a phonon with momentum q, and E_k is the energy of an exciton with momentum $k_{\|}$. This is done in the following way: the sum over q is changed to an integral in three dimensions [11], then this is transformed to spherical coordinates [134]. Figure 2.1 shows how spherical coordinates are related to rectangular coordinates, therefore

$$
\begin{aligned}
q_x &= |q| \, \sin\theta \, \cos\phi, \\
q_y &= |q| \, \sin\theta \, \sin\phi, \quad \text{and} \\
q_z &= |q| \, \cos\phi.
\end{aligned}
\qquad (2.14)
$$

Changing the summation to an integral gives

$$
\begin{aligned}
\sum_q \rightarrow \frac{V}{(2\pi)^3} \int \mathrm{d}q &= \frac{V}{(2\pi)^3} \int\int\int \mathrm{d}q_x \, \mathrm{d}q_y \, \mathrm{d}q_z \\
&= \frac{V}{(2\pi)^3} \int\int\int |q|^2 \sin\theta \, \mathrm{d}|q| \, \mathrm{d}\theta \, \mathrm{d}\phi \\
&= \frac{V}{(2\pi)^3(\hbar v_S)^3} \int\int\int E^2 \, \mathrm{d}E \, \mathrm{d}(\cos\theta) \, \mathrm{d}\phi,
\end{aligned}
\qquad (2.15)
$$

and the matrix element also changes to

$$|W(q)|^2 = \frac{D^2 E}{2\rho v_S V} \, F_z^2 \left(\frac{E \cos\theta \, L_z}{2\hbar v_S} \right). \qquad (2.16)$$
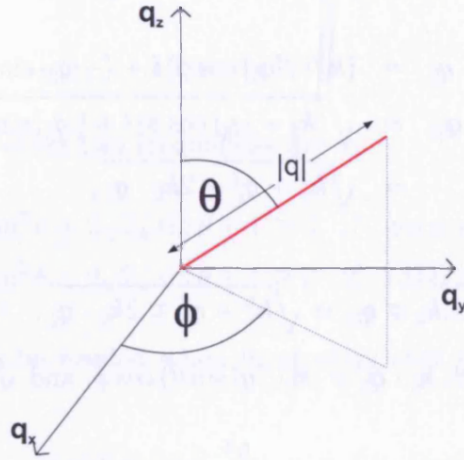
Figure 2.1: Rectangular and spherical coordinates.

To switch Eq. 2.10 to the energy basis, note that $N_{E_k} \equiv N_k$, $n_E \equiv n_q^{\mathrm{ph}}$, $E_k = \frac{\hbar^2 k^2}{2M_x}$ and $E = \hbar v_S q$. Equation 2.10 becomes

$$\frac{\partial}{\partial t} N_{E_k} = -\frac{2\pi}{\hbar} \frac{D^2 \hbar q}{2\rho v_S V} \frac{V}{(2\pi)^3 (\hbar v_S)} \int_{-1}^{1} \int_{0}^{2\pi} \int_{0}^{\infty} \mathrm{d}E \, \mathrm{d}\phi \, \mathrm{d}(\cos\theta) \, E^2 \, F_z\!\left(\frac{E \cos\theta L_z}{2\hbar v_S}\right)$$

$$\times \left\{ \left[N_{E_k}(1 + n_E)(1 + N_{k_\parallel - q_\parallel}) - (1 + N_{E_k}) n_E N_{k_\parallel - q_\parallel} \right] \delta(E_k - E_{k_\parallel - q_\parallel} - E) \right.$$

$$\left. + \left[N_{E_k} n_E (1 + N_{k_\parallel + q_\parallel}) - (1 + N_{E_k})(1 + n_E) N_{k_\parallel + q_\parallel} \right] \delta(E_k - E_{k_\parallel + q_\parallel} + E) \right\}.$$

$$(2.17)$$

As stated at the beginning of this derivation, this transformation can only be done if the initial distribution, $N_k(t = 0)$, is isotropic in momentum space, which is assumed to be the case. Therefore, the change of variables from k to E_k can be done as long as N_k is a constant for all k = constant. So provided $N_k(t = 0)$ is isotropic, and assuming n_q is also isotropic, $N_k(t)$ is isotropic.

Next, to integrate over ϕ, the arguments of the delta functions are changed. The arguments are $(E_{k_\parallel} - E_{k_\parallel \mp q_\parallel} \mp E)$. Taking $k_\parallel$ to be along the x-axis, $|k_\parallel| = k_x$.

$$k_\parallel + q_\parallel = (k_\parallel + |q_\parallel| \cos\phi) i + (|q_\parallel| \sin\phi) j$$

$$|k_\parallel + q_\parallel| = \sqrt{(k_\parallel + |q_\parallel| \cos\phi)^2 + (|q_\parallel| \sin\phi)^2}$$

$$= \sqrt{k_\parallel^2 + q_\parallel^2 + 2 k_\parallel \cdot q_\parallel}. \qquad (2.18)$$

Similarly,

$$\begin{aligned}
\boldsymbol{k}_\| - \boldsymbol{q}_\| &= (k_\| - |q_\||\cos\phi)\boldsymbol{i} + (-|q_\||\sin\phi)\boldsymbol{j} \\
|\boldsymbol{k}_\| - \boldsymbol{q}_\|| &= \sqrt{(k_\| - |q_\||\cos\phi)^2 + (|q_\||\sin\phi)^2} \\
&= \sqrt{k_\|^2 + q_\|^2 - 2\boldsymbol{k}_\| \cdot \boldsymbol{q}_\|}\,,
\end{aligned} \tag{2.19}$$

and therefore

$$|\boldsymbol{k}_\| \mp \boldsymbol{q}_\|| = \sqrt{k_\|^2 + q_\|^2 \mp 2\boldsymbol{k}_\| \cdot \boldsymbol{q}_\|}\,. \tag{2.20}$$

Now, since $|q_\|| = |q|\sin\theta$, $\boldsymbol{k}_\| \cdot \boldsymbol{q}_\| = |\boldsymbol{k}_\||(|q|\sin\theta)\cos\phi$, and $\sqrt{E_k} = \frac{\hbar k}{\sqrt{2M_x}}$,

$$\begin{aligned}
E_{\boldsymbol{k}_\|} - E_{\boldsymbol{k}_\| \mp \boldsymbol{q}_\|} \mp E &= E_k - \frac{\hbar^2}{2M_x}(k_\|^2 + q_\|^2 \mp 2\boldsymbol{k}_\| \cdot \boldsymbol{q}_\|) \mp E \\
&= \frac{-E^2\sin^2\theta}{2M_x v_S^2} \pm \frac{2\sqrt{E_k}E}{\sqrt{2M_x}v_S}\sin\theta \, \cos\phi \mp E\,. \tag{2.21}
\end{aligned}$$

Integration over a delta-function will select the values for which the argument of the delta-function is zero. So now the argument is set to be equal to zero:

$$\frac{-E^2\sin^2\theta}{2M_x v_S^2} \pm \frac{2\sqrt{E_k}E}{\sqrt{2M_x}v_S}\sin\theta \, \cos\phi \mp E = 0\,. \tag{2.22}$$

Now, $2M_x v_S^2 = E_0$, and let $\frac{E}{E_0} = \varepsilon$, $\frac{E_k}{E_0} = \varepsilon_k$. Equation 2.22 can be simplified to

$$-\varepsilon\sin^2\theta \pm 2\sqrt{\varepsilon_k}\sin\theta \, \cos\phi \mp 1 = 0\,. \tag{2.23}$$

Note from Fig. 2.1 that

$$\begin{aligned}
\phi \in [0, 2\pi] &\rightarrow \cos\phi \in [-1, 1] \\
\theta \in [0, \pi] &\rightarrow \sin\theta \in [0, 1]\,. \tag{2.24}
\end{aligned}$$

First, Stokes scattering is dealt with. The inequality

$$\varepsilon_k - \varepsilon \geq 0 \tag{2.25}$$

must be true, and Eq. 2.23 can be rearranged to give another two:

$$\varepsilon\sin^2\theta + 2\sqrt{\varepsilon_k}\sin\theta + 1 \geq 0 \quad \text{if} \quad \cos\phi < 0, \text{ and} \tag{2.26}$$

$$-\varepsilon\sin^2\theta + 2\sqrt{\varepsilon_k}\sin\theta - 1 \geq 0 \quad \text{if} \quad \cos\phi > 0. \tag{2.27}$$

Secondly, anti-Stokes scattering is dealt with, so the inequality

$$\varepsilon - \varepsilon_k \geq 0 \qquad (2.28)$$

must be true, and the other two inequalities are

$$-\varepsilon \sin^2 \theta + 2\sqrt{\varepsilon_k} \sin \theta + 1 \geq 0 \quad \text{if} \quad \cos \phi < 0, \text{ and} \qquad (2.29)$$

$$\varepsilon \sin^2 \theta + 2\sqrt{\varepsilon_k} \sin \theta - 1 \geq 0 \quad \text{if} \quad \cos \phi > 0. \qquad (2.30)$$

These inequalities will be needed when integrating over the delta-functions. Note that

$$\cos \phi' = \frac{\varepsilon \sin^2 \theta + 1}{2\sqrt{\varepsilon_k} \sin \theta} \quad \text{and} \quad \cos \phi'' = \frac{-\varepsilon \sin^2 \theta + 1}{2\sqrt{\varepsilon_k} \sin \theta} \qquad (2.31)$$

where ϕ' corresponds to Stokes scattering, and ϕ'' corresponds to anti-Stokes scattering. This gives

$$|\sin \phi'^{/''}| = \sqrt{1 - \cos^2 \phi'^{/''}} = \frac{\sqrt{4\varepsilon_k \sin^2 \theta - (\varepsilon \sin^2 \pm 1)^2}}{2\sqrt{\varepsilon_k} \sin \theta}. \qquad (2.32)$$

Equations 2.31 and 2.32 are derived from Eq. 2.23, and Eq. 2.32 will be needed in the final part of the derivation. To carry out integration over a delta-function the following rule is used:

$$\delta\left(f(x)\right) = \sum_i \frac{\delta(x - x_i)}{|f'(x_i)|} \qquad (2.33)$$

where $f(x_i) = 0$. The integral over ϕ is

$$\int_0^{2\pi} d\phi \; \delta\left(\frac{-E^2}{E_0} \sin^2\theta \pm \frac{2\sqrt{E_k}E \sin\theta \, \cos\phi}{\sqrt{E_0}} \mp E\right) = \int_0^{2\pi} d\phi \; \frac{1}{2\sqrt{\frac{E_k}{E_0}}E \sin\theta} \sum_i \frac{\delta(\phi - \phi_i)}{|\sin\phi_i|}$$

$$= \frac{1}{\sqrt{\varepsilon_k}E \sin\theta} \int_0^{2\pi} d\phi \; \frac{\delta(\phi - \phi'^{/''})}{|\sin\phi'^{/''}|}$$

$$= \frac{1}{\sqrt{\varepsilon_k}E \sin\theta} \left[\frac{\Theta(2\pi - \phi'^{/''})\Theta(\phi'^{/''})}{|\sin\phi'^{/''}|}\right].$$

$$(2.34)$$

The factor 2 disappears from the bottom of the equation because there are two values at which the argument of the delta-function is zero (see Eq. 2.33). The two Heaviside functions in Eq. 2.34 are equivalent to $0 \leq \phi'^{/''} \leq 2\pi$, therefore the inequalities found previously can be used, written as Heaviside step functions. Therefore Eq. 2.34 for

Stokes scattering becomes

$$\frac{1}{\sqrt{\varepsilon_k}E\sin\theta}\left[\frac{\Theta(2\pi-\phi')\Theta(\phi')}{|\sin\phi'|}\right] = \frac{2}{E}\frac{1}{\sqrt{4\varepsilon_k\sin^2\theta-(\varepsilon\sin^2\theta-1)^2}}$$
$$\times\Theta(2\sqrt{\varepsilon_k}\sin\theta-\varepsilon\sin^2\theta+1)\Theta(\varepsilon_k-\varepsilon),$$

$$(2.35)$$

and for anti-Stokes scattering it becomes

$$\frac{1}{\sqrt{\varepsilon_k}E\sin\theta}\left[\frac{\Theta(2\pi-\phi'')\Theta(\phi'')}{|\sin\phi''|}\right] = \frac{2}{E}\frac{1}{\sqrt{4\varepsilon_k\sin^2\theta-(\varepsilon\sin^2\theta-1)^2}}$$
$$\times\Theta(2\sqrt{\varepsilon_k}\sin\theta-\varepsilon\sin^2\theta+1)$$
$$\times\Theta(\varepsilon\sin^2\theta+2\sqrt{\varepsilon_k}\sin\theta-1)\Theta(\varepsilon-\varepsilon_k).$$

$$(2.36)$$

For Stokes scattering, there are only two Heaviside step functions instead of the three found previously; the inequality in Eq. 2.26 can be omitted because its argument is always positive.

Equations 2.35 and 2.36 can be substituted into the QBE (Eq. 2.17), and if Eq. 2.32 is also used, the final form of the QBE in energy space is

$$\frac{\partial}{\partial t}N_{\varepsilon_k} = -\frac{2}{\tau_{\rm sc}}\int_{-1}^{1}\int_0^\infty d\varepsilon\,\varepsilon^2\,d(\cos\theta)\,|F_z(\varepsilon a\cos\theta)|^2$$

$$\times\left\{\frac{1}{\sqrt{4\varepsilon_k\sin^2\theta-(\varepsilon\sin^2\theta+1)^2}}[N_{\varepsilon_k}(1+n_\varepsilon)(1+N_{\varepsilon_k-\varepsilon})-(1+N_{\varepsilon_k})n_\varepsilon N_{\varepsilon_k-\varepsilon}]\right.$$
$$\times\Theta(2\sqrt{\varepsilon_k}\sin\theta-\varepsilon\sin^2\theta-1)\Theta(\varepsilon_k-\varepsilon)$$
$$+\frac{1}{\sqrt{4\varepsilon_k\sin^2\theta-(\varepsilon\sin^2\theta-1)^2}}[N_{\varepsilon_k}n_\varepsilon(1+N_{\varepsilon_k+\varepsilon})-(1+N_{\varepsilon_k})(1+n_\varepsilon)N_{\varepsilon_k+\varepsilon}]$$
$$\left.\times\Theta(2\sqrt{\varepsilon_k}\sin\theta-\varepsilon\sin^2\theta+1)\Theta(\varepsilon\sin^2\theta+2\sqrt{\varepsilon_k}\sin\theta-1)\Theta(\varepsilon-\varepsilon_k)\right\}.$$

$$(2.37)$$

The characteristic scattering time is defined as

$$\tau_{\rm sc} = \frac{\pi^2\hbar^4\rho}{D^2 M_x^3 v_{\rm S}},$$

$$(2.38)$$

and typical values for GaAs QWs as described in Section 1.10 are: $\tau_{\rm sc} = 215\,\mathrm{ns}$ (for $D = 6.5\,\mathrm{eV}$), $\tau_{\rm sc} = 98\,\mathrm{ns}$ (for $D = 9.6\,\mathrm{eV}$) and $\tau_{\rm sc} = 38\,\mathrm{ns}$ (for $D = 15.5\,\mathrm{eV}$). The

dimensionless constant a is given by

$$a = \frac{L_z M_x v_S}{\hbar} . \tag{2.39}$$

and $a = 0.055$ if $M_x = 0.215 m_0$ and $L_z = 8\,\text{nm}$. Once again, ε is the (dimensionless) energy of a phonon and ε_k is the (dimensionless) energy of an exciton. N_{ε_k}, n_ε and $N_{\varepsilon_k \pm \varepsilon}$ are the occupation numbers of the energy levels ε_k, ε and $\varepsilon_k \pm \varepsilon$ respectively, and θ is the angle between the direction of the phonon and the z-axis.

Next, the basic equation of relaxational thermodynamics of QW excitons is derived. This equation provides a unified description of the thermalization process, and can be used to study how Bose-Einstein statistics influence the thermalization of quantum well excitons.

2.4 THE BASIC EQUATION OF RELAXATIONAL THERMODYNAMICS

The basic equation of relaxational thermodynamics of quantum well excitons is derived from the QBE.

As in the previous derivation, the starting point is the QBE in momentum space (Eq. 2.10). This time, only excitons already in the ground state are dealt with, therefore Stokes scattering is not allowed. The exciton momentum is set to be equal to zero, $k_\parallel = 0$, and the first term in the large brackets in Eq. 2.10 disappears, so:

$$
\begin{aligned}
\frac{\partial}{\partial t} N_{k_\parallel = 0} &= \frac{2\pi}{\hbar} \sum_q |W(q)|^2 \left[N_{k_\parallel = 0} n_q^{\text{ph}} (1 + N_{q_\parallel}) - (1 + N_{k_\parallel = 0})(1 + n_q^{\text{ph}}) N_{q_\parallel} \right] \\
&\quad \times \delta(\hbar q v_S - E_{k_\parallel + q_\parallel}) \\
&= -\frac{2\pi}{\hbar} \frac{\hbar q}{2\rho v_S V} D^2 \sum_q \left| F_z \left(\frac{q_z L_z}{2} \right) \right|^2 \\
&\quad \times \left[N_{k_\parallel = 0} n_q^{\text{ph}} (1 + N_{q_\parallel}) - (1 + N_{k_\parallel = 0})(1 + n_q^{\text{ph}}) N_{q_\parallel} \right] \delta(\hbar q v_S - E_{k_\parallel + q_\parallel}) .
\end{aligned}
\tag{2.40}
$$

By using Eq. 2.15 to switch to the energy basis and noting that integrating over ϕ is

simply equal to 2π, the equation becomes

$$\frac{\partial}{\partial t} N_{E_k=0} = -\frac{D^2}{4\pi\hbar^4\rho v_{\rm S}^5} \int_{-1}^{1} \int_{0}^{\infty} dE\, E^3 d(\cos\theta) \left| F_z \left(\frac{E\cos\theta L_z}{2\hbar v_{\rm S}} \right) \right|^2$$
$$\times \left[N_{E_k=0} n_E (1 + N_{q_\parallel}) - (1 + N_{E_k=0})(1 + n_E) N_{q_\parallel} \right] \delta(E - E_{q_\parallel}).$$
(2.41)

The delta-function argument can be written as

$$E - E_{q_\parallel} = E - \frac{\hbar^2 \boldsymbol{q}_\parallel{}^2}{2M_{\rm x}} = E - \frac{E^2 \sin^2\theta}{2M_{\rm x} v_{\rm S}^2}.$$
(2.42)

Now, using Eq. 2.33, the integration with respect to $\cos\theta$ is dealt with:

$$\int_{-1}^{1} d(\cos\theta)\; \delta\left(E - \frac{E^2 \sin^2\theta}{E_0}\right) F_z^2\left(E \frac{\cos\theta L_z}{2\hbar v_{\rm S}}\right)$$
$$= \int_{-1}^{1} d(\cos\theta) F_z^2\left(E\frac{\cos\theta L_z}{2\hbar v_{\rm S}}\right) \sum_i \frac{\delta(\cos\theta - \cos\theta_i)}{\left|\frac{-2E}{E_0}\cos\theta_i\right|}.$$
(2.43)

The delta-function is equal to zero when

$$\cos\theta_i = \pm\sqrt{\frac{E - E_0}{E}},$$
(2.44)

so the RHS of Eq. 2.43 is

$$= \frac{E_0}{2E}\sqrt{\frac{E}{E - E_0}} \int_{-1}^{1} d(\cos\theta) F_z^2 \left(\frac{E\cos\theta L_z}{2\hbar v_{\rm S}}\right)$$
$$\times \left[\delta\left(\cos\theta - \sqrt{\frac{E - E_0}{E}}\right) + \delta\left(\cos\theta + \sqrt{\frac{E - E_0}{E}}\right)\right].$$
(2.45)

Substituting $\frac{E}{E_0} = \varepsilon$ and $\frac{E_k}{E_0} = \varepsilon_k$ as before, and integrating over $\cos\theta$ gives

$$= \frac{1}{2E\sqrt{\varepsilon(\varepsilon - 1)}} \left[F_z^2\left(\frac{EL_z}{2\hbar v_{\rm S}}\sqrt{\frac{\varepsilon - 1}{\varepsilon}}\right) + F_z^2\left(\frac{-EL_z}{2\hbar v_{\rm S}}\sqrt{\frac{\varepsilon - 1}{\varepsilon}}\right) \right]$$
(2.46)

and since $F_z^2(x) = F_z^2(-x)$,

$$= \frac{1}{E_{\rm q}\sqrt{\varepsilon(\varepsilon - 1)}} F_z^2(a\sqrt{\varepsilon(\varepsilon - 1)})$$
(2.47)

where a is given by Eq. 2.39. Going back to the original equation, Eq. 2.41, and

substituting all the above gives

$$\frac{\partial}{\partial t}N_{\varepsilon_k=0} = \frac{-D^2\pi}{4\rho v_S^5 \hbar^4} \int_0^\infty dE \, E^2 \frac{1}{\sqrt{\varepsilon(\varepsilon-1)}} \, F_z^2\left(a\sqrt{\varepsilon(\varepsilon-1)}\right)$$
$$\times \left[N_{\varepsilon_k=0}\, n_\varepsilon(1+N_\varepsilon) - (1+N_{\varepsilon_k=0})(1+n_\varepsilon)N_\varepsilon\right] \qquad (2.48)$$

where $n_\varepsilon \equiv n_E = n_q^{ph}$, $N_\varepsilon \equiv N_E = N_{q_\parallel}$ and $N_{\varepsilon_k=0} \equiv N_{E_k=0} = N_{k_\parallel=0}$. Dividing the integrand by $E_0^3 = (2M_x v_S^2)^3$ gives

$$\frac{\partial}{\partial t}N_{\varepsilon_k=0} = \frac{2\pi}{\tau_{sc}} \int_1^\infty d\varepsilon \, \varepsilon \sqrt{\frac{\varepsilon}{\varepsilon-1}} \, F_z^2\left(a\sqrt{\varepsilon(\varepsilon-1)}\right) \left[N_\varepsilon(1+n_\varepsilon) - N_{\varepsilon_k=0}(n_\varepsilon-N_\varepsilon)\right]$$
$$(2.49)$$

where the characteristic scattering time, τ_{sc} is defined in Eq. 2.38.

Now, when $\varepsilon_k = 0$, the occupation number is given by $N_{E=0} = e^{T_0/T} - 1$ (Eq. 2.7) and differentiating this with respect to time gives

$$\frac{\partial}{\partial t}T = -\frac{T^2}{T_0}\, e^{-T_0/T}\frac{\partial}{\partial t}N_k \, . \qquad (2.50)$$

Substituting Eq. 2.49 into this equation gives the final equation, the basic equation of relaxational thermodynamics:

$$\frac{\partial}{\partial t}T = -\frac{2\pi}{\tau_{sc}}\left(\frac{T^2}{T_0}\right)(1-e^{-T_0/T})\int_1^\infty d\varepsilon \, \varepsilon \sqrt{\frac{\varepsilon}{\varepsilon-1}} \left|F_z\left(a\sqrt{\varepsilon(\varepsilon-1)}\right)\right|^2$$
$$\times \left(\frac{e^{\varepsilon E_0/k_B T_b} - e^{\varepsilon E_0/k_B T}}{e^{\varepsilon E_0/k_B T} + e^{-T_0/T} - 1}\right)\left(\frac{1}{e^{\varepsilon E_0/k_B T_b} - 1}\right). \qquad (2.51)$$

This equation describes how the initially hot photoexcited excitons thermalize from their initial temperature $T_i = T(t = 0)$ to the temperature of the lattice, T_b, with respect to time.

RESULTS

Results obtained by using Eq. 2.51 are shown in Fig. 2.2. Details of the parameters used are given in Section 1.10, and here the deformation potential, $D = 6.5\,eV$ and the initial energy, $E_i/k_B = 200\,K$.

From Fig. 2.2 it is clear that the excitons take a much longer time to thermalize when T_b is lower and/or n_{2D} is larger. This thermalization time, τ_{th} is discussed in the next

section.

Figure 2.3 shows how the occupation number of the ground state increases with time. This is calculated by using Eq. 2.7. So if the concentration of excitons, $n_{2D} > 10^{10}\,\mathrm{cm}^{-2}$ then the occupation number of the ground state is > 1 after 10 ns. The lifetime of an exciton $\sim 10\,\mathrm{ns}$ so this graph shows that it could be possible for excitons to accumulate in the lowest energy states if there are no other processes to oppose this accumulation. In Fig. 2.4, $\ln\{(T - T_b)/1\,\mathrm{K}\}$ is plotted against t for various T_b. This shows that the relaxation of excitons follows exponential decay at high T_b.

2.5   THE CHARACTERISTIC THERMALIZATION TIME OF EXCITONS

Starting with the basic equation of relaxational thermodynamics (Eq. 2.51), it is possible to derive an equation for the characteristic thermalization time of excitons, τ_{th}, when their temperature is close to the lattice temperature. The thermalization time is defined as the time taken for the excitons to cool to the lattice temperature.

The integrand in Eq. 2.51 is equal to zero when $T = T_b$. This means that when linearizing, the prefactor can be treated simply by putting $T = T_b$. The T-dependent integrand in Eq. 2.51,

$$\left(\frac{e^{\varepsilon E_0/k_B T_b} - e^{\varepsilon E_0/k_B T}}{e^{\varepsilon E_0/k_B T} + e^{-T_0/T} - 1} \right) \left(\frac{1}{e^{\varepsilon E_0/k_B T_b} - 1} \right),$$

can be represented in the form $f(T) = v/w$, where v and w are the numerator and denominator respectively. Again, because the linearization is at $T = T_b$, note that $v(T = T_b) = 0$. Thus the expansion of $f(T)$ at $T = T_b$ is given by $f(T) = (v'/w)dT$. This gives

$$\frac{\partial}{\partial t} T = -\frac{2\pi}{\tau_{sc}}(T - T_b)\left(\frac{T_b^2}{T_0}\right)\frac{E_0}{k_B T_b^2}(1 - e^{-T_0/T_b})\int_1^\infty d\varepsilon\ \varepsilon^2 \sqrt{\frac{\varepsilon}{\varepsilon - 1}}\ \left| F_z\left(a\sqrt{\varepsilon(\varepsilon - 1)}\right)\right|^2$$

$$\times \left(\frac{e^{\varepsilon E_0/k_B T_b}}{e^{\varepsilon E_0/k_B T_b} + e^{-T_0/T_b} - 1} \right) \left(\frac{1}{e^{\varepsilon E_0/k_B T_b} - 1} \right). \tag{2.52}$$

The basic thermodynamic equation (Eq. 2.51) reduces to the following equation if T

(a) $T_\mathrm{b} = 1\,\mathrm{K}$
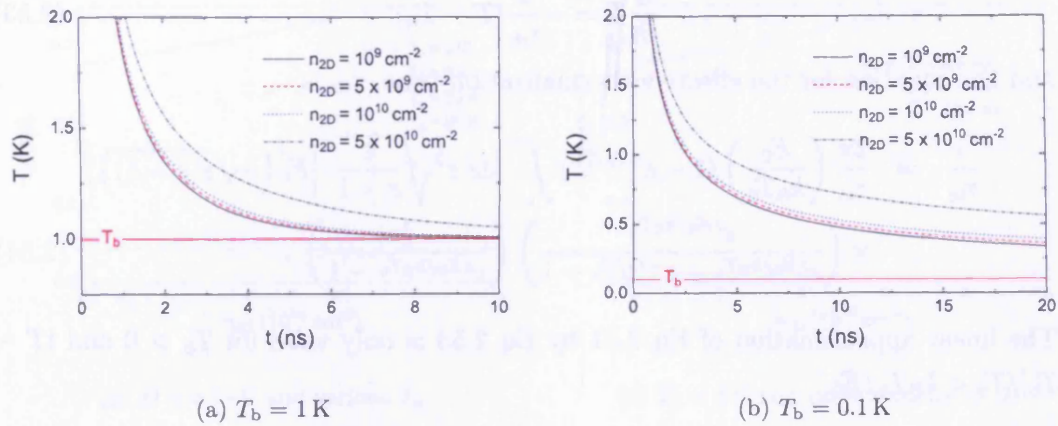
(b) $T_\mathrm{b} = 0.1\,\mathrm{K}$

Figure 2.2: Thermalization dynamics $T = T(t)$ of excitons for $T_\mathrm{i} = 200\,\mathrm{K}$ and various concentrations as shown.
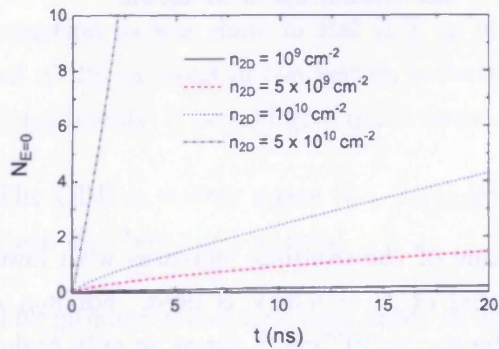
Figure 2.3: A plot of $N_{E=0}$ against time for $T_\mathrm{b} = 0.1\,\mathrm{K}$ and various concentrations as shown.
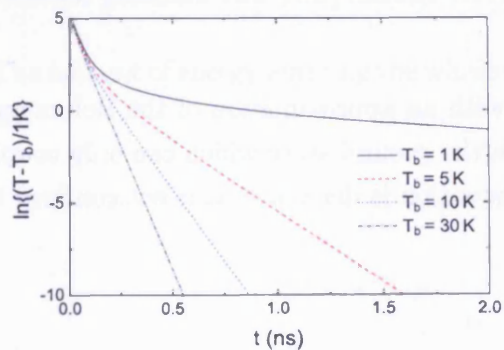
Figure 2.4: A plot of $\ln\{(T - T_\mathrm{b})/1\,\mathrm{K}\}$ against time for $n_\mathrm{2D} = 10^9\,\mathrm{cm}^{-2}$, $T_\mathrm{i} = 200\,\mathrm{K}$ and various lattice temperatures as shown.

is close to T_b:

$$\frac{\partial}{\partial t}T = -\frac{1}{\tau_{th}}(T - T_b) \tag{2.53}$$

and the equation for the effective thermalization time, τ_{th} is

$$\frac{1}{\tau_{th}} = \frac{2\pi}{\tau_{sc}}\left(\frac{E_0}{k_B T_0}\right)(1 - e^{-T_0/T_b})\int_1^\infty d\varepsilon\, \varepsilon^2 \sqrt{\frac{\varepsilon}{\varepsilon - 1}}\left|F_z\left(a\sqrt{\varepsilon(\varepsilon - 1)}\right)\right|^2$$

$$\times \left(\frac{e^{\varepsilon E_0/k_B T_b}}{e^{\varepsilon E_0/k_B T_b} + e^{-T_0/T_b} - 1}\right)\left(\frac{1}{e^{\varepsilon E_0/k_B T_b} - 1}\right). \tag{2.54}$$

The linear approximation of Eq. 2.51 by Eq. 2.53 is only valid for $T_b > 0$ and $|T - T_b|/T_b < k_B T_b/E_0$.
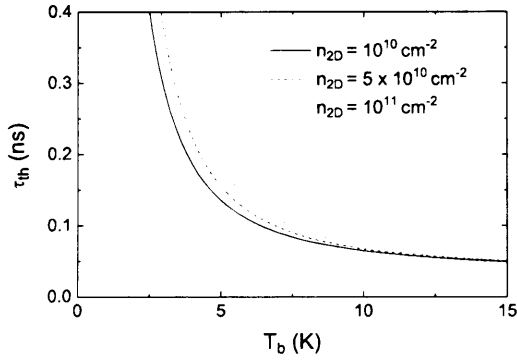
Figure 2.5: The thermalization time plotted against lattice temperature for various concentrations as shown.

Figure 2.5 shows how the thermalization time of the excitons increases with lower lattice temperatures. A deformation potential of $D = 6.5\,\text{eV}$ is used. For $n_{2D} < 10^{10}\,\text{cm}^{-2}$ the curves nearly coincide with the $n_{2D} = 10^{10}\,\text{cm}^{-2}$ curve, so only higher concentrations are shown. Figure 2.6 shows the exciton thermalization time against concentration. The thermalization time increases substantially as the lattice temperature is reduced or the concentration of excitons is increased, and is higher for lower values of D.

The equations in Section 2.4 and 2.5 deal with an approximation of the Boltzmann equation, and only treat excitons already in the ground state which can only couple in anti-Stokes with LA phonons. Next, an equation is derived that is not confined to excitons already in the ground state.

(a) $D = 6.5\,\text{eV}$ and various T_b.

(b) $T_b = 3\,\text{K}$ and various values of D.
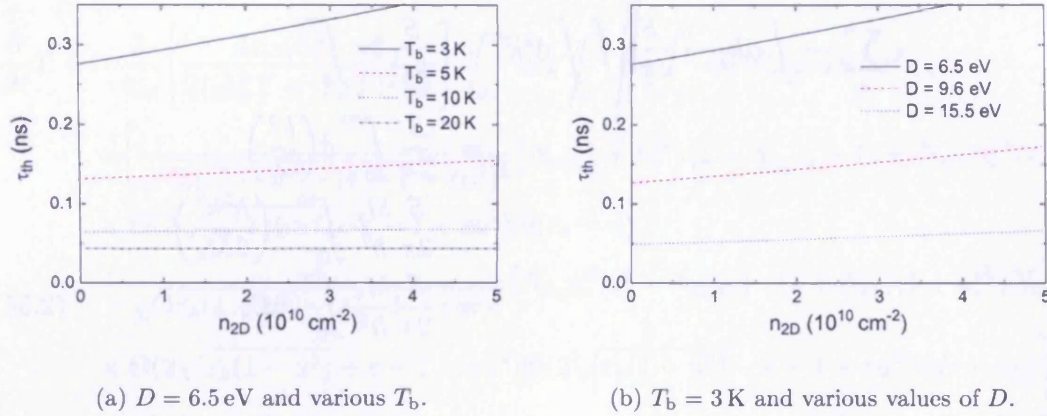
Figure 2.6: The thermalization time of excitons plotted against concentration.

2.6 THE COMPLETE MICROSCOPIC EQUATION

As mentioned in Section 1.5, instead of treating an approximation of the Boltzmann equation as was done in Ref. [17], a 'microscopic' equation that takes into account all of the excitons in the system is derived. Although this complicates the equations considerably, it should give much more accurate results.

The QBE in energy space (Eq. 2.37) gives the number of excitons that enter energy state E_k every time interval.

The number of excitons that enter energy level ε_k every time unit $= \frac{\partial}{\partial t} N_{\varepsilon_k}$.

The amount of energy that enter energy level ε_k every time unit $= \frac{\partial N_{\varepsilon_k}}{\partial t} \times E_k$.
This is just one energy state. For the amount of energy entering the whole system of excitons per time unit every energy level, ε_k, has to be taken into account.

The amount of energy entering the whole system of excitons per time unit $= \sum_{\varepsilon_k} \frac{\partial N_{\varepsilon_k}}{\partial t} \times E_k$.

Now change to an integral:

$$
\begin{aligned}
\sum_{k_\parallel} \to \int \mathrm{d}\boldsymbol{k}_\parallel \to \frac{S}{4\pi^2} \int\!\!\int \mathrm{d}^2 k &= \frac{S}{4\pi^2} 2\pi \int_0^\infty k \, \mathrm{d}k \\
&= \frac{S}{2\pi} \int_0^\infty \mathrm{d}\!\left(\frac{k^2}{2}\right) \\
&= \frac{S}{2\pi} \frac{M_\mathrm{x}}{\hbar^2} \int_0^\infty \mathrm{d}\!\left(\frac{\hbar^2 k^2}{2M_\mathrm{x}}\right) \\
&= \frac{S}{2\pi} \frac{M_\mathrm{x}}{\hbar^2} \int_0^\infty \mathrm{d}E_k.
\end{aligned}
\tag{2.55}
$$

So the amount of energy entering the system of excitons per time unit is

$$
\begin{aligned}
&= \frac{\partial}{\partial t} E_\mathrm{total} \\
&= \frac{S}{2\pi} \frac{M_\mathrm{x}}{\hbar^2} \int_0^\infty \frac{\partial N_{\varepsilon_k}}{\partial t} E_k \, \mathrm{d}E_k.
\end{aligned}
\tag{2.56}
$$

Equation 2.56 will be substituted into Eq. 2.60. Now, note that the total energy $E_\mathrm{total} = \sum_E E N_E$, which gives

$$
E_\mathrm{total} = \sum_{k_\parallel} \frac{\hbar^2 k_\parallel^2}{2M_\mathrm{x}} \frac{1}{e^{-\mu/k_\mathrm{B}T} e^{\hbar^2 k_\parallel^2/2M_\mathrm{x} k_\mathrm{B}T} - 1} = \frac{M_\mathrm{x}}{\hbar^2} \frac{S}{2\pi} \int_0^\infty \mathrm{d}E_k \frac{E_k}{e^{-\mu/k_\mathrm{B}T} e^{E_k/k_\mathrm{B}T} - 1}
\tag{2.57}
$$

Letting $A = e^{-\mu/k_\mathrm{B}T}$ and $z = E_k/k_\mathrm{B}T$,

$$
E_\mathrm{total} = \frac{M_\mathrm{x}}{\hbar^2} \frac{S}{2\pi} (k_\mathrm{B}T)^2 \int_0^\infty \mathrm{d}z \frac{z}{A e^z - 1}.
\tag{2.58}
$$

If $I_0 = \int_0^\infty \mathrm{d}z \frac{z}{A e^z - 1}$ then

$$
\frac{\partial}{\partial t} E_\mathrm{total} = \frac{M_\mathrm{x}}{\hbar^2} \frac{S}{2\pi} \left[2 I_0 k_\mathrm{B}^2 T \frac{\partial T}{\partial t} + (k_\mathrm{B}T)^2 \frac{\partial I_0}{\partial T} \frac{\partial T}{\partial t} \right],
\tag{2.59}
$$

so

$$
\frac{\partial}{\partial t} T = \frac{\hbar^2}{M_\mathrm{x}} \frac{2\pi}{S} \left[\frac{1}{2 I_0 k_\mathrm{B}^2 T + (k_\mathrm{B}T)^2 \frac{\partial I_0}{\partial T}} \right] \frac{\partial}{\partial t} E_\mathrm{total}.
\tag{2.60}
$$

Substituting $\frac{\mathrm{d}E_\mathrm{total}}{\mathrm{d}t}$ from Eq. 2.56 gives

$$
\frac{\partial}{\partial t} T = \left[\frac{1}{2 I_0 k_\mathrm{B}^2 T + (k_\mathrm{B}T)^2 \frac{\partial I_0}{\partial T}} \right] \int_0^\infty \frac{\partial N_{\varepsilon_k}}{\partial t} E_k \, \mathrm{d}E_k.
\tag{2.61}
$$

Note that $\frac{\partial N_{\varepsilon_k}}{\partial t}$ is given by the QBE (Eq. 2.37), so this is substituted in, giving

$$
\frac{\partial}{\partial t} T = -\frac{2}{\tau_{\rm sc}} \left[\frac{E_0^2}{2 I_0 k_{\rm B}^2 T + (k_{\rm B}T)^2 \frac{\partial I_0}{\partial T}} \right] \int_0^\infty {\rm d}\varepsilon_k \int_0^\infty {\rm d}\varepsilon \int_{-1}^1 {\rm d}u \, |F_z(a\varepsilon u)|^2 \, \varepsilon^2 \, \varepsilon_k
$$

$$
\times \Bigg\{ \frac{1}{\sqrt{4\varepsilon_k(1-u^2)-(\varepsilon+1-\varepsilon u^2)^2}} \left[N_{\varepsilon_k}(1+n_\varepsilon^{\rm ph})(1+N_{\varepsilon_k-\varepsilon}) - (1+N_{\varepsilon_k})n_\varepsilon^{\rm ph}N_{\varepsilon_k-\varepsilon} \right]
$$

$$
\times \Theta(2\sqrt{\varepsilon_k(1-u^2)}-\varepsilon-1+\varepsilon u^2)\Theta(\varepsilon_k - \varepsilon)
$$

$$
+ \frac{1}{\sqrt{4\varepsilon_k(1-u^2)-(\varepsilon-1-\varepsilon u^2)^2}} \left[N_{\varepsilon_k}n_\varepsilon^{\rm ph}(1+N_{\varepsilon_k+\varepsilon}) - (1+N_{\varepsilon_k})(1+n_\varepsilon^{\rm ph})N_{\varepsilon_k+\varepsilon} \right]
$$

$$
\times \Theta(2\sqrt{\varepsilon_k(1-u^2)}+\varepsilon-1-\varepsilon u^2)\Theta(2\sqrt{\varepsilon_k(1-u^2)}-\varepsilon+1+\varepsilon u^2)\Theta(\varepsilon - \varepsilon_k) \Bigg\} .
$$

$$(2.62)$$

The following substitutions for the distribution functions are now made: $n_\varepsilon^{\rm ph} = 1/(e^{\varepsilon E_0/k_{\rm B}T_{\rm b}} - 1)$ (Eq. 1.3), $N_{\varepsilon_k} = (1 - e^{-T_0/T})/(e^{E_k/k_{\rm B}T} + e^{-T_0/T} - 1)$ (Eq. 2.6) and

$$
N_{\varepsilon_k \pm \varepsilon} = \frac{1 - e^{-T_0/T}}{e^{(E_k \pm E)/k_{\rm B}T} + e^{-T_0/T} - 1} , \qquad (2.63)
$$

so finally, the full microscopic equation is

$$
\frac{\partial}{\partial t} T = -\frac{2}{\tau_{\rm sc}} \left[\frac{E_0^2}{2 I_0 k_{\rm B}^2 T + (k_{\rm B}T)^2 \frac{\partial I_0}{\partial T}} \right] \int_0^\infty {\rm d}\varepsilon_k \int_0^\infty {\rm d}\varepsilon \int_{-1}^1 {\rm d}u \, |F_z(a\varepsilon u)|^2 \, \varepsilon^2 \varepsilon_k
$$

$$
\times \frac{e^{\varepsilon_k E_0/k_{\rm B}T}(1 - e^{-T_0/T})}{(e^{\varepsilon_k E_0/k_{\rm B}T} + e^{-T_0/T} - 1)(e^{\varepsilon E_0/k_{\rm B}T_{\rm b}} - 1)}
$$

$$
\times \Bigg\{ \frac{1}{\sqrt{4\varepsilon_k(1-u^2)-(\varepsilon+1-\varepsilon u^2)^2}} \frac{e^{\varepsilon E_0/k_{\rm B}T_{\rm b}}e^{-\varepsilon E_0/k_{\rm B}T} - 1}{(e^{\varepsilon_k E_0/k_{\rm B}T}e^{-\varepsilon E_0/k_{\rm B}T} + e^{-T_0/T} - 1)}
$$

$$
\times \Theta(2\sqrt{\varepsilon_k(1-u^2)}-\varepsilon-1+\varepsilon u^2)\Theta(\varepsilon_k - \varepsilon)
$$

$$
+ \frac{1}{\sqrt{4\varepsilon_k(1-u^2)-(\varepsilon-1-\varepsilon u^2)^2}} \frac{e^{\varepsilon E_0/k_{\rm B}T} - e^{\varepsilon E_0/k_{\rm B}T_{\rm b}}}{e^{\varepsilon_k E_0/k_{\rm B}T}e^{\varepsilon E_0/k_{\rm B}T} + e^{-T_0/T} - 1}
$$

$$
\times \Theta(2\sqrt{\varepsilon_k(1-u^2)}+\varepsilon-1-\varepsilon u^2)\Theta(2\sqrt{\varepsilon_k(1-u^2)}-\varepsilon+1+\varepsilon u^2)\Theta(\varepsilon - \varepsilon_k) \Bigg\}.
$$

$$(2.64)$$

This 'microscopic' equation proved to be very complicated to work with. When this equation is numerically modelled with a computational code, it takes an extensive amount of time to obtain accurate results. The 3-fold integration is over irregular and spiky functions, which are even more irregular at lower temperatures. Therefore,

it is not practical to include any additional effect to this equation because the time-scale needed to obtain the results would be very long. In the next section, the results obtained with this equation are compared with the results obtained with the basic equation (Eq. 2.51). In further work throughout this thesis, a modified version of the basic equation of relaxational thermodynamics (Eq. 2.51) is used instead, detailed in the next section.

2.7 COMPARISON OF SIMPLE AND MICROSCOPIC RESULTS

Since Eq. 2.64 is too complicated to be combined with other equations (which is done in further sections), the results are compared with the results of Eq. 2.51. The results of Eqs. 2.51 and 2.64 only differ significantly at low lattice temperatures, $T_b < 1\,\mathrm{K}$. As shown in Fig. 1.6, E_0 is the crossover between the exciton and phonon dispersion, and therefore the value of E_0 controls the kinetics of excitons at low temperatures. It is for this reason that E_0 was chosen as a fit parameter: its value was changed in Eq. 2.51 and the results are plotted to compare with the results of Eq. 2.64. For results at $T_b = 1.8$ and $0.35\,\mathrm{K}$ see Figs. 2.7 and 2.8. Here, $D = 6.5\,\mathrm{eV}$ and $T_i = 200\,\mathrm{K}$.

(a) $n_{2D} = 10^9\mathrm{cm}^{-2}$

(b) $n_{2D} = 3 \times 10^{10}\mathrm{cm}^{-2}$
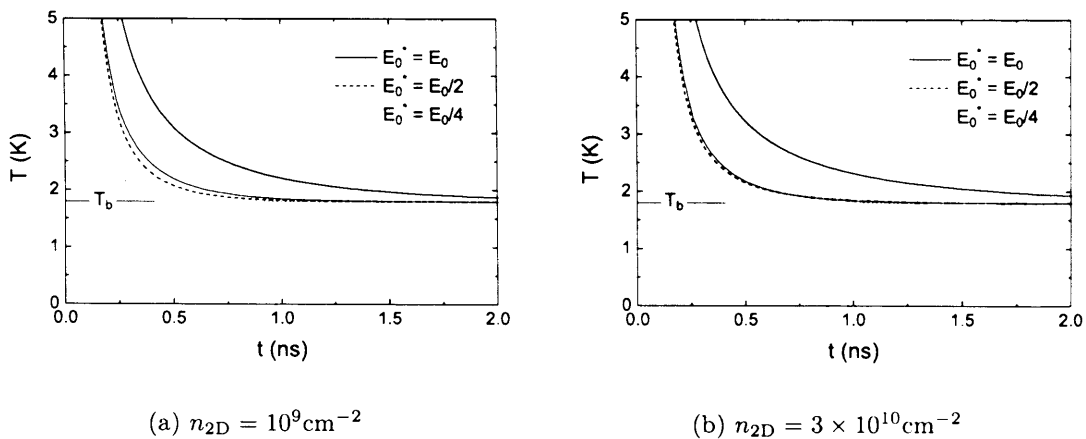
Figure 2.7: A plot of temperature against time for $T_b = 1.8\,\mathrm{K}$ and $T_i = 200\,\mathrm{K}$. The red lines show the results obtained with the Eq. 2.64 and the black lines show results obtained with Eq. 2.51. E_0 in is varied in Eq. 2.51 to show comparison with the red line.

This new, 'fitted' E_0 is called E_0^*, and a good estimate is $E_0^* = E_0/2$. Therefore, in the remainder of this thesis, wherever E_0 is used in equations, it is replaced by E_0^* in calculations.

(a) $n_{2D} = 10^9 \text{cm}^{-2}$ (b) $n_{2D} = 3 \times 10^{10} \text{cm}^{-2}$
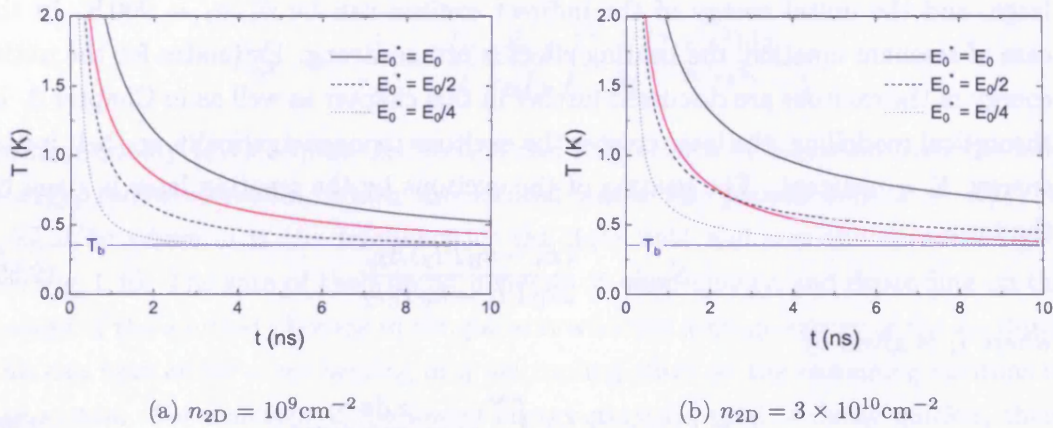
Figure 2.8: A plot of temperature against time for $T_b = 0.35\,\text{K}$ and $T_i = 200\,\text{K}$. The red lines show the results obtained with the Eq. 2.64 and the black lines show results obtained with Eq. 2.51.

2.8 CREATION AND DECAY OF EXCITONS

All the equations derived so far in this chapter assume a constant concentration of excitons with respect to time. In reality this is not the case because excitons are created (by focusing a laser on the sample), and they eventually decay (the electron and hole recombine, emitting PL). As mentioned in Section 1.9, in most experiments modelled in this thesis the laser that creates the excitons has a heating effect on the system, therefore cold excitons can be studied in two ways: (1) by conducting a time-resolved experiment by switching the laser on for a small amount of time then studying the excitons' behaviour after it is switched off, or (2) by conducting a spatially-resolved experiment, by using a constant laser power and studying the excitons' behaviour after they have moved away from the laser spot. By incorporating the effects of heating and cooling due to creation and decay of excitons into the basic equation of relaxational thermodynamics (Eq. 2.51) the first scenario can be modelled.

PUMP

As mentioned in Section 1.12, excitons can be created resonantly or nonresonantly. When indirect excitons are created nonresonantly, the heating by the laser pulse is large, and the initial energy of the indirect exciton can be $E_i/k_B \sim 200\,\mathrm{K}$. In the case of resonant creation, the heating effect is not as strong. Estimates for the initial energy of the excitons are discussed further in this chapter as well as in Chapter 3. In theoretical modelling, the laser creates the excitons monoenergetically, so their initial energy, $E_i = $ constant. The heating of the excitons by the creating laser is given by the term

$$S_{\mathrm{pump}} = \frac{(E_i - k_B T I_2)\Lambda_{T_0}}{2k_B T I_1 - k_B T_0 I_2},$$
(2.65)

where I_1 is given by

$$I_1 = (1 - e^{-T_0/T}) \int_0^\infty \frac{z\,\mathrm{d}z}{e^z + e^{-T_0/T} - 1},$$
(2.66)

and I_2 is given by

$$I_2 = e^{-T_0/T} \int_0^\infty \frac{z e^z\,\mathrm{d}z}{(e^z + e^{-T_0/T} - 1)^2}.$$
(2.67)

The term S_{pump} is the rate of change exciton temperature caused by the pump, and is always > 0.

The term Λ_{T_0} is given by

$$\Lambda_{T_0} = \frac{2\pi\hbar^2}{g k_B M_x} \Lambda(t),$$
(2.68)

where $\Lambda(t)$ is the exciton creation rate per cm^2 and is defined as

$$\Lambda(t) = \Lambda_0[\Theta(t) - \Theta(t - \tau_{\mathrm{pump}})].$$
(2.69)

The term in square brackets in this equation is a boxcar function comprising of two Heaviside step functions, which represents a pump that switches on at $t = 0$ and off at $t = \tau_{\mathrm{pump}}$.

OPTICAL DECAY

Optical decay equations were introduced in Section 1.11. The decay rate of excitons is given by Eq. 1.12, also shown here for clarity:

$$\Gamma_{\text{opt}} = \frac{1}{\tau_{\text{opt}}} = \frac{\Gamma_0}{2} \frac{E_\gamma}{k_B T_0} \int_0^1 \frac{(1+z^2)\mathrm{d}z}{Ae^{-z^2 E_\gamma/k_B T_\text{b}} - 1} .$$

In high-quality QWs a quasi-2D exciton can only emit a bulk photon from the low-energy, radiative modes, which are located inside the photon cone $k = k(\omega) = \sqrt{\varepsilon_{\text{B}}}\,\omega/\hbar c$ where ω is the frequency of the light field and c is the speed of light; see Fig. 1.10. The rate of their decay depends on their energy, and depending on the energy of the emitted photons in comparison with the average energy of the excitons, this can have either a net heating or a net cooling effect on the remaining excitons in the system. For example, if the lowest-energy particles tend to decay quicker, there is a net heating effect on the rest of the particles.

This effect is called 'recombination heating and cooling'. It is similar to the evaporative cooling techniques used in atomic optics to remove high-energy atoms from magnetic traps [31], but in this case the lowest-energy particles decay. This means that at relatively high temperatures, $k_\text{B} T > E_\gamma$, there is a net heating of the system. However, if the temperature of the system is very low, $k_\text{B} T \ll E_\gamma$ and most excitons lie within the photon cone, the effect can have a net heating or cooling effect; this is investigated in Section 2.8. This effect is given by

$$S_{\text{opt}} = \frac{(k_\text{B} T I_2 \Gamma_{\text{opt}} - E_\gamma \Gamma^{\text{E}}_{\text{opt}})T_0}{2k_\text{B} T I_1 - k_\text{B} T_0 I_2} . \tag{2.70}$$

where

$$\Gamma^{\text{E}}_{\text{opt}} = \frac{1}{\tau^{\text{E}}_{\text{opt}}} = \frac{\Gamma_0}{2} \frac{E_\gamma}{k_B T_0} \int_0^1 \frac{(1+z^4)\mathrm{d}z}{Ae^{-z^2 E_\gamma/k_B T_\text{b}} - 1} , \tag{2.71}$$

and I_1 and I_2 are given by Eqs. 2.66 and 2.67 respectively. The term S_{opt} is the rate of change of exciton temperature caused by their decay, and can be positive or negative.

INCLUDING S_{pump} AND S_{opt} INTO THE
RELAXATIONAL THERMODYNAMICS EQUATION

The final equation for the temperature dynamics of excitons is

$$\frac{\partial}{\partial t} T = \left(\frac{\partial T}{\partial t}\right)_{n_{2\text{D}}} + S_{\text{pump}} + S_{\text{opt}}, \tag{2.72}$$

where S_{pump} and S_{opt} are given above by Eqs. 2.65 and 2.70 respectively, and $\left(\frac{\partial T}{\partial t}\right)_{n_{2\text{D}}}$ is given by the basic equation of relaxational thermodynamics (Eq. 2.51), repeated here for clarity:

$$\left(\frac{\partial}{\partial t} T\right)_{n_{2\text{D}}} = -\frac{2\pi}{\tau_{\text{sc}}} \left(\frac{T^2}{T_0}\right) \left(1 - e^{-T_0/T}\right)$$

$$\times \int_1^\infty d\varepsilon\, \varepsilon \sqrt{\frac{\varepsilon}{\varepsilon - 1}} \frac{|F_z(a\sqrt{\varepsilon(\varepsilon - 1)})|^2}{(e^{\varepsilon E_0/k_\text{B}T_\text{b}} - 1)} \frac{e^{\varepsilon E_0/k_\text{B}T_\text{b}} - e^{\varepsilon E_0/k_\text{B}T}}{(e^{\varepsilon E_0/k_\text{B}T} + e^{-T_0/T} - 1)}.$$

Equation 2.72 is used to model the temperature dynamics of a quasi-2D exciton system. Various results can be obtained by using this equation, including the exciton temperature T, the excitons' optical lifetime τ_{opt}, the exciton concentration $n_{2\text{D}}$, the number of excitons in the ground state $N_{E=0}$, and the PL signal I_{PL} obtained from a relatively small angle, η ($\eta = 40^\circ$ or 8° in this thesis).

The PL signal, I_{PL}, is given by

$$I_{\text{PL}} = -E_t \frac{\partial n_{2\text{D}}}{\partial t} \tag{2.73}$$

where E_t is the minimum possible energy of the PL signal emitted by an exciton (also defined in Section 1.11).

RESULTS: VARYING Λ_0

Parameters are as stated in Section 1.10, the deformation potential, $D = 6.5\,\text{eV}$ which gives $\tau_{\text{sc}} = 215\,\text{ns}$, the pump $\Lambda(t)$ has a duration of $\tau_{\text{pump}} = 47\,\text{ns}$, $\tau_\text{R} = 6.75\,\text{ns}$, $T_\text{b} = 1.5\,\text{K}$, $T_\text{i} = 200\,\text{K}$ and the angle of detection of the PL signal is $\eta = 40^\circ$.

Results are shown here for two different excitation powers, $\Lambda_0 = 0.1 \times 10^{10}$ and $0.3 \times 10^{10}\,\text{cm}^{-2}\text{ns}^{-1}$. Figure 2.9 shows $n_{2\text{D}}$, T, $N_{E=0}$, τ_{opt} and I_{PL} plotted against t. For
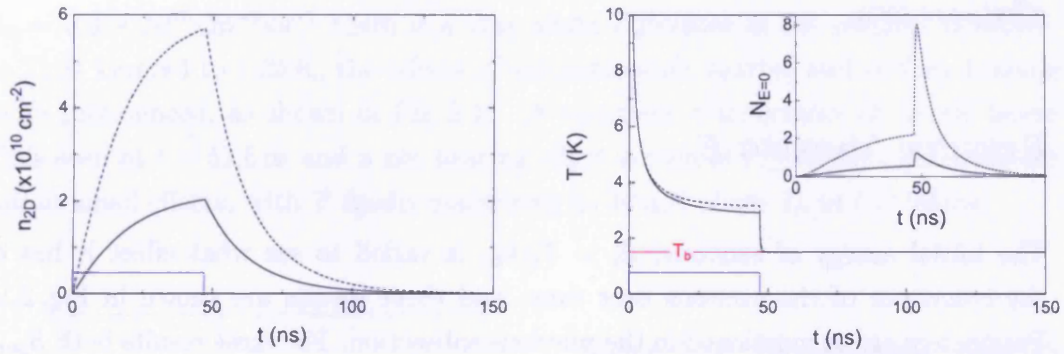
(a) The concentration plotted against time for two excitation powers.

(b) The temperature plotted against time for two excitation powers. Inset: the occupation number of the ground state, $N_{E=0}$, plotted against time.
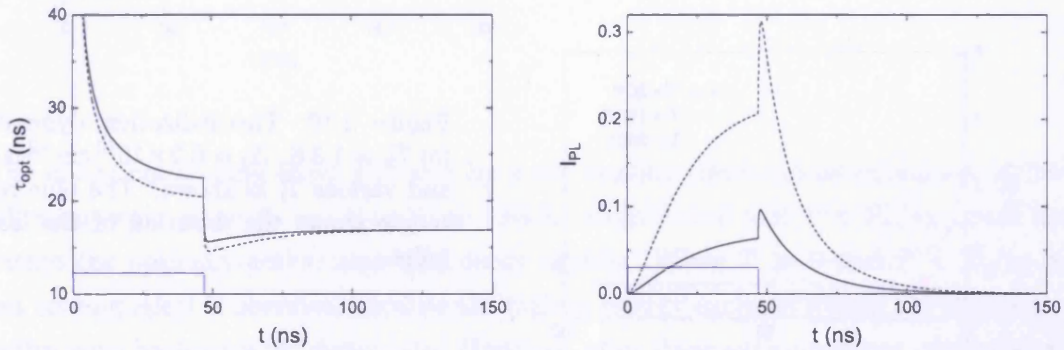
(c) The effective radiative lifetime of excitons plotted against time.

(d) The PL signal collected from an angle of $\eta = 40°$ plotted against time.

Figure 2.9: T, n_{2D}, τ_{opt}, I_{PL} and $N_{E=0}$ plotted against time for $T_b = 1.5\,\mathrm{K}$, $T_i = 200\,\mathrm{K}$ and two different excitation powers, $\Lambda_0 = 0.1 \times 10^{10}$ and $0.3 \times 10^{10}\,\mathrm{cm^{-2}ns^{-1}}$ (solid and dashed lines respectively). The blue rectangle shows the duration of the laser pulse.

these results both S_{pump} and S_{opt} are included. As expected, the concentration, and thus the occupation number of the ground state, is significantly higher for the larger excitation power. Here, $N_{E=0}^{max} \sim 8$ and the maximum concentration (at $t = \tau_{pump}$) is $n_{2D}^{max} = 5.7 \times 10^{10}$ cm^{-2}, which is high. The temperature is seen to stabilize at T_b within 5 ns after the end of the excitation pulse, and no significant heating or cooling effects are seen.

RESULTS: VARYING E_i

The initial energy of excitons, $E_i = T_i/k_B$, is varied to see what effect it has on the behaviour of the excitons over time, and these results are shown in Fig. 2.10. Parameters are as mentioned in the previous subsection. For these results both S_{pump} and S_{opt} are included. Figure 2.10 shows the temperature $T(t)$ when $T_b = 1.5$ K and $\Lambda_0 = 0.2 \times 10^{10}$ cm^{-2}ns^{-1}, for $T_i = 20$, 100 and 200 K. The maximum concentration in each case (at $t = \tau_{pump}$) is $n_{2D}^{max} = 3.1 \times 10^{10}$, 3.6×10^{10} and 3.9×10^{10} cm^{-2} respectively.

Figure 2.10: Thermalization dynamics for $T_b = 1.5$ K, $\Lambda_0 = 0.2 \times 10^{10}$ cm^{-2}ns^{-1} and various T_i as shown. The blue rectangle shows the duration of the laser pulse.

As is seen in Fig. 2.10, large variations in T_i affect $T(t < \tau_{pump})$. At the end of the pulse, $T_i = 20$ K produces $T = 1.9$ K and $T_i = 200$ K produces $T = 3.1$ K: in this example a factor of 10 change in T_i changes $T(t = \tau_{pump})$ by only a factor of 1.6. The variations in T_i only cause a negligible change in $T(t > \tau_{pump})$, although there is a significant difference in n_{2D}^{max}: for a lower T_i, n_{2D}^{max} is lower because more of the excitons are optically-active during the laser pulse ($t < \tau_{pump}$).

RESULTS: EFFECTS OF RECOMBINATION HEATING AND COOLING

Here, the effects of recombination heating and cooling are studied. Two sets of results are shown for each case: with and without recombination heating and cooling effects, S_{opt}. Parameters are the same as in the previous subsection. For $T_b = 1.5\,\mathrm{K}$ and $\Lambda_0 = 0.3 \times 10^{10}\,\mathrm{cm^{-2}ns^{-1}}$ there is a very slight difference in the results. However, as T_b is lowered to $1.25\,\mathrm{K}$, the effects of recombination heating and cooling become more pronounced, as shown in Fig. 2.11. A minimum temperature of $10\,\mathrm{mK}$ below T_b is seen at $t = 51.6\,\mathrm{ns}$ and a net heating effect is seen at $t \gtrsim 59.2\,\mathrm{ns}$, but both are rather small effects, with T finally stabilizing at $10\,\mathrm{mK}$ above T_b at $t \gtrsim 100\,\mathrm{ns}$.
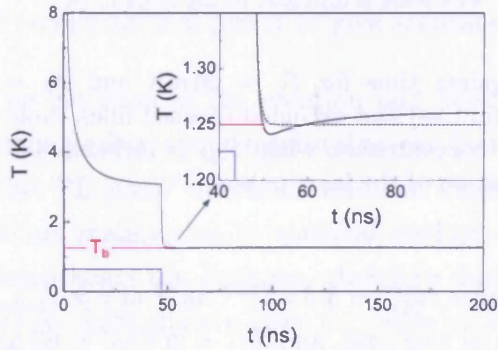
Figure 2.11: Thermalization dynamics for $T_b = 1.25\,\mathrm{K}$ and $\Lambda_0 = 0.3 \times 10^{10}\,\mathrm{cm^{-2}ns^{-1}}$ (and thus $n_{2D}^{max} = 5.6 \times 10^{10}\,\mathrm{cm^{-2}}$), with S_{opt} included (solid line) and with $S_{opt} = 0$ (dashed line). The blue rectangle shows the duration of the laser pulse.

The initial net cooling effect followed by a net heating effect can be explained in the following way: since $E_\gamma = 141\,\mu\mathrm{eV}$, or $1.64\,\mathrm{K}$, when $T > 0$ and $T < E_\gamma/k_B$, most lie within the optically-active zone and decay rapidly. When $T \gg 0$ and $T < E_\gamma/k_B$ a net cooling effect is observed because the highest energy excitons within the optically-active zone have a higher decay rate. However, after these excitons decay, their decay rate becomes smaller, because there are less of them and/or because they have cooled further (depending on the value of T_b), and the decay of the lowest energy excitons is dominant, creating a net heating effect.

For lower concentrations ($n_{2D}^{max} \sim 10^{10}\,\mathrm{cm^{-2}}$), the effect of recombination heating and cooling is much smaller for $T_b = 1.25\,\mathrm{K}$. For $\Lambda_0 = 0.1 \times 10^{10}\,\mathrm{cm^{-2}ns^{-1}}$ (hence $n_{2D}^{max} = 2.0 \times 10^{10}\,\mathrm{cm^{-2}}$), as T_b is lowered to $1\,\mathrm{K}$, the effect becomes noticeable, and a net heating effect is observed, with T stabilizing at $11\,\mathrm{mK}$ above T_b at $t \gtrsim 100\,\mathrm{ns}$ as before.

The effect is now studied for lower T_b. The results for $T_b = 50\,\mathrm{mK}$ are shown in

these results both S_{pump} and S_{opt} are included. As expected, the concentration, and thus the occupation number of the ground state, is significantly higher for the larger excitation power. Here, $N_{E=0}^{\text{max}} \sim 8$ and the maximum concentration (at $t = \tau_{\text{pump}}$) is $n_{\text{2D}}^{\text{max}} = 5.7 \times 10^{10} \, \text{cm}^{-2}$, which is high. The temperature is seen to stabilize at T_{b} within 5 ns after the end of the excitation pulse, and no significant heating or cooling effects are seen.

Results: Varying E_i

The initial energy of excitons, $E_i = T_i / k_{\text{B}}$, is varied to see what effect it has on the behaviour of the excitons over time, and these results are shown in Fig. 2.10. Parameters are as mentioned in the previous subsection. For these results both S_{pump} and S_{opt} are included. Figure 2.10 shows the temperature $T(t)$ when $T_{\text{b}} = 1.5 \, \text{K}$ and $\Lambda_0 = 0.2 \times 10^{10} \, \text{cm}^{-2} \text{ns}^{-1}$, for $T_i = 20$, 100 and 200 K. The maximum concentration in each case (at $t = \tau_{\text{pump}}$) is $n_{\text{2D}}^{\text{max}} = 3.1 \times 10^{10}$, 3.6×10^{10} and $3.9 \times 10^{10} \, \text{cm}^{-2}$ respectively.
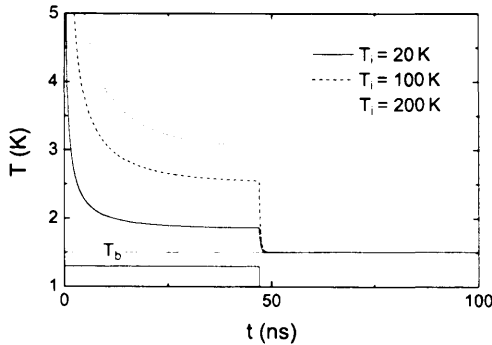

Figure 2.10: Thermalization dynamics for $T_{\text{b}} = 1.5 \, \text{K}$, $\Lambda_0 = 0.2 \times 10^{10} \, \text{cm}^{-2} \text{ns}^{-1}$ and various T_i as shown. The blue rectangle shows the duration of the laser pulse.

As is seen in Fig. 2.10, large variations in T_i affect $T(t < \tau_{\text{pump}})$. At the end of the pulse, $T_i = 20 \, \text{K}$ produces $T = 1.9 \, \text{K}$ and $T_i = 200 \, \text{K}$ produces $T = 3.1 \, \text{K}$: in this example a factor of 10 change in T_i changes $T(t = \tau_{\text{pump}})$ by only a factor of 1.6. The variations in T_i only cause a negligible change in $T(t > \tau_{\text{pump}})$, although there is a significant difference in $n_{\text{2D}}^{\text{max}}$: for a lower T_i, $n_{\text{2D}}^{\text{max}}$ is lower because more of the excitons are optically-active during the laser pulse ($t < \tau_{\text{pump}}$).

2.9 SUMMARY

The thermalization and photoluminescence dynamics of indirect excitons in GaAs/ AlGaAs CQWs at low lattice temperatures, $0.05 < T_b < 1.8\,\text{K}$, have been modelled theoretically and analysed in this chapter. This was done in two ways: (1) assuming $n_{2D} =$ constant, and (2) with additional creation and decay mechanisms thus $n_{2D} = n_{2D}(t)$.

Taking n_{2D} to be constant, a complete microscopic equation was 'fitted' to a simpler version of the equation, thus finding a value for E_0 that could be substituted into the simple equation in further work, $E_0^* = E_0/2$. This was necessary because the microscopic equation was very difficult to work with and needed an extensive amount of computational power to give accurate results.

The inclusion of the creation and decay mechanisms, as well as their heating and cooling effects, gave results that can be more accurately compared with experiments. The 'PL jump' effect discussed in literature [135, 136] is observed, and this effect occurs mainly due to classical cooling of the excitons after the pump pulse. The pump heats the excitons, therefore during the pump pulse they are less optically-active. Immediately after the pulse an increase of the PL signal is observed because the excitons become more optically-active; this is known as the PL jump.

The recombination heating and cooling effect can be described as the change of the effective temperature of indirect excitons due to their resonant optical decay. It is an interesting effect: both heating and cooling effects can be seen in a single simulation if $0 \ll T < E_\gamma$, but at $T \sim 0$ only a net cooling effect is observed. This effect benefits the experimentalists who would like to achieve a large occupation number of the ground state, but only if the experiments are carried out at low enough temperatures. This recombination heating and cooling effect is included in all further work in this thesis.
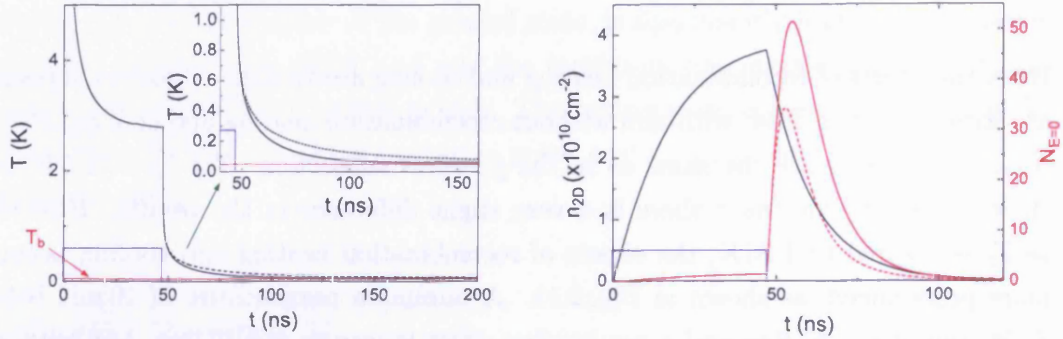
(a) Temperature plotted against time.

(b) Concentration and occupation number of the ground state plotted against time (black and red lines respectively). Note that the x-axis scale is different to the scale in (a).

Figure 2.12: T, n_{2D} and $N_{E=0}$ plotted against time for $T_b = 50\,\mathrm{mK}$ and $\Lambda_0 = 0.2 \times 10^{10}\,\mathrm{cm}^{-2}\mathrm{ns}^{-1}$, with S_{opt} included (solid line) and excluded (dashed line). Note that there is no significant difference in the concentration when S_{opt} is included and excluded. The blue rectangle shows the duration of the laser pulse.

Fig. 2.12. Here $\Lambda_0 = 0.2 \times 10^{10}\,\mathrm{cm}^{-2}\mathrm{ns}^{-1}$ (hence $n_{2D}^{max} = 3.8 \times 10^{10}\,\mathrm{cm}^{-2}$ at $t = \tau_{pump}$). Notice that only a net cooling effect is seen in this case, and $T(t = 200\,\mathrm{ns}) = 60$ and $70\,\mathrm{mK}$ for the cases when S_{opt} is included and excluded respectively. The occupation number of the ground state is $\gg 1$ and reaches a maximum of $N_{E=0} = 52$ at $t = 55.0\,\mathrm{ns}$.

Therefore, for the recombination heating and cooling effect to be observed, T has to be small enough and n_{2D} has to be large enough. However if T is very low ($T \ll 1\,\mathrm{K}$) only a net cooling effect is observed because a significant fraction of the excitons are in the optically-active zone, but the highest-energy excitons within the zone have a higher optical decay rate.

A larger excitation power creates a larger concentration of excitons, therefore, to obtain a large population of the ground state, a high Λ_0 and low T_b are needed. The results presented in this section show a maximum of $N_{E=0} = 52$ for $T_b = 50\,\mathrm{mK}$ and a concentration of $n_{2D}(t = \tau_{pump}) = 3.8 \times 10^{10}\,\mathrm{cm}^{-2}$, which is experimentally accessible.

3 DIFFUSION OF

QUANTUM WELL EXCITONS

In this chapter the microscopic theory developed for the long-range transport, thermalization and optical decay of excitons is explained, and the theoretical results are compared with experimental results. The quantum diffusion equation is introduced, then combined with temperature dynamics (from the previous chapter) and applied to a steady-state system of excitons in 2D. By fitting the theoretical results to the experimental data it is possible to obtain a good estimate for the diffusion coefficient and the amplitude of disorder in the system.

The screening of disorder is also discussed, and an explanation is given on how this effect is included in the equations. The mean-field energy conversion effect is also introduced, as well as the suppression of the optical decay of excitons due to their velocity.

3.1 BACKGROUND INFORMATION
AND PUBLISHED RESULTS

In this chapter a particular kind of experiment is described and modelled, where a laser (which creates the excitons) is focused onto a 2D CQW structure. The laser intensity profile is very similar to a Gaussian profile, and the created excitons move outwards from the excitation spot, cooling down while doing so. Some results from

this kind of experiment were published separately in Ref. [5] (by Butov *et al.*) and
[68] (by Snoke *et al.*). In Ref. [5], 2D images of the PL intensity in the $x - y$ plane
were shown, as well as the PL signal profile with respect to radius, and these are
reproduced in Figs. 3.1 and 3.2. Two PL rings can be seen surrounding the excitation
spot. One ring is small, with a radius $\sim 30\,\mu$m and the other is much larger, with a
radius $> 100\,\mu$m. The external ring is also fragmented into beads. In Ref. [68], only
the external ring is seen, and its radius can be as large as $\sim 500\,\mu$m. In this article
the PL intensity is viewed in the $E - x$ plane, and the 2D sample is not viewed from
the 'top' as in Ref. [5], therefore fragmentation of the ring would be very difficult
to see. However, in another article by one of authors of Ref. [68], the sample was
viewed from the 'top', but fragmentation of the ring was not seen [137]. Recently,
other experiments were conducted by this group on a single QW sample where only
direct excitons existed, and in this case they still observed the external ring but no
fragmentation [138].
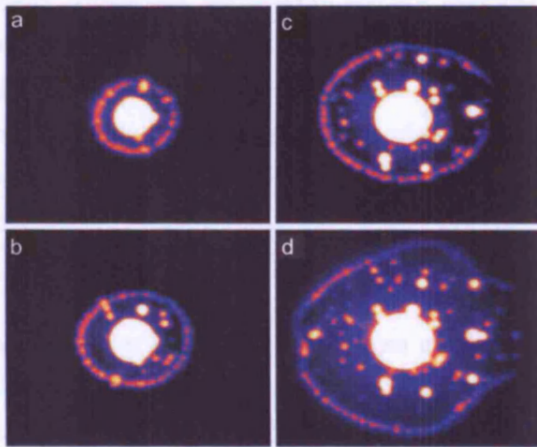
Figure 3.1: The dependence of the spatial pattern of the indirect exciton PL intensity on the excitation power. The lattice temperature, $T_b = 1.8\,$K, the gate voltage, $V_g = 1.22\,$V, and the excitation powers, P_{ex}, are as follows: (a) $290\,\mu$W, (b) $390\,\mu$W, (c) $690\,\mu$W and (d) $1030\,\mu$W. The area of view is $530 \times 440\,\mu$m. The colour represents the intensity of the PL signal where white represents maximum PL signal then yellow, red, purple and blue represent decreasing intensities and black represents no PL signal. Taken from Ref. [5].

The external ring of PL, which can be $> 100\,\mu$m in radius, has attracted a lot of
attention, and a lot of research is being carried out to investigate the source of this
ring. It is especially interesting since it segregates into beads, which are separated by
a constant distance along the ring. At first, it was thought that the excitons became
optically 'dark' after moving past the first ring, and became optically-active at the
position of the external ring. Two possible reasons for the excitons to be dark are:
(1) they have a high velocity, or momentum, and so their distribution in momentum
space is not isotropic, which means that less of the excitons are optically-active, and
(2) they have a high temperature, and so cannot optically decay. However, the ring
is now believed to be formed by a separation of electron and hole gases, with exciton
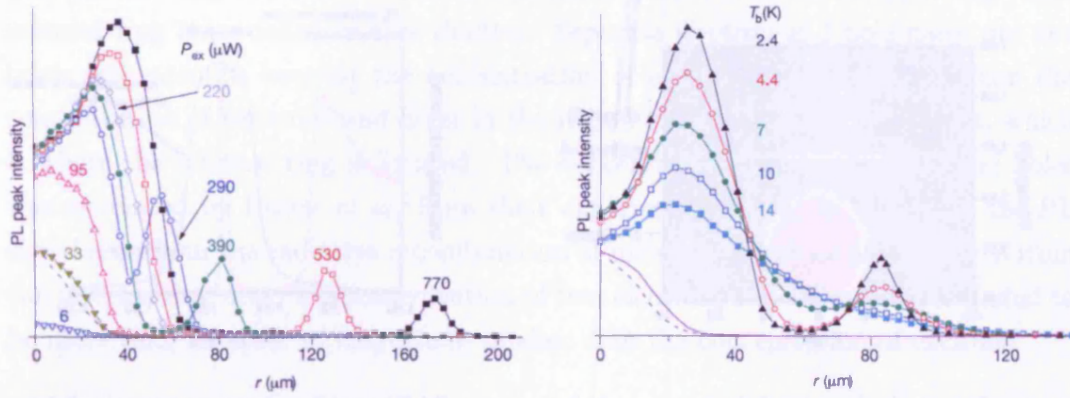
(a) $T_b = 1.8\,\text{K}$ and various excitation powers as shown.

(b) $P_{ex} = 390\,\mu\text{W}$ and various lattice temperatures as shown.

Figure 3.2: Power and temperature dependence of the peak PL intensity against radius, where the radius, r, is measured from the centre of the excitation spot. The gate voltage, $V_g = 1.22\,\text{V}$. The excitation laser intensity profiles are shown by the purple dashed lines. The solid purple line in (b) shows the peak intensity of the direct exciton PL. Here, the indirect exciton PL line is at $\sim 1.545 - 1.550\,\text{eV}$ and the direct PL line is at $\sim 1.570\,\text{eV}$. Taken from Ref. [5].

formation and recombination occuring at the position of the ring [138–144]. This would explain why no external ring is seen when the excitons are created *resonantly* [141].

In the experiments discussed in Ref. [5], only the internal ring is seen at low P_{ex}. As seen in Fig. 3.2(a), at $P_{ex} \simeq 95\,\mu\text{W}$ the internal ring appears, and with increasing power becomes more prominent and slightly larger, then at some critical point, the external ring appears; this external ring also becomes larger as the power is increased. In Fig. 3.2(b) the lattice temperature, T_b, is changed, and both the intensity and contrast of the internal ring decrease dramatically with increasing lattice temperature.

The appearance of this internal ring has not been reported elsewhere. This could be because in other experiments the laser excitation spot is not focused enough, or because the subtraction of the n^+ GaAs emission is not as accurate. As seen in Fig. 3.3(a), there is a broad line arising below the indirect exciton line, which is due to emission from the n^+ GaAs layers, and the subtraction of this is essential for visualization of the internal ring. This can be done using a band pass filter (see Fig. 3.3(b)), or by using computational methods (see Fig. 3.4).
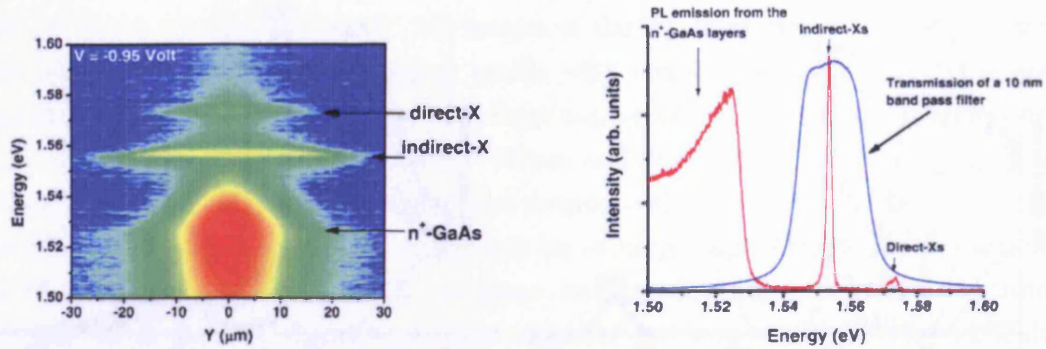
(a) A typical example of the spectra of the emitted PL with respect to distance from the excitation spot centre, Y. The colour represents the intensity of the light: blue is lowest, red is highest.

(b) The red line shows an example of the PL intensity emitted from the internal ring area, and the blue line shows the transmission of a 10 nm band pass filter which is used in the experiments.

Figure 3.3: These figures give an illustration of the n^+ GaAs emission and the way it is removed with a filter. Taken from Ref. [6].
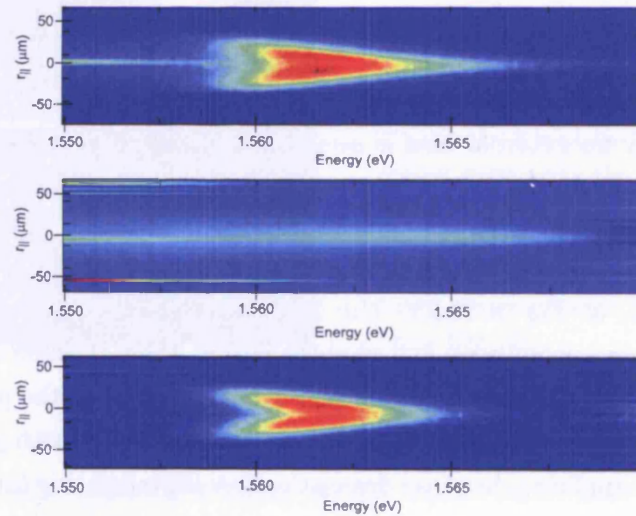
Figure 3.4: A typical example of the effect of n^+ GaAs emission removal in the $E - x$ plane. The colour represents the intensity of the light: dark red is highest, blue is lowest. The upper figure shows the raw data, the middle figure shows the n^+ GaAs emission, and the lower figure shows the data after n^+ GaAs emission removal. This data was taken for resonant excitation at $P_{ex} = 730 \, \mu W$, $V_g = 1.6 \, V$ and $T_b = 1.5 \, K$, and in this case, the removal of the n^+ GaAs emission was done by using computational methods. This data was taken by Butov $et \, al.$ [145].

The internal ring of PL has not drawn as much attention as the external ring. This internal ring is modelled in this chapter. Separate electron and hole gases are not taken into account because the concentration of excitons is much higher than the concentration of electrons and holes in the region close to the excitation spot, which is where the internal ring is located. The concentration of free electrons and holes was estimated by Butov *et al.* from their experimental data, by analysing the PL signal seen from the radiative recombination of unbound electrons and holes. Within the internal ring area, the concentration of free electrons and holes was concluded to be more than an order of magnitude smaller than the concentration of excitons.

The PL signal plots in Fig. 3.2 are discussed further in Section 3.5, where they are compared with theoretical data.

3.2 THEORY

QUANTUM DIFFUSION

The nonlinear quantum diffusion equation is given by [87]

$$\frac{\partial}{\partial t}n_{2D} = \nabla\left[D_x\nabla n_{2D} \;+\; \mu_x n_{2D}\nabla\left(u_0 n_{2D} + U_{QW}\right)\right] - \Gamma_{opt}n_{2D} + \Lambda. \qquad (3.1)$$

The first part in the square brackets is due to the diffusion of excitons, which originates from the concentration gradient. The second part in the square brackets is due to the drift motion of excitons, where the mobility, μ_x, is determined by the diffusion coefficient of the excitons, D_x, and given by a modified version of the Einstein relationship for bosons:

$$\mu_x = \frac{D_x}{k_B T_0}(e^{T_0/T} - 1). \qquad (3.2)$$

When $T \gg T_0$ this equation reduces to the Einstein relationship, $\mu_x = D_x/k_B T$. In the quantum limit the modified Einstein relationship gives a strong increase of the mobility for higher n_{2D}.

Variations in the QW potential due to disorder is given by U_{QW}, and this is discussed in Section 3.3. The mean-field potential is given by $u_0 n_{2D}$ and arises due to the dipole-dipole repulsion of indirect excitons; u_0 is defined in Section 3.3. Therefore at high densities the excitons feel a strong pressure-like force, which in turn causes a

drift velocity of excitons, $v_{\text{drift}} \propto \nabla n_{2D}$.

The term $\Gamma_{\text{opt}} n_{2D}$ is due to the optical decay of excitons, where Γ_{opt} is given by Eq. 1.12. The term $\Lambda = \Lambda(r_\parallel)$ gives the generation rate of excitons per cm^2.

THERMALIZATION KINETICS

Most of this theory is introduced in Chapter 2, thus only a brief summary is given here. One other effect is introduced in this chapter, called mean-field energy conversion. This effect is discussed in Section 3.6, and is incorporated into the set of equations. A steady-state situation is modelled in this chapter, so terms which depended on time, t, previously, depend only on the in-plane coordinate, $r_\parallel$, here. The in-plane coordinate is measured from the centre of the excitation spot and is referred to as the radius.

In the model, the exciton temperature is affected by three processes: (i) heating due to the optical excitation, because the initial energy of the excitons can be high (this depends on the energy of the laser), (ii) heating/cooling due to the optical decay of the lowest-energy excitons, and (iii) heating due to LA-phonon assisted conversion of the mean-field energy into internal energy. The first two effects are introduced and discussed in Section 2.8, and the third effect is introduced and discussed in Section 3.6.

The temperature dynamics of excitons is given by Eq. 2.72, also repeated here for clarity:

$$
\begin{aligned}
\frac{\partial}{\partial t} T = & -\frac{2\pi}{\tau_{\text{sc}}} \left(\frac{T^2}{T_0}\right) (1 - e^{-T_0/T}) \int_1^\infty d\varepsilon \, \varepsilon \sqrt{\frac{\varepsilon}{\varepsilon - 1}} \left| F_z \left(a\sqrt{\varepsilon(\varepsilon - 1)}\right) \right|^2 \\
& \times \left(\frac{e^{\varepsilon E_0/k_B T_b} - e^{\varepsilon E_0/k_B T}}{e^{\varepsilon E_0/k_B T} + e^{-T_0/T} - 1}\right) \left(\frac{1}{e^{\varepsilon E_0/k_B T_b} - 1}\right) + S_{\text{pump}} + S_{\text{opt}}.
\end{aligned}
$$

As stated in Section 2.7, $E_0^* = E_0/2$ is used instead of E_0. The term $\Lambda_{T_0} = [(\pi\hbar^2)/(2k_B M_x)]\Lambda(r_\parallel)$ and the generation rate of excitons per cm^2 is a spatial Gaussian function:

$$
\Lambda(r_\parallel) = \Lambda_0 e^{-r_\parallel^2/2\sigma^2} , \tag{3.3}
$$

and the full width at half maximum (FWHM) of the function $= 2\sqrt{2\ln 2}\,\sigma$. The initial injected energy of the excitons is given by $E_i = k_B T_i$.

Equations 1.12, 2.72 and 3.1 are solved numerically for a stationary, cylindrically-symmetric Gaussian-shaped optical excitation, $\Lambda(r_{\parallel})$. The system is assumed to be cylindrically-symmetric and the equations are solved in the radial direction, from $r_{\parallel} = 0$ to $r_{\parallel}^{\mathrm{max}}$, where $r_{\parallel}^{\mathrm{max}}$ is the distance where $n_{\mathrm{2D}} \to 0$. Before the theoretical and experimental results are presented, the effects of disorder are discussed.

3.3 DISORDER

The concept of disorder is introduced in Section 1.13. The QW structures used in experiments are grown by molecular beam epitaxy methods, and have small thickness fluctuations. This results in a variation in well and barrier thicknesses, and therefore a variation in the confining potential in the QW, which contributes to an inhomogeneous broadening of the exciton linewidth. There is a resulting in-plane potential variation, and if the scale of disorder is larger than the exciton Bohr radius the excitons tend to avoid the local potential maxima and collect in the local potential minima; this is illustrated in Fig. 3.5. This varying in-plane potential is represented in the quantum diffusion equation (Eq. 3.1) by the term U_{QW}.
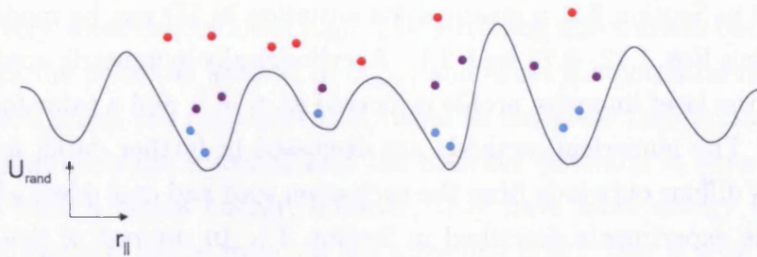
Figure 3.5: A schematic diagram of excitons experiencing a random in-plane potential, U_{rand} (not to scale). The coldest excitons (blue dots) tend to lie at the potential minima, and the hottest excitons (red dots) have more energy and can overcome the potential maxima.

At low temperatures, these excitons are trapped in the minima because they don't have enough thermal energy to escape. If the concentration of excitons is high, the disorder can be screened by the repulsive dipole-dipole interaction between the excitons.

SCREENING OF LONG-RANGE CORRELATED DISORDER

The screening of long-range correlated disorder arises due to the repulsive interaction between excitons. The term 'long-range' refers to µm length scales. The dipole-dipole repulsion between excitons causes a blue-shift of the indirect exciton PL emission energy, E_{shift}, with increasing n_{2D}; this blue-shift has been observed in many experiments (*e.g.* see Ref. [65]). The PL emission energy is shifted by

$$E_{shift} = u_0 n_{2D},$$ (3.4)

where the mean-field energy amplitude u_0 is given by

$$u_0 = \frac{4\pi e^2 d_z}{\varepsilon_B},$$ (3.5)

ε_B is the background dielectric constant and $E_{shift} \simeq 1.6\,\text{meV}$ for $n_{2D} = 10^{10}\,\text{cm}^{-2}$. This equation is valid when the distance between the electron and hole layers, $d_z \geq a_{2D}^B$, where a_{2D}^B is the 2D exciton Bohr radius.

By using the quantum diffusion equation (Eq. 3.1), it is possible to show how the excitons screen long-range correlated disorder in the QWs by dipole-dipole interaction. As discussed in Section 3.2, a steady-state situation in 1D can be modelled theoretically by using Eqs. 1.12, 2.72 and 3.1. A cylindrically-symmetric spatial Gaussian function for the laser intensity profile is located at $r_\parallel = 0$, and a value for $n_{2D}(r_\parallel = 0)$ is assumed. The numerical methods are discussed in further detail in Section 3.4. The excitons diffuse outwards from the excitation spot and cool down while doing so, just as in the experiments described in Section 3.1. In the rest of this chapter, the disorder is not included directly as a function as it is here because the actual shape of the disorder is unknown; therefore only the amplitude, U^0, is used. However, here, an arbitrary potential, $U_{QW} = U_{rand} = -\frac{U^0}{2}\cos(r_\parallel)$, is included directly into the diffusion equation (Eq. 3.1) to demonstrate the effect of screening.

Figure 3.6 shows the results for the following parameters: $D = 9.6\,\text{eV}$, $\tau_R = 13\,\text{ns}$, $T_b = 1.5\,\text{K}$, $n_{2D}^{max} = 4 \times 10^{10}\text{cm}^{-2}$, $\Lambda_0 = 1.24 \times 10^{10}\,\text{cm}^{-2}\text{ns}^{-1}$, $T_i = 1000\,\text{K}$, FWHM of the excitation function $= 6.1\,\mu\text{m}$ (therefore $\sigma = 2.6\,\mu\text{m}$), $\eta = 8°$, $U^0 = 0.9\,\text{meV}$ and a constant diffusion coefficient $D_x = D_x^c = 25\,\text{cm}^2/\text{s}$. The upper plot in Fig. 3.6 shows the effective potential $U_{eff} = U_{rand} + u_0 n_{2D}(r_\parallel)$, and the potential that was used, $U_{rand} = -\frac{U^0}{2}\cos(r_\parallel)$, is plotted in the lower plot. It is clear that the disorder
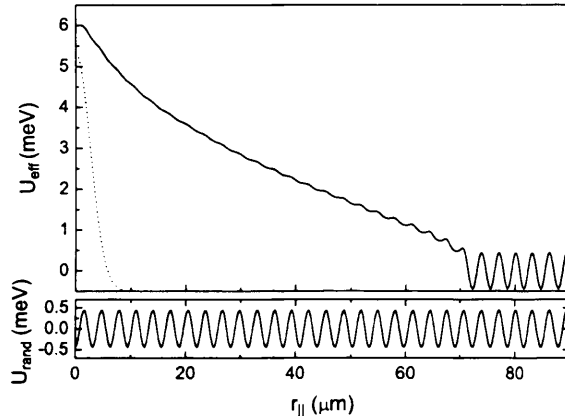
Figure 3.6: Screening of the long-range-correlated disorder potential, U_{rand}, by dipole-dipole interacting indirect excitons. On the upper plot, the effective potential, $U_{\text{eff}} = U_{\text{rand}} + u_0 n_{2D}(r_{\|})$, is plotted (solid line) as well as the laser intensity profile (dotted line). A random potential is modelled by the sinusoidal potential, U_{rand}, which is plotted in the lower plot.

potential screening is more effective for higher densities and lower temperatures: near $r_{\|} \sim 0$ the screening is not as effective (here $T \simeq 12\,\text{K}$), and also at $r_{\|} \gtrsim 60\,\mu\text{m}$ the screening is very weak due to lower n_{2D}. The screening effect arises because excitons accumulate in the potential minima of U_{rand}, and avoid the potential maxima. Since they repel each other, the local potential *raises* in the areas they accumulate, hence the potential minima are screened and the disorder potential is smoothed. When the excitons have a higher energy, however, they have more energy to move from the potential minima, hence reducing the screening effect; this is why the screening effect at $r_{\|} \sim 0$ is weaker. The screening effect becomes significant for concentrations, $n_{2D} \gtrsim 10^{10}\,\text{cm}^{-2}$.

It is possible to include the disorder effects directly into the diffusion equation by using a thermionic model [87]. The diffusion coefficient, D_x, is replaced with

$$D_x^{\text{d}} = D_x^0 e^{-U^0/(k_B T + u_0 n_{2D})} , \tag{3.6}$$

where D_x^0 is a constant. Results with and without this thermionic model are presented in Section 3.5.

3.4 Numerical Methods

Fitting Parameters for all Excitation Powers

Since various laser excitation powers were used in the experiments, the fit parameters not only have to be appropriate for data taken with a particular laser power, but for the whole range of powers used. The laser excitation power, P_{ex}, does not appear explicitly in the equations; instead, the number of particles created per cm^2 per ns is used, and is given by Λ in Eq. 3.3. It is possible that Λ_0 does not scale linearly with P_{ex} because the creation of excitons is likely to become less efficient at higher excitation powers. Therefore, the concentration in each case is estimated by measuring the blue-shift of the exciton energy, E_{shift}, and using Eq. 3.4. Then Λ_0 is found for that particular concentration.

Computational Work

A steady-state situation is modelled, therefore $\frac{\partial}{\partial t}T = 0$ and $\frac{\partial}{\partial t}n_{2D} = 0$, therefore Eqs. 2.72 and 3.1 are both equal to zero. A bisection method is adopted to find the value for Λ_0, and the code works in the following way:

- At $r_\parallel = 0$, the concentration, n_{2D} is known, and an estimated value for the temperature, $T(r_\parallel = 0)$ and Λ_0 are included in the input file.

- By using Eq. 1.12, Γ_{opt} is found.

- By using Eq. 2.72, the temperature for the next step in space can be found by knowing that $\frac{\partial}{\partial t}T = 0$ and using the value found for Γ_{opt}. Then the concentration, n_{2D}, is also obtained for the next step in space by using Eq. 3.1 to calculate the concentration gradient, ∇n_{2D}. Γ_{opt} is also calculated for the same step in space.

- After a few space steps, a reasonable value for $T(r_\parallel = 0)$ is obtained by averaging over the first few calculated values, and the program returns to $r_\parallel = 0$ with this estimate for $T(r_\parallel = 0)$.

- The code starts again from $r_\parallel = 0$ and moves from one space step to the next by calculating values for Γ_{opt}, n_{2D} and T each time.

- This is repeated for more space steps until an instability develops, and n_{2D} either becomes negative or goes to infinity. If it becomes negative, this is an indication that Λ_0 is too large, so the code stops and returns to $r_\parallel = 0$ with a smaller value for Λ_0. In the opposite way, if n_{2D} tends to infinity, this is an indication that Λ_0 is not large enough.

- This process is repeated until Λ_0 converges towards a particular value and $n_{2D} \rightarrow 0$ as $r_\parallel \rightarrow \infty$.

This process can also be changed so that n_{2D} is adjusted to fit a particular value of Λ_0. However, since Λ_0 cannot be measured directly from experiments whereas n_{2D} can be estimated, fitting Λ_0 to a particular value of n_{2D} is more appropriate.

ADJUSTING THE DIFFUSION COEFFICIENT
AND DISORDER AMPLITUDE

The first diffusion coefficient used is a constant number, D_x^c. When using this, the asymptotic solution for radius, $r_\parallel \gg 0$ is $I_{PL} \propto \exp[-(\Gamma_{opt}/D_x)^{1/2}r_\parallel]$. In contrast, the PL profile in the experimental data has a steep decay and a *spatial pinning* at a critical radius: the PL signal decreases from a maximum at the ring radius, $r_\parallel^{rg}$, to zero very abruptly. This is illustrated in Fig. 3.2(a). This steep decay and spatial pinning is due to the lack of screening of long-range QW disorder at lower concentrations (discussed in Section 3.3). In order to include the disorder in the model, a thermionic model is used, given by Eq. 3.6. The effects of using this equation are discussed in the next section.

3.5 NONRESONANT EXCITATION:
INITIAL THEORETICAL RESULTS

Although the theoretical results presented in this section can be compared with the main features of the experimental results in Fig. 3.2, note that in the experimental plots, only the maximum PL signal is plotted, and not the total PL signal from the whole collection angle, η, as is done in the theoretical work. Therefore it is not possible to make a direct comparison.

In experiments, the PL signal and concentration profile of excitons can be obtained, and by fitting the theoretical results to these results as described above, it is then possible to obtain much more information on the system.

In these simulations $D = 6.5\,\mathrm{eV}$, $\tau_R = 6.75\,\mathrm{ns}$, the FWHM of the excitation laser profile $= 30.0\,\mu\mathrm{m}$ (thus $\sigma = 12.74\,\mu\mathrm{m}$) and $\eta = 8°$. An estimate of $T_i = 300\,\mathrm{K}$ is used for $T_b = 1.8\,\mathrm{K}$.

RESULTS AT $T_b = 1.8\,\mathrm{K}$

Figure 3.7 shows the PL signal in the $x - y$ plane, and Fig. 3.8 shows the same data, but PL signal is plotted against radius. Figure 3.8 shows that for a constant diffusion coefficient, $D_x = D_x^c$, the PL signal and concentration decay exponentially outside the first ring. As stated in Section 3.4, this is in contrast with experimental results which show a much steeper decay of the PL signal. The reason for this steeper decay is the lack of the n_{2D}-dependent screening of disorder at larger radius, due to a smaller concentration of excitons.

If the thermionic model is included into the equation for diffusion coefficient, giving Eq. 3.6, there is a much steeper decay of the PL signal, which is more consistent with experimental data [146], see Figs. 3.2(a), 3.7 and 3.8. In this case the diffusion coefficient decreases with increasing radius, see Fig. 3.11(b), and as it decreases and approaches zero this causes a spatial pinning of the ring.

The calculated PL signal against radial distance from the centre of the laser excitation spot is plotted in Fig. 3.9, and the appearance of the internal ring is clearly seen. At the lowest excitation powers there is no ring, and I_{PL} is a maximum at $r_\parallel = 0$. As the power is increased, the PL ring appears around the excitation spot, at $r_\parallel^{rg} \simeq 30\,\mu\mathrm{m}$. Both the radius and the intensity of this ring increase with increasing excitation power or decreasing T_b. Although the results cannot be compared directly to the experimental data in Fig. 3.2, the main features are the same: in experiments, for low excitation powers and/or high T_b there is no internal ring, then as P_{ex} is increased and/or T_b is lowered a ring appears. The ring radius, $r_\parallel^{rg}$, increases as the PL intensity is increased; in a similar way, as T_b is lowered $r_\parallel^{rg}$ increases.

The origin of the internal ring is nearly classical and arises due to heating of indirect excitons by the optical excitation, the S_{pump} term in Eq. 2.72. By using $E_i/k_B =$
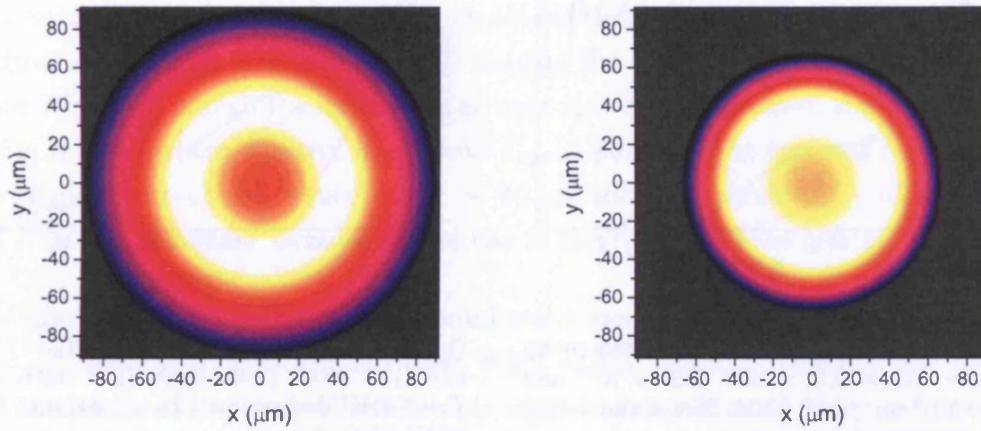
(a) Constant diffusion coefficient, $D_x = D_x^c = 100\,\mathrm{cm^2/s}$.

(b) Thermionic model $(D_x = D_x^d)$ with $D_x^0 = 120\,\mathrm{cm^2/s}$ and $U^0 = 1.0\,\mathrm{meV}$.

Figure 3.7: The PL signal in the $x - y$ plane, where white represents the highest intensity, then yellow, red, purple and blue represent decreasing intensities and black represents no PL signal. In these two plots, $T_b = 1.8\,\mathrm{K}$, $\Lambda_0 = 0.48 \times 10^{10}\,\mathrm{cm^{-2}ns^{-1}}$ and $T_i = 300\,\mathrm{K}$.
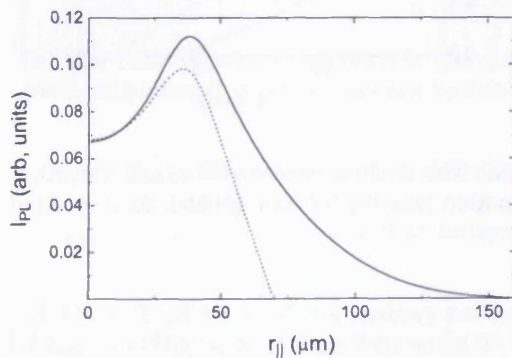
Figure 3.8: PL signal plotted against radius using a constant diffusion coefficient, $D_x = D_x^c = 100\,\mathrm{cm^2 s^{-1}}$ (solid line) and the thermionic model, $D_x = D_x^d$, where $D_x^0 = 120\,\mathrm{cm^2 s^{-1}}$ and $U^0 = 1.0\,\mathrm{meV}$ (dotted line). Here, $T_b = 1.8\,\mathrm{K}$, $\Lambda_0 = 0.48 \times 10^{10}\,\mathrm{cm^{-2}ns^{-1}}$ and $T_i = 300\,\mathrm{K}$. Same results as in Fig. 3.7.

(a) $T_b = 1.8\,\mathrm{K}$, $T_i = 300\,\mathrm{K}$ and various pump powers: $\Lambda_0 = 0.12 \times 10^{10}$, 0.30×10^{10} and $0.48 \times 10^{10}\,\mathrm{cm}^{-2}\mathrm{ns}^{-1}$ (solid, dashed and dotted lines respectively).

(b) $\Lambda_0 = 0.48 \times 10^{10}\,\mathrm{cm}^{-2}\mathrm{ns}^{-1}$ and $T_b = 7.0\,\mathrm{K}$ and $T_i = 800\,\mathrm{K}$ (solid line), $T_b = 4.0\,\mathrm{K}$ and $T_i = 600\,\mathrm{K}$ (dashed line), $T_b = 1.8\,\mathrm{K}$ and $T_i = 300\,\mathrm{K}$ (dotted line).
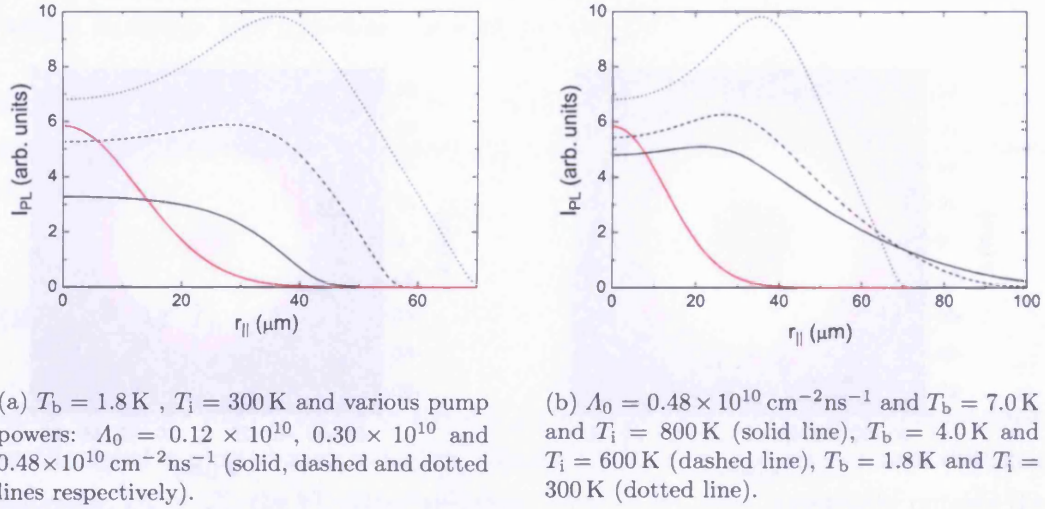
Figure 3.9: PL signal plotted as a function of radius. Other parameters are the same as for Fig. 3.7(b). The optical excitation profile is shown by the red line in both (a) and (b).
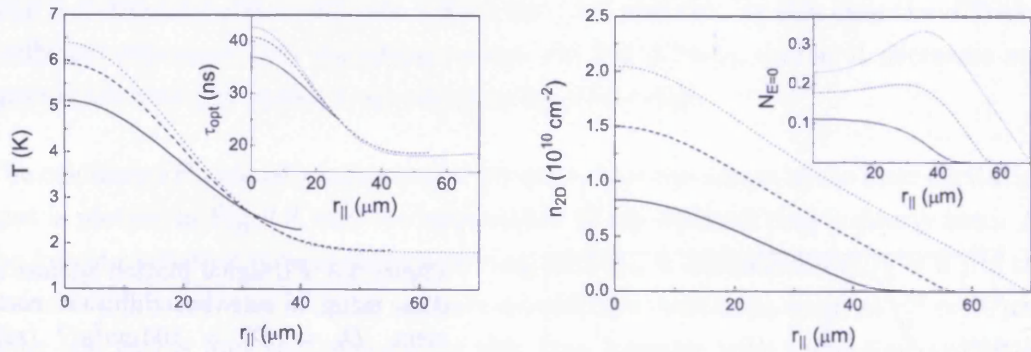
(a) A plot of the exciton temperature and optical lifetime against radius.

(b) The exciton concentration and the occupation number of the ground state plotted against radius.

Figure 3.10: T, τ_{opt}, n_{2D} and $N_{E=0}$ plotted against radius, for $T_b = 1.8\,\mathrm{K}$, $T_i = 300\,\mathrm{K}$ and various pump powers: $\Lambda_0 = 0.12 \times 10^{10}$, 0.30×10^{10} and $0.48 \times 10^{10}\,\mathrm{cm}^{-2}\mathrm{ns}^{-1}$ (solid, dashed and dotted lines respectively).

300 K, the exciton temperature at the laser spot is $T^{max} \simeq 6.5$ K which is much larger than $T_b = 1.8$ K (see Fig. 3.10(a)). The temperature $T(r_\parallel = 0)$ is expected to be higher if T_i is higher, and also if P_{ex} (or Λ_0) is higher. Both these statements were verified in experiments by Yoon et al.; see Ref. [98] and references therein. The exciton temperature decreases rapidly outside the excitation spot, see Fig. 3.10(a). Since $T(r_\parallel \sim 0)$ is high the optical decay near $r_\parallel = 0$ is suppressed; this is illustrated in Fig. 3.10(a) where effective decay rate Γ_{opt} is plotted. The excitons cool down to the temperature of the lattice at $r_\parallel^{rg} \sim 40$ μm and as a result the optical lifetime $\tau_{opt} = 1/\Gamma_{opt}$ decreases, causing a local rise in $I_{PL}(r_\parallel)$; this is the internal ring of PL.

The maximum population of the ground state mode, $N_{E=0} = e^{T_0/T} - 1$, occurs at $r_\parallel = r_\parallel^{rg}$, see Fig. 3.10(b). In this case, $N_{E=0}^{max} \sim 0.3$, which is relatively low because the maximum concentration here is only $n_{2D}^{max} \simeq 2 \times 10^{10}$ cm^{-2} at $r_\parallel = 0$, and the degeneracy temperature, $T_0 \propto n_{2D}$. Therefore, in this case the system behaves nearly classically, and Bose-Einstein statistics are only very weakly developed. To obtain a higher ground state occupancy, T_b could be lowered, and/or Λ could be increased [146, 147].
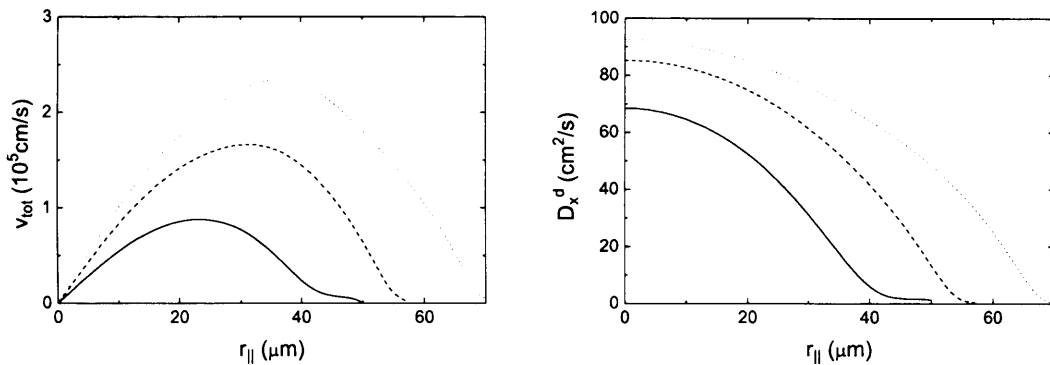
(a) The total velocity of excitons in the outward radial direction plotted against radius.

(b) The diffusion coefficient plotted against radius.

Figure 3.11: The velocity and diffusion coefficient for $T_b = 1.8$ K, $T_i = 300$ K and $\Lambda_0 = 0.12 \times 10^{10}$, 0.30×10^{10} and 0.48×10^{10} cm^{-2}ns^{-1} (solid, dashed and dotted lines respectively).

In Fig. 3.11(a) the total velocity of the excitons, v_{tot}, is plotted for the three different excitation powers. The maximum velocity, v_{tot}^{max}, occurs at the position of the PL ring, $r_\parallel^{rg}$. In these simulations, the disorder amplitude is approximated to be $U^0 = 1$ meV, and the diffusion coefficient, $D_x = D_x^d$, is in the range of $0 \lesssim D_x^d \lesssim 100$ cm^2/s, as

shown in Fig. 3.11(b), and in this case $D_x^0 = 120 \, \text{cm}^2/\text{s}$.

3.6 MEAN-FIELD ENERGY CONVERSION

The mean field energy arises due to the repulsion between the excitons and gives rise to a potential energy gradient, and therefore an in-plane drift motion. The possibility of estimating the concentration in experiments from the exciton energy blue-shift at higher concentrations has already been discussed in Section 3.4. The equation for this concentration-dependent energy shift is Eq. 3.4. The mean-field energy also results in a screening of in-plane disorder, which is discussed in Section 3.3.

Mean-field energy *conversion* refers to mean-field energy that is converted into the excitons' internal energy. This happens when the average velocity of the particles decreases very quickly, but their energy still remains high. This effect is due to scattering: the total vector sum of the velocities nearly cancel out, but the total energy is still large. In all calculations so far, the mean-field energy conversion is not included. However, the effect is rather small in the above cases, and including the extra term has no significant effect on the data. The effect is expected to be large when $k_B T \gg E_0$ ($E_0/k_B \simeq 0.4 \, \text{K}$), when the momentum relaxation time is much less than τ_{th}, and therefore the effect is large when ∇n_{2D} is large.

Heating of excitons by mean-field energy conversion to internal energy is included in Eq. 2.72 by adding an additional term, S_d, to the RHS. A new term, S_T, is defined as follows:

$$S_T = S_{\text{pump}} + S_{\text{opt}} + S_d \, , \tag{3.7}$$

where

$$S_d = -\frac{T_0 u_0 (\boldsymbol{v}_{\text{tot}} \cdot \nabla n_{2D})}{2 k_B T I_1 - k_B T_0 I_2} \, . \tag{3.8}$$

Here, the total velocity $\boldsymbol{v}_{\text{tot}}$ is the sum of the diffusion velocity, $\boldsymbol{v}_{\text{diff}} = -(D_x/n_{2D}) \nabla n_{2D}$ and the drift velocity $\boldsymbol{v}_{\text{drift}} = -\mu_x u_0 \nabla n_{2D}$. The integrals I_1 and I_2 are given by Eqs. 2.66 and 2.67.

This mean-field energy conversion effect is included from now on unless otherwise

noted. The final equation used from this point onwards is therefore

$$
\frac{\partial}{\partial t} T = -\frac{2\pi}{\tau_{sc}} \left(\frac{T^2}{T_0} \right) (1 - e^{-T_0/T}) \int_1^\infty d\varepsilon\, \varepsilon \sqrt{\frac{\varepsilon}{\varepsilon - 1}} \left| F_z \left(a\sqrt{\varepsilon(\varepsilon - 1)} \right) \right|^2
$$
$$
\times \left(\frac{e^{\varepsilon E_0/k_B T_b} - e^{\varepsilon E_0/k_B T}}{e^{\varepsilon E_0/k_B T} + e^{-T_0/T} - 1} \right) \left(\frac{1}{e^{\varepsilon E_0/k_B T_b} - 1} \right) + S_T, \tag{3.9}
$$

where S_T is given by Eq. 3.7.

3.7 NONRESONANT EXCITATION: DIRECT COMPARISON WITH EXPERIMENTS

Another set of experimental data was obtained specifically for the purpose of making a comparison with the theoretical model, therefore the PL signal was integrated over the whole collection angle, η. The theoretical data could then be compared directly with the experimental data. This data was obtained at $T_b = 1.5$ K.

The experiments were carried out by L. V. Butov's group in the University of California at San Diego. The PL pattern was imaged by a nitrogen-cooled CCD camera, and a band-pass filter was adjusted to the indirect exciton energy, as mentioned in Section 3.1, so that the n^+ GaAs emission is removed. If it is not removed, the internal ring of PL can be missed. The experiments that were carried out for this work concentrated mainly on the internal ring of PL, so the laser spot was kept small, FWHM $= 6.16\,\mu m$ (thus $\sigma = 2.62\,\mu m$).

In the experiments discussed in this section, the excitation was done with a HeNe laser at 633 nm. This excitation energy is *nonresonant*. In Section 3.8 of this chapter results obtained using resonant excitation with a Ti:Sapphire laser at 780 nm are also modelled.

The experimental results presented here have two sets of data for every excitation power: the position of the exciton line (or energy of the emitted photon), $E_{shift}(r_\parallel)$, from which the concentration can be calculated, and the PL profile, $I_{PL}(r_\parallel)$. By fitting the theoretical results to the experimental results it is possible to deduce values for the two unknown parameters: the disorder amplitude and diffusion coefficient. The computational code was ran several times with different estimates for the diffusion coefficient and disorder potential until a good fit to the experimental data

was obtained. In the next section, an improvement to the equation for the diffusion coefficient (Eq. 3.6) is discussed.

IMPROVING THE DIFFUSION COEFFICIENT

It is impossible to get a good fit for the diffusion coefficient when $D_x = D_x^d$ (given by Eq. 3.6) because there isn't one value for D_x^0 that fits the results for all the different excitation powers, P_{ex}. Another, more complicated, equation is used instead of D_x^0 in Eq. 3.6, given by

$$\tilde{D}_x^0 = \frac{D_{x-x}D_{x-ph}}{D_{x-x} + D_{x-ph}}.$$
(3.10)

This diffusion coefficient has two contributions: self-diffusion due to exciton-exciton scattering, given by $D_{x-x} = C_{x-x}(T/T_0)$, and diffusion due to LA-phonon scattering, given by $D_{x-ph} = D_{x-ph}(T_b)$. The constants C_{x-x} and D_{x-ph} have to be fitted from the experimental results. If the thermionic model is also used, the final equation obtained for the diffusion coefficient is

$$\tilde{D}_x^d = \frac{D_{x-x}D_{x-ph}}{D_{x-x} + D_{x-ph}} \exp\left(-\frac{U^0}{k_B T + u_0 n_{2D}}\right).$$
(3.11)

The disorder potential amplitude and diffusion coefficient were adjusted to get the best possible fit for all different concentrations. The final fits are in the next section.

RESULTS AT $T_b = 1.5\,\mathrm{K}$

In this section experimental results and theoretical results are compared directly. Two-dimensional colour images of the PL intensity in the $x - y$ plane and in the $E - x$ plane were obtained from experimental and theoretical results; in both these diagrams the varying intensity of the PL signal is shown with different colours as in Fig. 3.7. These plots are shown in Fig. 3.12 for both experimental and calculated results, and the internal ring of PL is clearly seen.

The measured and calculated PL signal profile, $I_{PL} = I_{PL}(r_{\parallel})$, obtained in experiments and calculated for various pump powers P_{ex} is shown in Fig. 3.13. With increasing P_{ex} the internal PL ring appears in the I_{PL} profile. This is in complete agreement with the observations in this experiment and in the previous experiments (see Fig. 3.2).
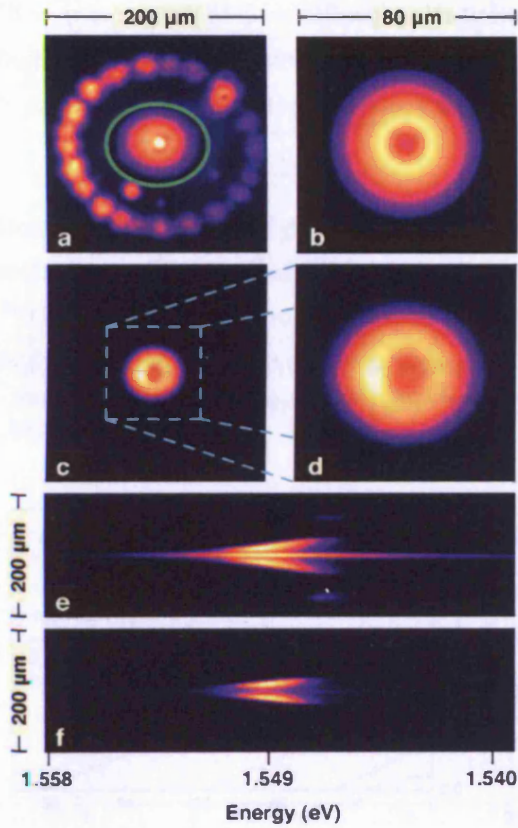
Figure 3.12: All plots show patterns of the PL signal in the $x - y$ plane, and are from experimental data except for (b), which is calculated. White represents the highest intensity, then yellow, red, purple and blue represent decreasing intensities and black represents no PL signal. The excitation powers, $P_{ex} = 250\,\mu W$ [(a) and (e)] and $75\,\mu W$ [(c), (d) and (f)], and (b) corresponds to a power of $75\,\mu W$ and $T_b = 1.5\,K$. In (a) the PL intensity in the area within the green circle is reduced by a constant factor for better visualization, and the bright spot in the middle of the internal ring is due to residual n^+ GaAs emission. The PL signal is imaged in $E - x$ coordinates in (e) and (f). For high P_{ex} the external PL ring is also seen in (a) and (e).
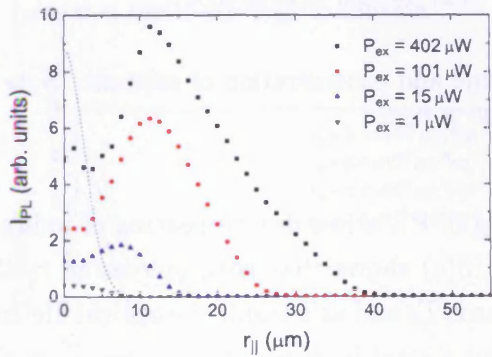
(a) Experimental results for various excitation powers as shown.
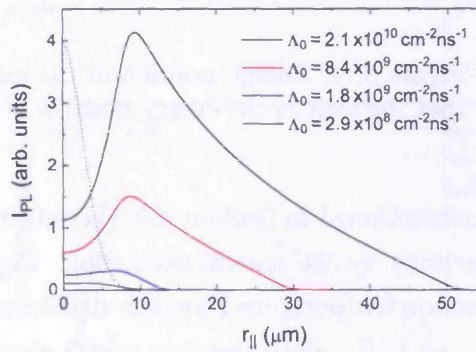
(b) Theoretical results for various exciton creation rates as shown.

Figure 3.13: The PL signal of indirect excitons plotted against radius. The Gaussian profile of the optical excitation is shown by the dotted black lines.

The parameters used in numerical simulations are: $D = 9.6\,\text{eV}$, $\tau_\text{R} = 13\,\text{ns}$, $T_\text{b} = 1.5\,\text{K}$, $T_\text{i} = E_\text{i}/k_\text{B} = 200\,\text{K}$, FWHM of the excitation profile $= 6.16\,\mu\text{m}$, and $\eta = 8°$. The fitting parameters were adjusted until the best fit to the data was obtained, and the final numbers are given by: $U^0 = 0.9\,\text{meV}$, $D_{\text{x}-\text{ph}} = 60\,\text{cm}^2/\text{s}$, and $C_{\text{x}-\text{x}} = 15\,\text{cm}^2/\text{s}$.

Figure 3.14 shows that the concentration profile $n_\text{2D} = n_\text{2D}(r_\parallel)$ always has a smooth shape, with n_2D^max occurring at $r_\parallel = 0$ and decreasing with increasing $r_\parallel$. The excitation powers $P_\text{ex} = 1$, 15, 101 and $402\,\mu\text{W}$ gave rise to concentrations $n_\text{2D}^\text{max} = 0.15 \times 10^{10}$, 0.44×10^{10}, 1.27×10^{10} and $2.50 \times 10^{10}\,\text{cm}^{-2}$ respectively, using generation rates $\Lambda_0 = 2.9 \times 10^8$, 1.8×10^9, 8.4×10^9 and $2.1 \times 10^{10}\,\text{cm}^{-2}\text{ns}^{-1}$ respectively.
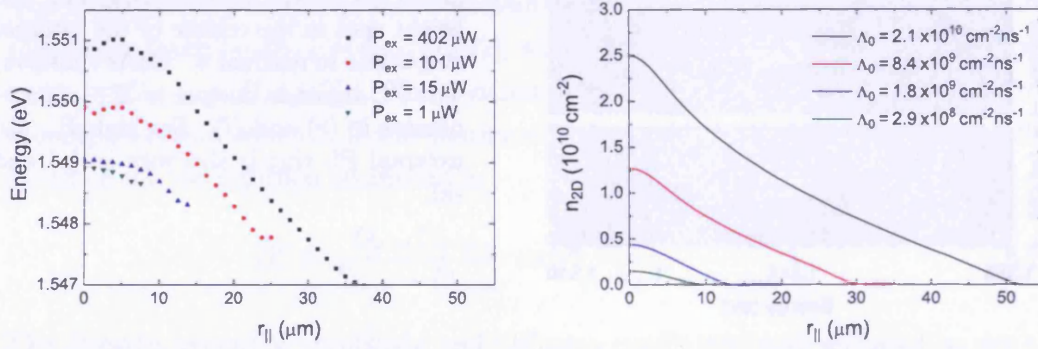
(a) Experimental results: the energy position of the exciton line plotted against radius, for various excitation powers as shown.

(b) Theoretical results: the calculated concentration plotted against radius, for various exciton creation rates as shown.

Figure 3.14: Energy position of the exciton line and concentration of excitons. Note that the shift in the energy position of the line $\propto n_\text{2D}$.

As mentioned in Section 3.5, the internal ring of PL arises due to heating of indirect excitons by the optical excitation. Figure 3.15(c) shows that with increasing $r_\parallel$ the exciton temperature T rapidly decreases towards T_b and as a result the optical lifetime $\tau_\text{opt} = 1/\Gamma_\text{opt}$ decreases too, which gives rise to a local increase of $I_\text{PL}(r_\parallel)$ at $r_\parallel = r_\parallel^\text{rg}$. The numerical simulations also reproduce the observed increase of $r_\parallel^\text{rg}$ and spatial extension of the PL area (HWHM of the signal) with increasing P_ex (see Fig. 3.15(a)).

As seen in Section 3.5, the amplitude of the disorder potential, U^0, determines the steepness of $I_\text{PL}(r_\parallel > r_\parallel^\text{rg})$ and therefore the dependence of the PL pinning radius. The ring contrast and ring radius dependencies are mainly determined by $D_{\text{x}-\text{ph}}$ and
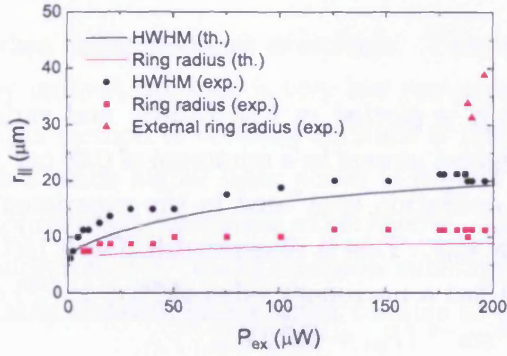
(a) The theoretical and experimental internal ring radius and the HWHM of the spatial extension of the PL signal are plotted against excitation power.
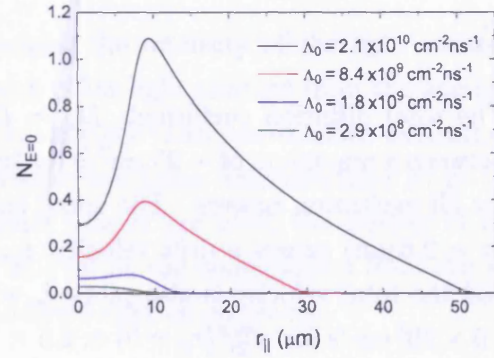
(b) A plot of the occupation number of the ground state against radius for excitation powers.
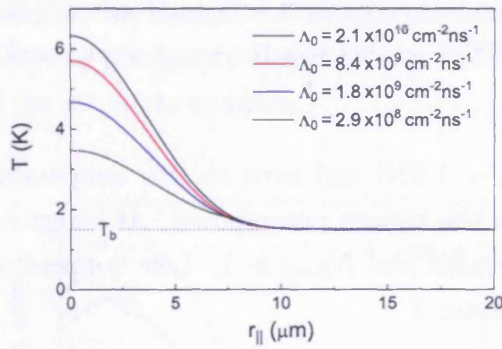
(c) The exciton temperature plotted against radius, for various excitation powers as in (b) (note that this x-axis scale is different).
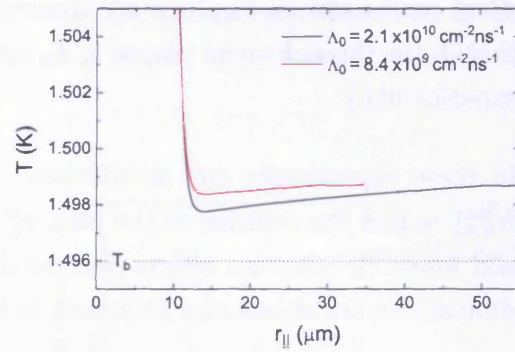
(d) The exciton temperature for the two highest excitation powers; note the different y-axis scale.
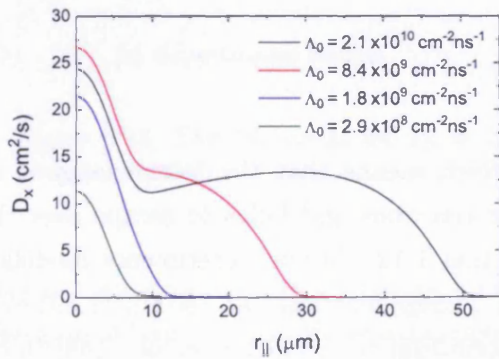
(e) The diffusion coefficient plotted against radius for the same excitation powers as in (b) and (c).
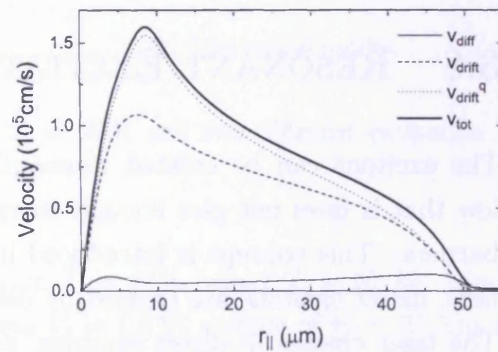
(f) Various velocities of the excitons as shown, plotted against radius for $\Lambda_0 = 2.1 \times 10^{10}$ cm^{-2}ns^{-1}.

Figure 3.15: Ring radii plotted against P_{ex}, and $N_{E=0}$, T, D_x and velocities plotted against radius (line colours in (b), (c) and (e) as in Figs. 3.13 and 3.14).

C_{x-x}.

The total diffusion coefficient, $D_x = \tilde{D}_x^d(r_\parallel)$, is plotted in Fig. 3.15(e), and varies between a maximum of $\sim 25\,\mathrm{cm^2/s}$ for the highest powers to a minimum of $0.06\,\mathrm{cm^2/s}$ for all excitation powers. The small sized excitation spot used in the experiments ($\sigma = 2.6\,\mu\mathrm{m}$) causes a drift velocity, $v_\mathrm{drift} \gg v_\mathrm{diff}$. This is illustrated in Fig. 3.15(f), and the total velocity is also plotted, which has a maximum value $v_\mathrm{tot}^\mathrm{max}(r_\parallel \simeq r_\parallel^\mathrm{rg}) \simeq 1.5 \times 10^5\,\mathrm{cm/s}$ for $n_\mathrm{2D}^\mathrm{max}(r_\parallel = 0) \simeq 2.5 \times 10^{10}\,\mathrm{cm^{-2}}$ ($P_\mathrm{ex} = 402\,\mu\mathrm{W}$).

As seen in Fig. 3.15(c), the excitons cool down rapidly outside the excitation spot. At $r \sim 10\,\mu\mathrm{m}$ their temperature reaches T_b, but due to the effect of recombination heating and cooling T then increases gradually such that it is higher than T_b by 3 mK, which means that in this case there is a net recombination heating of the system. This effect can be seen in Fig. 3.15(d). However, in this case it is a very small effect. (Note that T_b to three decimal places is $T_b = 1.496\,\mathrm{K}$ as this was the exact value used in experiments.)

In these experiments and simulations, $T_b = 1.5\,\mathrm{K}$, and even at this temperature $N_{E=0}^\mathrm{max} \sim 1$ at the position of the ring, $r_\parallel^\mathrm{rg}$ for the highest pump power. At higher n_2D and lower T_b quantum effects become dominant and $N_{E=0} \gg 1$. Low temperature simulations are shown and discussed in Chapter 4.

In the following section resonant excitation data are fitted. This is done in exactly the same way as described in this section, the main difference in the numerical calculations being the initial injected energy of the excitons, E_i.

3.8 RESONANT EXCITATION

The excitons can be created resonantly, which means that the laser energy is so low that is does not give enough energy for electrons and holes to escape over the barriers. This concept is introduced in Section 1.12. In the experiments modelled here, direct excitons are created by using a Ti:Sapphire laser at 780 nm (1.594 eV). The laser creates lh direct excitons, and according to Eccleston et al. [148] lh-hh exciton transfer occurs within 150 ps for $n_\mathrm{2D} = 1.5 \times 10^8\,\mathrm{cm^{-2}}$ and within $< 20\,\mathrm{ps}$ for $n_\mathrm{2D} = 1.5 \times 10^{10}\,\mathrm{cm^{-2}}$ which is more relevant to experiments discussed in this section.

From an experimental point of view it is more difficult to obtain good quality data

when using resonant excitation. This is because the intensity of the light emitted by indirect excitons is very low compared with other light emitted from the sample. This method of creating excitons is much less efficient than nonresonant excitation, so a much higher laser power is needed to create the same concentrations as in the nonresonant excitation experiments. As higher powers are used, the quality of the background n^+ GaAs emission subtraction falls off as the contribution from the n^+ GaAs emission grows larger relative to the indirect exciton emission.

RESULTS AT $T_b = 1.5\,\mathrm{K}$

All the experiments and theoretical calculations for this section were carried out as described in Section 3.7 except for changes to a few parameters, described in the following paragraph. Experimental data is fitted as before, after very careful removal of the n^+ GaAs emission.

(a) Experimental results.   (b) Theoretical results.
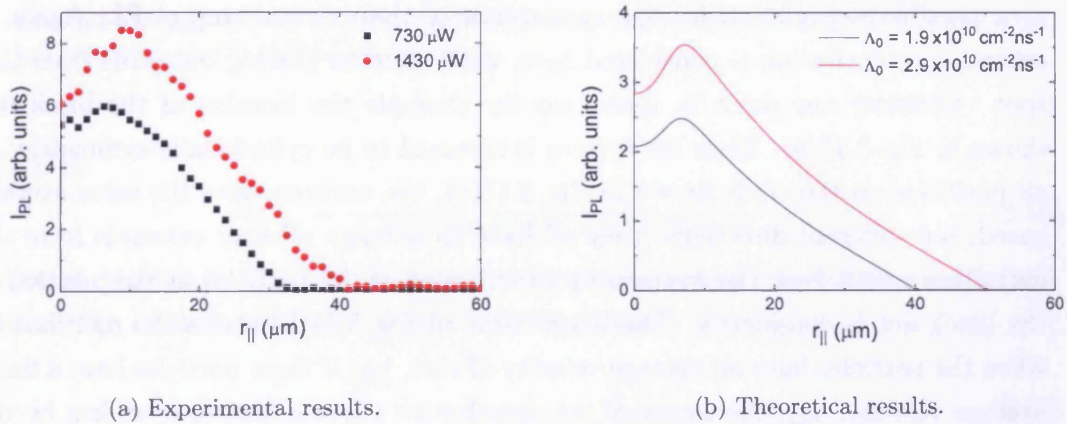
Figure 3.16: The PL signal for $T_b = 1.5\,\mathrm{K}$, $T_i = 20\,\mathrm{K}$ and two different excitation powers as shown.

In the theoretical results for resonant excitation $T_i = 20\,\mathrm{K}$, where $T_i = E_i/k_B$. Since the gate voltage used in these experiments was $V_g = 1.6\,\mathrm{V}$, a value of $\tau_R = 31.3\,\mathrm{ns}$ is used (see Fig. 1.12). All the other parameters, including U^0, C_{x-x} and D_{x-ph} are the same as in Section 3.7, and $T_b = 1.5\,\mathrm{K}$. The results for the PL signal, I_{PL} are shown in Fig. 3.16, for concentrations $n_{2D} = 2.50 \times 10^{10}$ ($\Lambda_0 = 2.90 \times 10^{10}\,\mathrm{cm}^{-2}\mathrm{ns}^{-1}$) and $1.87 \times 10^{10}\,\mathrm{cm}^{-2}$ ($\Lambda_0 = 1.9 \times 10^{10}\,\mathrm{cm}^{-2}\mathrm{ns}^{-1}$). Note, in particular, the high excitation

powers used in experiments (see Fig. 3.16(a)) compared with the lower powers used in the nonresonant case in Section 3.7.

Note that $T(r_\| = 0)$ is lower in this case than in the nonresonant case. Here, $T(r_\| = 0) = 2.8\,\mathrm{K}$ for $A_0 = 1.9 \times 10^{10}\,\mathrm{cm^{-2}ns^{-1}}$ and $T(r_\| = 0) = 2.9\,\mathrm{K}$ for $A_0 = 2.9 \times 10^{10}\,\mathrm{cm^{-2}ns^{-1}}$. The diffusion coefficient is a maximum at $r_\| = 0$: $D_\mathrm{x}^\mathrm{max} = 15.2\,\mathrm{cm^2/s}$ and $D_\mathrm{x}^\mathrm{max} = 16.7\,\mathrm{cm^2/s}$ for the low and high excitation powers respectively where $D_\mathrm{x} = \tilde{D}_\mathrm{x}^\mathrm{d}$.

3.9 SUPPRESSION OF THE OPTICAL DECAY OF EXCITONS DUE TO THEIR FINITE VELOCITY

When the excitons have a finite velocity, they are 'darker' than when they are stationary, *i.e.* their optical decay is suppressed. This is because less of the excitons are located inside the photon cone (see Fig. 1.10). This effect was discussed in Ref. [5] as a possible explanation for the appearance of the external ring of PL. Again, a central spot excitation is considered here, with excitons moving outwards from this spot. Consider one point in space, say for example the location of the black dot shown in Fig. 3.17(a). Since the system is assumed to be cylindrically-symmetric, at all positions on the circle drawn in Fig. 3.17(a), the excitons have the same average speed, but different directions (they all have an average velocity outwards from the excitation spot). Now the momentum distribution of the particles at the position of the black dot is considered. The black curve in Fig. 3.17(b) shows the distribution when the particles have an average velocity of zero, but if these particles have a finite average velocity, v_tot, the centre of the distribution curve is shifted as shown by the green curve, where the shift is given by $k_\mathrm{d} \propto v_\mathrm{tot}$.

This effect can be incorporated into the equation for the effective decay rate, $\tilde{\Gamma}_\mathrm{opt}$ in the following way:

$$\tilde{\Gamma}_\mathrm{opt} = \frac{1}{\tilde{\tau}_\mathrm{opt}} = \frac{\Gamma_0}{2} \frac{E_\gamma}{k_\mathrm{B}T_0} I_3 \,, \tag{3.12}$$

where I_3 in this case is more complicated than the integral in Eq. 1.12 because in this case the integration needs to be carried out over z and ϕ. The angle ϕ is between k and k_d, and k is the momentum of an exciton. The occupation number, N_{k-k_d} is
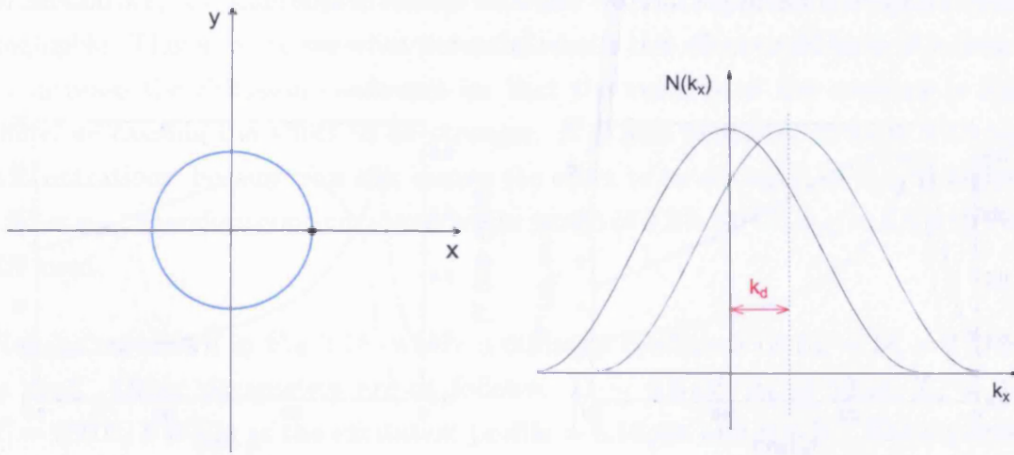
(a) The studied system is cylindrically-symmetric in the $x - y$ plane.

(b) Exciton distribution in momentum space.

Figure 3.17: At all positions on the circle in (a) the excitons have the same average speed. One point in space is studied, for example the location of the black dot shown. The momentum distribution of the particles at this point is plotted in (b): since they have an average velocity in the x-direction, their distribution in momentum space is not isotropic, and is shifted as shown.

given by

$$N_{k-k_{\mathrm{d}}} = \frac{1}{A e^{\hbar^2(|\boldsymbol{k}|^2+|\boldsymbol{k}_{\mathrm{d}}|^2-2|\boldsymbol{k}|\,|\boldsymbol{k}_{\mathrm{d}}|\cos\phi)/2M_{\mathrm{x}}k_{\mathrm{B}}T} - 1}, \tag{3.13}$$

where A is given by Eq. 1.11. If this equation is transferred into energy coordinates, it can then be included into I_3 in the following way:

$$I_3 = \frac{1}{2\pi\, n_{\mathrm{2D}}} \int_0^1 \mathrm{d}z \int_0^{2\pi} \mathrm{d}\phi \frac{1+z^2}{A e^{E_\gamma(1-z^2+y-2\sqrt{y(1-z^2)}\cos\phi)/k_{\mathrm{B}}T} - 1}, \tag{3.14}$$

where $y = E_{\mathrm{d}}/E_\gamma$.

Results at $T_{\mathrm{b}} = 1.5\,\mathrm{K}$

For simplicity, a constant diffusion is used, and the mean-field energy conversion effect is not included. The effect was incorporated into the code, and results were obtained for $n_{\mathrm{2D}}^{\max} = 0.44 \times 10^{10}$ and $2.5 \times 10^{10}\,\mathrm{cm}^{-2}$. When a diffusion coefficient of $D_{\mathrm{x}} = D_{\mathrm{x}}^{\mathrm{c}} = 25\,\mathrm{cm}^2/\mathrm{s}$ is used (an approximation consistent with values of D_{x} deduced

(a) $n_{2D}^{max} = 2.5 \times 10^{10}\,cm^{-2}$

(b) $n_{2D}^{max} = 4.0 \times 10^{10}\,cm^{-2}$
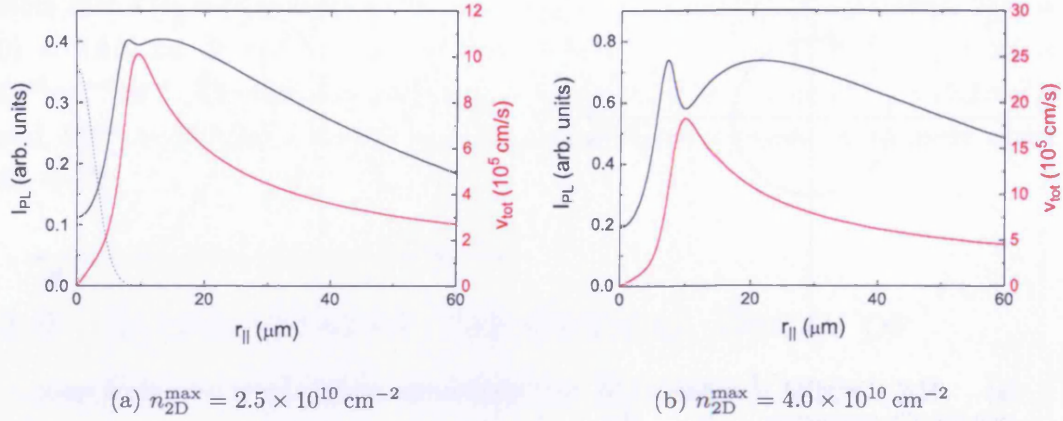
Figure 3.18: PL signal and total velocity plotted against radius for $D_x = D_x^c = 100\,cm^2/s$, $T_b = 1.5\,K$, $T_i = 200\,K$ and two different concentrations.
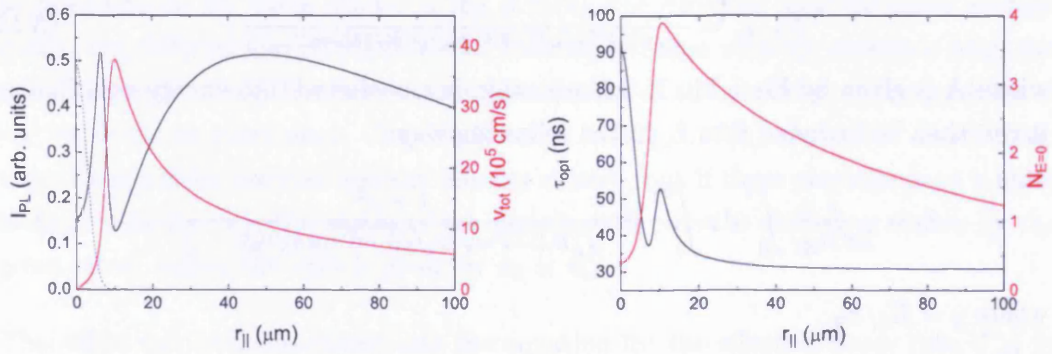
(a) PL signal and total velocity plotted against radius.

(b) Optical lifetime and occupation number of the ground state plotted against radius.

Figure 3.19: I_{PL}, v_{tot}, τ_{opt} and $N_{E=0}$ plotted against radius for $D_x = D_x^c = 250\,cm^2/s$, $T_b = 1.5\,K$, $n_{2D}^{max} = 4.0 \times 10^{10}\,cm^{-2}$ and $T_i = 200\,K$.

in Section 3.7) the difference in results with and without suppression of optical decay is negligible. Therefore, to see what potential results this effect could have, it is desirable to increase the diffusion coefficient so that the velocity of the excitons is higher, therefore causing the effect to be stronger. It is also beneficial to work with higher concentrations, because this also causes the effect to be stronger, as v_{drift} is higher for higher n_{2D}; therefore concentrations in the range of $2.5 \times 10^{10} < n_{\text{2D}} < 4.0 \times 10^{10}\,\text{cm}^{-2}$ are used.

Results are shown in Fig. 3.18, where a diffusion coefficient of $D_{\text{x}} = D_{\text{x}}^{\text{c}} = 100\,\text{cm}^2/\text{s}$ is used. Other parameters are as follows: $D = 9.6\,\text{eV}$, $\tau_{\text{R}} = 13\,\text{ns}$, $T_{\text{b}} = 1.5\,\text{K}$, $T_{\text{i}} = 200\,\text{K}$, FWHM of the excitation profile $= 6.16\,\mu\text{m}$ and $\eta = 8\,°$. The suppression of the optical decay of excitons starts to have an effect on the PL signal when $D_{\text{x}} = D_{\text{x}}^{\text{c}} = 100\,\text{cm}^2/\text{s}$ and $n_{\text{2D}}^{\text{max}} = 2.5 \times 10^{10}\,\text{cm}^{-2}$, as shown in Fig. 3.18(a), where a slight two-peaked shape appears in the PL profile. This effect might not be detected in experiments because it is rather small, so Fig. 3.18(b) shows the results for a higher concentration, $n_{\text{2D}}^{\text{max}} = 4.0 \times 10^{10}\,\text{cm}^{-2}$, where the effect is significantly stronger.
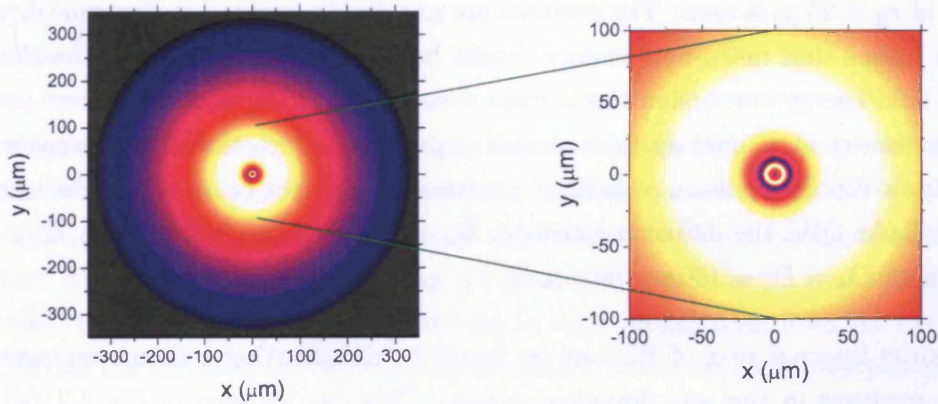
Figure 3.20: 2D images of the PL signal intensity in the $x - y$ plane, where white represents the highest intensity, then yellow, red, purple and blue represent decreasing intensities and black represents no PL signal.

Figure 3.19 shows results for a higher diffusion coefficient, and here it is clear that the internal ring of PL splits into two distinct rings, due to the effect of the suppression of optical decay of excitons. The maximum total velocity here is high, $v_{\text{tot}} \sim 1.7 \times 10^6\,\text{cm/s}$. In Fig. 3.19(b) the optical lifetime is plotted, which has a distinctly different, two-peaked, shape from the usual $\tau_{\text{opt}}(r_{\parallel})$ profile. When $D_{\text{x}} = D_{\text{x}}^{\text{c}} = 100\,\text{cm}^2/\text{s}$,

$\tau_{\mathrm{opt}}(r_{\parallel})$ does not have a two-peaked structure, and the shape, $\tau_{\mathrm{opt}} = \tau_{\mathrm{opt}}(r_{\parallel})$, is similar to the case when suppression of optical decay is not included. In this case, τ_{opt} is smaller by $\sim 2\,\mathrm{ns}$ at the position of maximum total velocity.

The concentration profiles, $n_{\mathrm{2D}}(r_{\parallel})$, for the cases when suppression of optical decay is included and excluded do not differ significantly. The PL signal in the $x - y$ plane is plotted in Fig. 3.20.

Since the suppression of optical decay does not have a significant effect on results when $D_{\mathrm{x}} \lesssim 100\,\mathrm{cm^2/s}$, and because it takes an extensive amount of time to obtain the numerical results, the effect is not included in further work in this thesis.

3.10 DIRECT EXCITONS

The equations used throughout this chapter to model indirect excitons in CQWs can be used to model direct excitons in single QWs. In this case $\tau_{\mathrm{opt}} > \tau_{\mathrm{th}} > \tau_{\mathrm{R}}$ and a value of $\tau_{\mathrm{R}} = 25\,\mathrm{ps}$ is used. The excitons are not dipole-oriented in the same direction which means that mean-field energy should be omitted, so $u_0 = 0$ and therefore the mean-field energy conversion mechanism does not exist, $S_{\mathrm{d}} = 0$. For direct excitons the exciton-exciton interaction is a spin-dependent interaction, much weaker than the dipole-dipole repulsion of indirect excitons. For direct excitons in a high-quality single GaAs QW, the diffusion constant, $D_{\mathrm{x}} \sim 10 - 100\,\mathrm{cm^2/s}$ [118, 120, 129]. Here, a value of $D_{\mathrm{x}} = D_{\mathrm{x}}^{\mathrm{c}} = 100\,\mathrm{cm^2/s}$ is used.

The same internal ring of PL can be found by substituting indirect excitons with direct excitons in the way described above. This can be seen in Fig. 3.21(a) for a maximum concentration of $n_{\mathrm{2D}} = 2.5 \times 10^{10}\,\mathrm{cm^{-2}}$. If the focus of the laser is not strong enough the ring is not present, but when the focus reduces to FWHM $\sim 2\,\mu\mathrm{m}$ the ring appears.

Due to the short intrinsic lifetime, the recombination heating and cooling effect is strong. This is illustrated in Fig. 3.21(b), where the temperature profile, $T(r_{\parallel})$, is plotted. The inset shows T for the outermost excitons for the two excitations with the smallest FWHM, and in both these cases the exciton temperature stabilises at $T \simeq 2.9\,\mathrm{K}$, which is significantly higher than $T_{\mathrm{b}} = 1.5\,\mathrm{K}$.
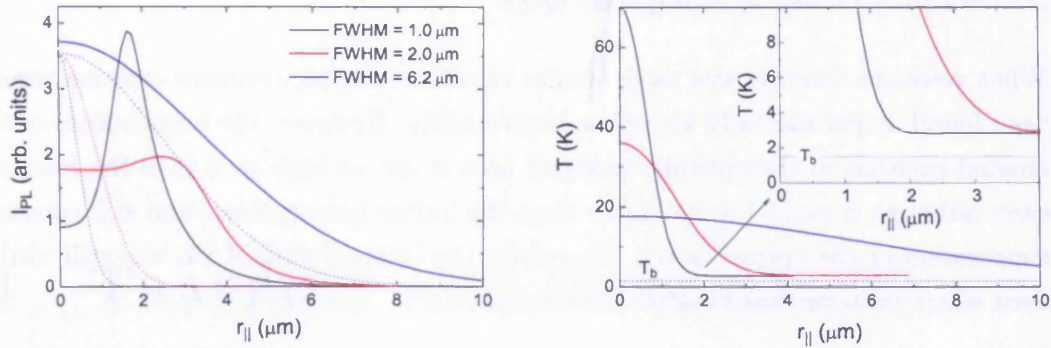
(a) The PL signal (solid lines) and excitation profiles (dotted lines) plotted against radius.

(b) The exciton temperature plotted against radius, for excitation profiles with FWHM = 1.0, 2.0 and 6.16 μm (black, red and blue lines respectively).

Figure 3.21: The PL signal and the exciton effective temperature for direct excitons in single QWs for three excitation profiles with various FWHM. Here, $T_b = 1.5\,\mathrm{K}$, $n_{2D}^{max} = 2.5 \times 10^{10}\,\mathrm{cm}^{-2}$, $D_x = D_x^c = 100\,\mathrm{cm}^2/\mathrm{s}$ and $\tau_R = 25\,\mathrm{ps}$.

3.11 Summary

Three equations for the diffusion, thermalization and optical decay of the indirect excitons were used to model the cylindrically-symmetric system of excitons in 2D. The equations include quantum-statistical corrections relevant to degenerate indirect excitons. The origin of the internal ring of PL found in experiments is unambiguously identified: it is due to cooling of the excitons in their propagation from the excitation spot. When the excitons are created nonresonantly, in the optically-pumped area the exciton temperature is high ($T \approx 5\,\mathrm{K}$); significantly higher than the lattice temperature T_b (which is $1 - 2\,\mathrm{K}$ in experiments discussed in this chapter). As a result, their optical decay is suppressed (since only low-energy excitons can optically decay), but as they travel out from the excitation spot they cool down and become more optically-active, giving rise to an increase in the PL signal: the 'internal ring' of PL. The PL signal then decays because all the particles eventually decay.

The same internal ring of PL can be found for direct excitons in single QWs, if their diffusion is large enough and the FWHM of the laser beam is small enough. In this case, the recombination heating and cooling effect is strong: a net heating effect is seen outside the laser spot due to the excitons' short radiative life. The internal PL

ring is therefore a generic feature of PL from excitons, direct or indirect, that are nonresonantly excited in high-quality QWs.

When resonant creation was used, similar results to the nonresonant creation results were found, experimentally as well as theoretically. However, the temperature of the created excitons in the optically-pumped area is not as high as it is in the resonant case, although it proved to be higher than the lattice temperature, and still caused a suppression of the optical decay. Therefore, the internal ring of PL was still visible even when excitons were created resonantly.

The screening of disorder by the dipole-oriented excitons was discussed and modelled for an arbitrary in-plane disorder potential and a Gaussian-shaped optical excitation. This disorder is assumed to be of long-range order (on the μm scale) and of amplitude, $U^0 \sim 1\,\text{meV}$. The screening effect is stronger when the concentration of excitons is higher ($\gtrsim 10^{10}\,\text{cm}^{-2}$), but weakens when the exciton temperature is higher ($\gtrsim 10\,\text{K}$).

The mean-field energy conversion mechanism was introduced and discussed, and included into the numerical simulations. This effect is strong when the average velocity of the excitons decreases but their average energy remains high. The effect was strongest when the deceleration of excitons was highest, *i.e.* when the concentration decreased to zero abruptly.

The suppression of optical decay of excitons due to their velocity was discussed and modelled, and was found to have an effect on the results when $D_x = D_x^c > 100\,\text{cm}^2/\text{s}$ and $n_{2D} > 2.5 \times 10^{10}\,\text{cm}^{-2}$. A constant diffusion coefficient was used for simplicity. This effect could be observed experimentally if the diffusion coefficient is $D_x > 100\,\text{cm}^2/\text{s}$ and the laser power is strong enough.

In the next chapter, the trapping and possible BEC of excitons is discussed.

4 TRAPPING AND POSSIBLE BOSE-EINSTEIN CONDENSATION OF QUANTUM WELL EXCITONS

As long as the average spacing between excitons is much larger than their Bohr radius, they behave as bosons. Since excitons have a high degeneracy temperature $(T_0 \propto 1/M_x)$ they exhibit quantum-mechanical effects more easily than heavier bosons such as atoms. The concept of Bose-Einstein condensation was introduced in Sections 1.7 and 1.8, and in this chapter the trapping of excitons is modelled, and the possible transition to a Bose-Einstein condensate is discussed.

4.1 LASER TRAPPING

The benefits of using lasers is that they can provide an extremely precise and non-invasive force while also providing fast and simple control of the trapping field. Laser traps are briefly introduced and discussed in Section 1.7: optical trapping by radiation pressure was proposed by Ashkin in 1970 [35], where micron-sized particles were trapped in a laser beam. This idea was extended in Ref. [149], where Ashkin described how it could be possible to slow down an atomic beam of sodium atoms using the radiation pressure of a laser beam, and after being slowed, these atoms could be captured in a trap consisting of focused laser beams. In this laser cooling technique, the atomic motion is damped until the temperature of the atoms reaches the µK range. Optical trapping and manipulation of small neutral particles has advanced

enormously since 1970. Laser cooling and trapping have been key factors in many momentous experiments in subfields of physics, chemistry and biology, where small particles play an important role [150–153]. A specific kind of laser trap is introduced and used in this chapter.
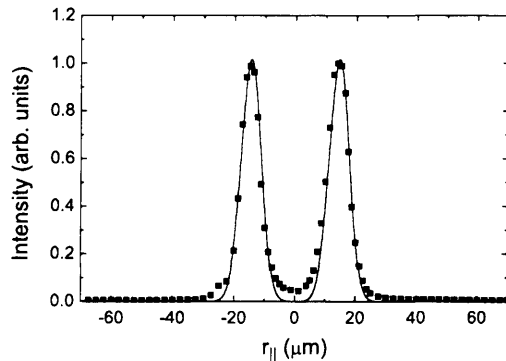
Figure 4.1: The laser intensity profile. The profile is cylindrically-symmetric and forms the basis of the trap for the excitons. It has a radius of $r_\parallel^{ex} = 14.5\,\mu m$. The points are experimental data and the line is the theoretical fit using two Gaussian profiles.

As in previous chapters, a laser creates the excitons. However in this case a ring-shaped laser spot is used, with an intensity profile as illustrated in Fig. 4.1. Because the excitons repel each other and the intensity profile is ring-shaped, the laser forms the basis of a potential trap with the energy minimum at the ring centre [154]. The trap is formed by the indirect excitons themselves: the trap potential is given by $U_{trap} = E_{shift} = u_0 n_{2D}$ and $E_{shift} \simeq 1.6\,meV$ for $n_{2D} = 10^{10}\,cm^{-2}$ as mentioned in Section 3.3. The trap confining mean-field potential is determined by the radial distribution of the excitons, $n_{2D}(r_\parallel)$, and does not depend on other characteristics such as their temperature T.

Optical traps can be controlled easily by varying the laser intensity in space or time. In addition to this, in the ring-shaped trap the excitons at the centre are cold since they are far enough away from the excitation ring: the effect of exciton heating due to the hot photogenerated excitons is small at distances $\gtrsim 10\,\mu m$ away from the excitation ring. The excitons' long lifetime and the strong dipole-dipole repulsion allow them to travel to the trap centre before they recombine, thus accumulating to create a cold and dense exciton gas. This will be demonstrated in further sections.

4.2   THEORETICAL AND EXPERIMENTAL RESULTS

The experiments are carried out in a similar way to the experiments mentioned in Section 3.7. The spatial $x - y$ PL pattern can be obtained, as well as the position of the exciton line. The theoretical results are also obtained similarly to the way described in Section 3.4. The diffusion coefficient and disorder potential can be fitted as before, although they should not differ much from previous results as the structures used are essentially the same.

Three different lasers were used: a Nd:YVO$_4$ laser at 532 nm, a HeNe laser at 633 nm and a Ti:Sapphire 788 nm laser tuned to the direct exciton energy. The spatial and spectral features were very similar for all the excitation wavelengths investigated, and the experimental data shown here were taken using the 532 nm excitation laser wavelength, with the gate voltage, $V_g = 1.4$ V which gives a ground state radiative lifetime of $\tau_R = 21$ ns. The power of the laser $10 < P_{ex} < 1020$ µW and all experiments were done at $T_b = 1.4$ K. The experimental results showing PL patterns in the $x - y$ and $E - x$ planes are shown in Fig. 4.2.
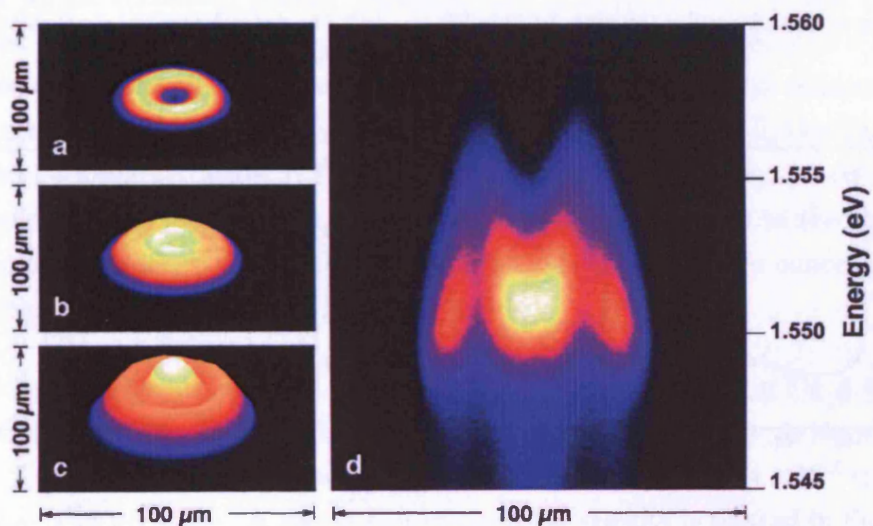
Figure 4.2: Experimental plots of the PL intensity from excitons created by a ring-shaped laser excitation, (a)-(c) in the $x - y$ plane and (d) in the $E - x$ plane. The lattice temperature $T_b = 1.4$ K and the excitation powers are as follows: $P_{ex} = 10, 35$ and 100 µW for (a), (b) and (c) respectively, and 75 µW for (d).
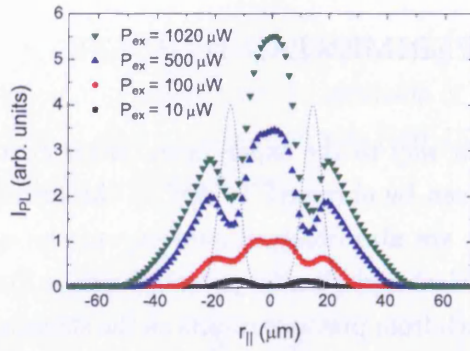
(a) Experimental results: PL signal.
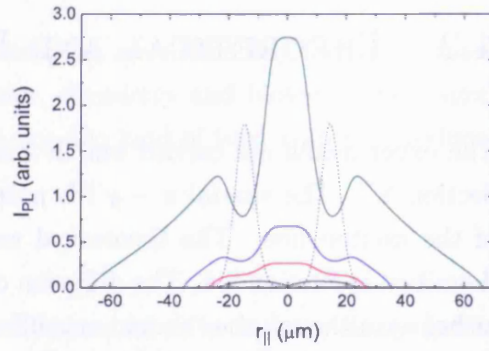
(b) Theoretical results: PL signal.
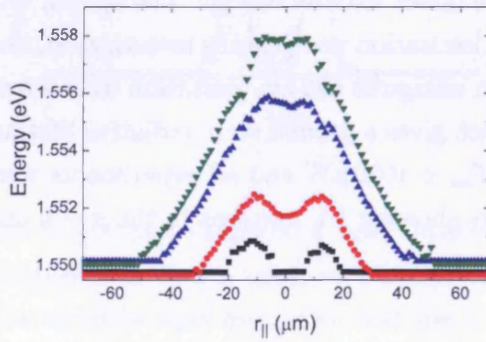
(c) Experimental results: energy of the PL line.
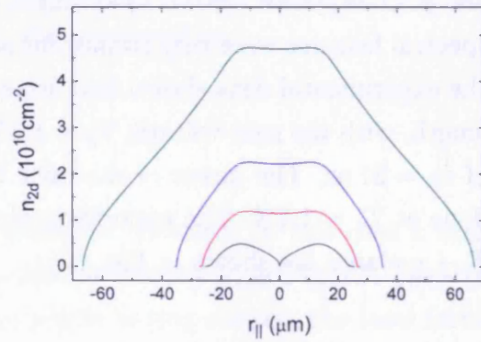
(d) Theoretical results: concentration profile, corresponding to (c).
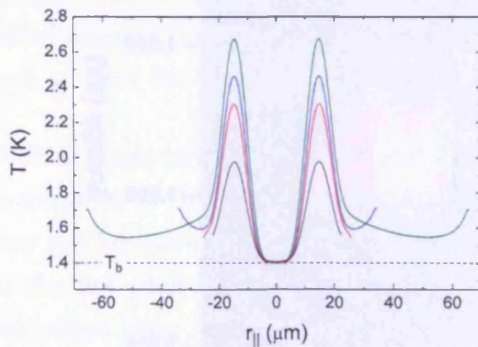
(e) Theoretical results: temperature of the excitons.
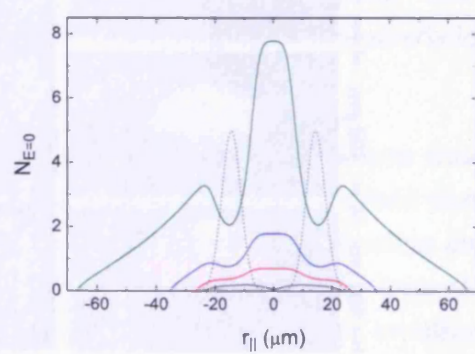
(f) Theoretical results: occupation number of the ground state.

Figure 4.3: Experimental and theoretical results for $T_b = 1.4\,\mathrm{K}$ and four different excitation powers, $P_{ex} = 1020, 500, 100$ and $10\,\mu\mathrm{W}$ corresponding to $\Lambda_0 = 6.4 \times 10^9$, 2.7×10^9, 1.2×10^9 and $2.8 \times 10^8\,\mathrm{cm}^{-2}\mathrm{ns}^{-1}$ respectively and shown by green, blue, red and black lines respectively. The excitation profile is shown by the dotted lines. Note that the scale of the $y-$axes of (c) and (d) correspond.

Equations 1.12, 2.72 and 3.1 are numerically solved in the same way as in Section 3.7, but here the optical excitation is positioned at $r_\parallel^{ex} = 14.5\,\mu m$, and the ring thickness has a Gaussian shape with $\sigma = 3.3\,\mu m$ (FWHM $= 2\sqrt{2\ln 2}\sigma = 7.7\,\mu m$). The equation for the creation rate of excitons is

$$\Lambda(r_\parallel) = \Lambda_0 e^{-(r_\parallel - r_\parallel^{ex})^2/2\sigma^2} , \tag{4.1}$$

and Eq. 3.11 is used for the diffusion coefficient. The theoretical results were fitted to experimental data as in the previous chapter, and for the excitation powers $P_{ex} = 10$, 100, 500 and 1020 μW the concentrations in each case are $n_{2D}(r_\parallel = 0) = 0.01 \times 10^{10}$, 1.2×10^{10}, 2.2×10^{10} and $4.7 \times 10^{10}\,cm^{-2}$ respectively. The generation rates of excitons in each case are $\Lambda_0 = 2.8 \times 10^8$, 1.2×10^9, 2.7×10^9 and $6.4 \times 10^9\,cm^{-2}ns^{-1}$ respectively. The value of T_i in the theoretical calculations affects the magnitude of the 'dip' in PL signal at $r_\parallel^{ex}$ (see Figs. 4.3(a) and (b)), and for these experimental data a value of $T_i = 100\,K$ is the most suitable. The values for the disorder and diffusion coefficients are $U^0 = 1.8\,meV$, $D_{x-ph} = 40\,cm^2/s$ and $C_{x-x} = 9\,cm^2/s$. See Fig. 4.3 for experimental and theoretical results.

As shown in Figs. 4.3(a) and (b), at low excitation powers, $P_{ex} \sim 10\,\mu W$ the PL profile is similar to the excitation profile. However, as P_{ex} is increased a strong PL signal is detected at the centre of the excitation ring, indicating the presence of a cold and dense gas of excitons. The theoretical results show that the exciton temperature at the trap centre is indeed extremely close to the lattice temperature T_b (see Fig. 4.3(e)) and in fact goes slightly below T_b by $\sim 1\,mK$ for the highest excitation power. A small heating effect is also seen outside the excitation ring, which is due to the mean-field energy conversion effect. The effect is strongest when the drop in concentration is sharp, which can be seen from Figs. 4.3(d) and (e).

The velocity of the excitons for $\Lambda_0 = 0.27 \times 10^{10}\,cm^{-2}ns^{-1}$ is plotted in Fig. 4.4(a). It is clear that the drift velocity is much higher than the diffusion velocity, as shown in Section 3.7. The maximum velocity when the highest power, $\Lambda_0 = 0.64 \times 10^{10}\,cm^{-2}ns^{-1}$, is used is $\sim 0.9 \times 10^5\,cm/s$. A vector plot of the total velocity is plotted in Fig. 4.4(b), which clearly shows the points at which $v_{tot} = 0$: (1) at the centre, $r_\parallel = 0$ and (2) at the position of the solid red ring, which lies inside the laser excitation ring. The latter position corresponds to the point at which $n_{2D} = n_{2D}^{max}$.

The ring-shaped laser induces a ring-shaped trap with a radius slightly different to the radius of the laser ring; this is illustrated in Fig. 4.5 for the highest excitation power,
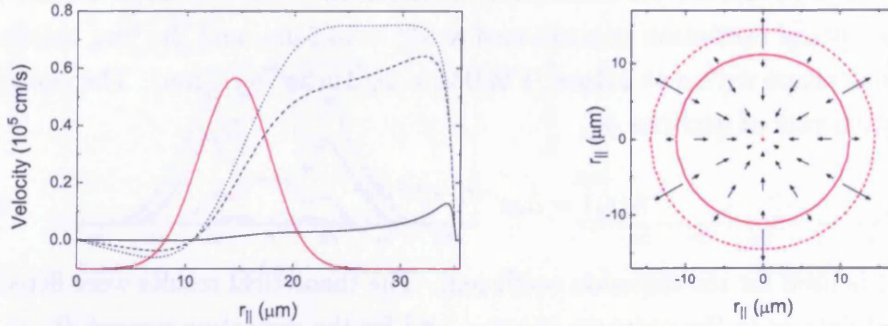
(a) Velocities plotted against radius: v_{diff}, v_{drift} and $v_{\mathrm{drift}}^{\mathrm{q}}$ shown by the solid, dashed and dotted lines respectively. The excitation profile is shown by the red line.

(b) A vector plot in the $x - y$ plane for the total velocity of excitons, v_{tot}. The solid red line and red dot show positions at which $v_{\mathrm{tot}} = 0$, and the dashed red line shows the laser ring radius, $r_{\|}^{\mathrm{ex}}$.

Figure 4.4: Velocity plots for $T_{\mathrm{b}} = 1.4\,\mathrm{K}$ and $\Lambda_0 = 0.27 \times 10^{10}\,\mathrm{cm}^{-2}\mathrm{ns}^{-1}$ ($n_{\mathrm{2D}}(r_{\|} = 0) = 2.2 \times 10^{10}\,\mathrm{cm}^{-2}$).

$\Lambda_0 = 0.64 \times 10^{10}\,\mathrm{cm}^{-2}\mathrm{ns}^{-1}$. The trap boundary, $r_{\|}^{\mathrm{tr}}$, is defined as the location where $n_{\mathrm{2D}} = n_{\mathrm{2D}}^{\mathrm{max}}$ because the trap is created by the exciton concentration distribution, $n_{\mathrm{2D}}(r_{\|})$. The trap radius $r_{\|}^{\mathrm{tr}} \simeq 11\,\mu\mathrm{m}$ and the laser ring radius $r_{\|}^{\mathrm{ex}} = 14.5\,\mu\mathrm{m}$, therefore $r_{\|}^{\mathrm{tr}} < r_{\|}^{\mathrm{ex}}$.

In these experiments, the occupation number of the ground state is as high as $N_{E=0} \simeq 8$ at the trap centre, see Fig. 4.3(f). The simulations show that if the lattice temperature is lowered, $N_{E=0}$ should increase dramatically, and at low temperatures the majority of the excitons should occupy the ground state; this is illustrated in the
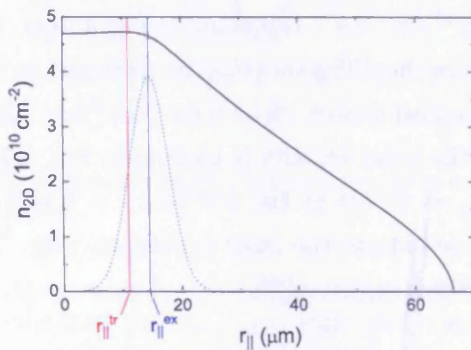
Figure 4.5: The radius of the trap, $r_{\|}^{\mathrm{tr}}$, compared with the radius of the laser ring, $r_{\|}^{\mathrm{ex}}$. The solid curve shows the concentration profile for the highest excitation power, $\Lambda_0 = 0.64 \times 10^{10}\,\mathrm{cm}^{-2}\mathrm{ns}^{-1}$ and the dotted line shows the excitation laser intensity profile.

next section.

Note that the excitation profile in the experiment is not exactly the same as the theoretical excitation profile. In experiments, the intensity ar $r_\parallel = 0$ is not $= 0$, although it is extremely low, less than 5 % of the maximum intensity. It is possible that this could have a small effect on the temperature of the excitons at the centre of the trap: they could be slightly hotter than predicted values in the theoretical results. However, it is stated in Section 2.8 that a stronger cooling effect is predicted at lower T_b due to the recombination heating and cooling effect, and therefore, the exciton temperature would be below T_b. This means that at lower T_b ($T_b \lesssim 1$ K), despite the fact that the intensity ar $r_\parallel = 0$ is not $= 0$ in experiments, the exciton temperature would still be close to T_b.

4.3 DERIVATION OF THE EQUATION FOR T_c

The definition of T_c can be stated as follows: at temperatures below T_c, a large, non-negligible, fraction of particles occupy the $E = 0$ state.

For BEC of noninteracting particles in a *homogeneous trap* of area S, the fugacity, $z = e^{\mu/k_B T}$ is given by

$$\frac{N}{g} = \sum_{j=1}^{\infty} z^j \left(1 + 2 \sum_{i=1}^{\infty} e^{-ji^2 \xi_0} \right), \tag{4.2}$$

where

$$\xi_0 = \frac{2\pi^2 \hbar^2}{M_x k_B T S} = \frac{\pi g}{N} \frac{T_0}{T} \tag{4.3}$$

and N is the number of particles in the trap. If $n_{2D} = $ constant in the trap, N is given by $N = n_{2D} S$. The occupation number of the ground state mode in the trap is given by

$$N_{E=0} = \frac{z}{1 - z}. \tag{4.4}$$

So far, these equations are exact, and μ is always < 0. If the temperature is lowered, keeping the concentration constant, the chemical potential will increase, approaching zero. In the thermodynamic limit it will not become equal to zero, which means that there is no BEC in the thermodynamic limit for $T > 0$. However, if a quasi-thermodynamic approach is used, where the ground state is separated from the other states, it is possible to put $\mu = 0$ and obtain an equation for T_c which signifies the temperature at which there is a large fraction of particles in the ground state.

The total number of particles, N is given by the sum of all the particles in the separate energy states:

$$N = g \sum_{E_k=0}^{\infty} \frac{1}{Ae^{E_k/k_{\mathrm{B}}T} - 1} \tag{4.5}$$

where $A = e^{-\mu/k_{\mathrm{B}}T}$. This summation can be changed to an integral if the separation between energy states is very small. If there is a large number of particles in the system, and their temperature, T, is high, only a negligible fraction of them are in the $E_k = 0$ state and the number of particles in this state can be neglected in the sum in Eq. 4.5. As the temperature is lowered, the fraction of particles in this state becomes non-negligible, and the temperature at which this happens is T_c. Therefore, T_c is the lowest temperature at which N can be calculated as follows:

$$N = g \sum_{E_{k_1}}^{\infty} \frac{1}{Ae^{E_k/k_{\mathrm{B}}T} - 1} \tag{4.6}$$

where E_{k_1} is the energy of the first state above ground state. Then, the sum is changed to an integral

$$N = \frac{gS}{4\pi^2} \int_{k_1}^{\infty} \frac{2\pi k \; \mathrm{d}k}{Ae^{\hbar^2 k^2/2M_x k_{\mathrm{B}}T} - 1} \tag{4.7}$$

where $k_1 = 2\pi/\sqrt{S}$ corresponds to the energy E_{k_1}. Since $n_{2\mathrm{D}} = N/S$, where S is the area of the trap,

$$n_{2\mathrm{D}} = \frac{gM_x k_{\mathrm{B}}T}{2\pi\hbar^2} \int_{\xi}^{\infty} \frac{\mathrm{d}x}{Ae^x - 1} \tag{4.8}$$

where ξ_0 is given by Eq. 4.3. Integrating Eq. 4.8 and substituting T_0 using Eq. 1.2 gives

$$\begin{aligned}
\frac{T_0}{T} &= \ln A + \xi_0 - \ln(Ae^{\xi_0} - 1) \\
&= -\ln(\frac{A - e^{-\xi_0}}{A}). \tag{4.9}
\end{aligned}$$

Then, A is substituted in and the chemical potential, μ. is set to be equal to zero, so

$$\frac{\pi g T_0}{N} = -T_c \ln(1 - e^{-T_0/T_c}) \tag{4.10}$$

which is the equation for T_c for a homogeneous trap.

4.4 CALCULATING $T_{\rm c}$ AND $N_{E=0}$ FOR A HOMOGENEOUS TRAP

In this section, the possibility of BEC of the excitons in the 2D trap introduced in Section 4.1 is discussed.

When a large number of indirect excitons are confined in the optically-induced trap, the concentration, and hence the mean-field potential, is nearly constant for $r_\parallel < r_\parallel^{\rm tr}$. Since $n_{\rm 2D}(r_\parallel < r_\parallel^{\rm tr}) \simeq$ constant, the total number of excitons in the trap is given by $N = n_{\rm 2D}S$, where $S = \pi(r_\parallel^{\rm tr})^2$. In these calculations $r_\parallel^{\rm tr} = 11\,\mu{\rm m}$, corresponding to the results in Section 4.2.

Equation 4.2 is used to calculate the fugacity, z, which can then be used to calculate $N_{E=0}$ which is given by Eq. 4.4. Equation 4.10 is then used to calculate $T_{\rm c}$. The number of excitons in the ground state is plotted against temperature in Fig. 4.6(a) for three different concentrations, assuming that the excitons' temperature in the trap is $T = T_{\rm b}$ (which is a fair assumption, as seen in Fig. 4.3(e)). This figure proves the validity of the equation derived for $T_{\rm c}$: the deviations between the 'quasi-thermodynamic' approach and the thermodynamic approach start to become significant at temperatures $< T_{\rm c}$.

Figure 4.6(b) shows the fraction of trapped excitons in the ground state for various concentrations.

- For $n_{\rm 2D} = 1.5 \times 10^{10}\,{\rm cm}^{-2}$, $N = 55400$ and hence $T_{\rm c} = 150\,{\rm mK}$.

- For $n_{\rm 2D} = 1.5 \times 10^{9}\,{\rm cm}^{-2}$, $N = 5500$ and hence $T_{\rm c} = 21\,{\rm mK}$.

- For $n_{\rm 2D} = 1.5 \times 10^{8}\,{\rm cm}^{-2}$, $N = 550$ and hence $T_{\rm c} = 3.5\,{\rm mK}$.

- For $n_{\rm 2D} = 1.5 \times 10^{7}\,{\rm cm}^{-2}$, $N = 55$ and hence $T_{\rm c} = 0.7\,{\rm mK}$.

The transition to a macroscopic occupation of the ground state, near $T_{\rm c}$, becomes sharper for higher concentrations. The maximum fraction is $N_{E=0}/N = 0.25$, this is because $N_{E=0}$ is for one spin degeneracy g, and N takes all spin degeneracies into account. Since $g = 4$, the maximum this fraction can be is 0.25, when all the excitons are in the ground state.
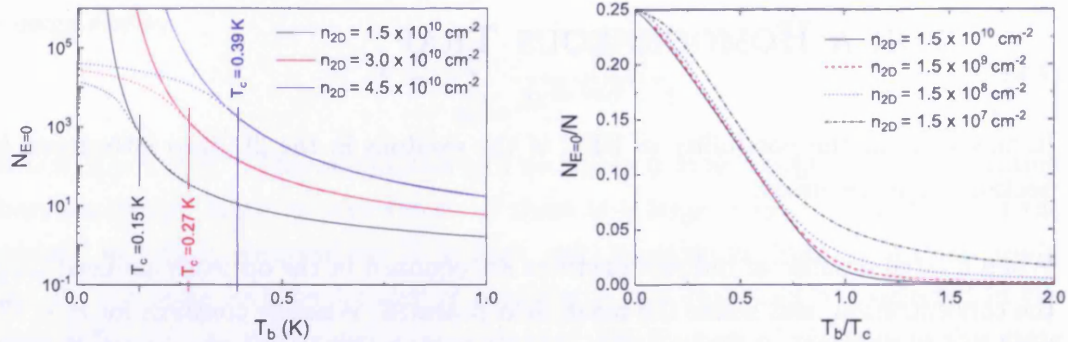
(a) $N_{E=0}$ plotted against T_b for excitons in an induced trap (dotted lines) and in the thermodynamic limit (solid lines) for various concentrations as shown.

(b) The fraction of trapped excitons in the ground state, $N_{E=0}/N$ against T_b/T_c for various concentrations as shown.

Figure 4.6: The occupation number of the ground state for various lattice temperatures and concentrations, (a) in the thermodynamic limit and for a homogeneous trap, and (b) for a homogeneous trap.

4.5   COMPARISON WITH SIMILAR RESULTS FOR 3D AND 1D STRUCTURES

Bose-Einstein condensation of an ideal gas was investigated theoretically by Ketterle and van Druten, for a finite number of particles in one and three dimensions [7]. For the 3D case, they studied particles in a *harmonic potential*, and found that BEC in systems with a small number of particles is very similar to systems with an infinite number of particles. This is illustrated in Fig. 4.7, where it is seen that the major difference for $N < \infty$ is the slightly shifted and smeared out onset of the macroscopic occupation of the ground state. As mentioned in Section 1.7, Ketterle and van Druten take the macroscopic occupation of the ground state as the defining characteristic of Bose-Einstein condensation. Grossmann and Holthaus also made calculations for a finite number of particles in a 3D harmonic potential, and obtained very similar results; in particular, they state that the onset of condensation does not occur at a sharply defined temperature as it would in the limit $N \to \infty$, but is smeared out over a temperature interval of order $N^{-1/3}$ [155]. The condensation temperature is also shifted to lower temperatures, *e.g.* for $N = 2000$ particles it shifts by $\sim 6\%$.

In 1963, Mills theoretically investigated the ground state occupancy of an ideal Bose

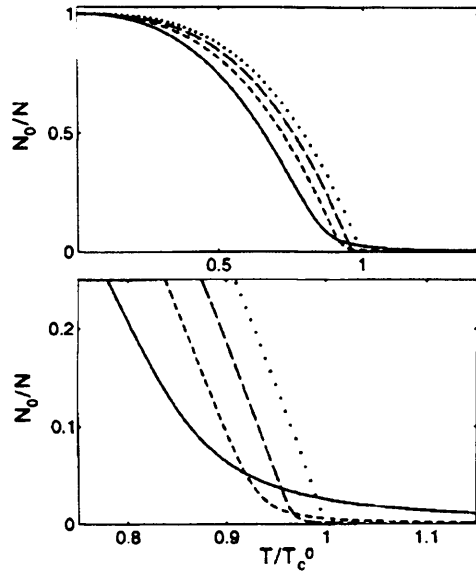Figure 4.7: The condensate fraction for a finite number of atoms in a 3D harmonic potential, plotted against temperature. The total number of atoms varies: $N = 100$, 1000, 10^4 and ∞ shown by solid, dashed, long dashed and dotted lines respectively. Taken from Ref. [7].
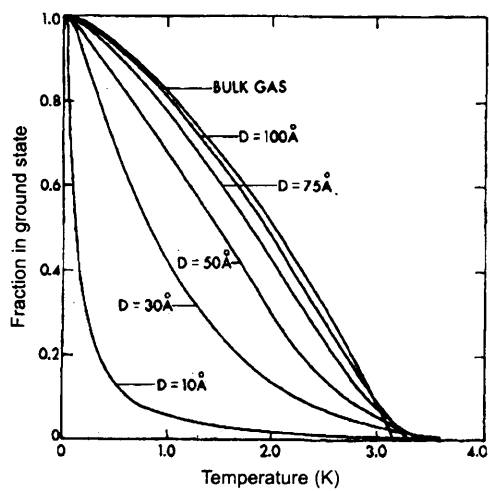
Figure 4.8: The occupation number of the ground state as a function of temperature for $x_L = 100\,\text{nm}$, taken from Ref. [8].

gas confined to a finite volume: a box of length x_L and sides x_D, where $20 < x_L < 500$ nm and $1 < x_D < 10$ nm [8]. The system is therefore quasi 1D, and Mills shows that an increasing deviation from the results for a bulk gas occurs when $x_L \gg x_D$. A plot of the occupation number of the ground state is shown in Fig. 4.8.

4.6 LOW TEMPERATURE SIMULATIONS

The experiments discussed in Section 4.2 have not been carried out for lattice temperatures lower than $T_b = 1.4$ K yet. However, theoretical results can be obtained without much difficulty for $T_b > 0.4$ K. In this section, theoretical results for $T_b = 0.4$ K are presented, and all other parameters, except for D_{x-ph}, are the same as in Section 4.2.

Since T_b is lower, the diffusion coefficient that originates from exciton-phonon scattering, D_{x-ph}, should change: it should increase, because there is a lower LA-phonon population at lower T_b. The exciton-phonon diffusion coefficient's dependence on temperature is unknown for CQWs. However, it is well-known that in bulk material, the exciton mobility's dependence on exciton-phonon scattering is $\propto T_b^{-3/2}$ [108, 110]. Since the mobility is given by $\mu_x = D_x/k_B T$, this gives a $T^{-1/2}$ dependence for the diffusion coefficient. Therefore, an estimate can be made for D_{x-ph} using the known results for bulk. A value of $D_{x-ph} = 40$ cm^2/s was deduced in Section 4.2 for $T_b = 1.5$ K, and therefore, for $T_b = 0.4$ K a value of $D_x = 77$ cm^2/s is used.

Figure 4.9 shows the concentration profile, exciton temperature, PL signal and occupation number of the ground state plotted against radius. Here, $D = 9.6$ eV, $\tau_R = 21$ ns, $n_{2D}(r_\parallel = 0) = 3.65 \times 10^{10}$ cm^{-2}, $A_0 = 0.56 \times 10^{10}$ cm^{-2}ns^{-1} and as in Section 4.2, $T_i = 100$ K, $U^0 = 1.8$ meV and $C_{x-x} = 9$ cm^2/s. The exciton temperature at the centre of the trap is $T = 0.38$ K; this is illustrated in Fig. 4.9(b). As seen in Fig. 4.9(d), the occupation number of the ground state in this case is nearly 500, which is ~ 0.35 % of the total number of excitons in the trap.

Finally, Fig. 4.10 shows how these results would look in an experiment, where the PL signal from the $x - y$ plane is visualized: the central PL peak would be the dominant feature, and the surrounding ring would have a very low contrast and might even be missed.
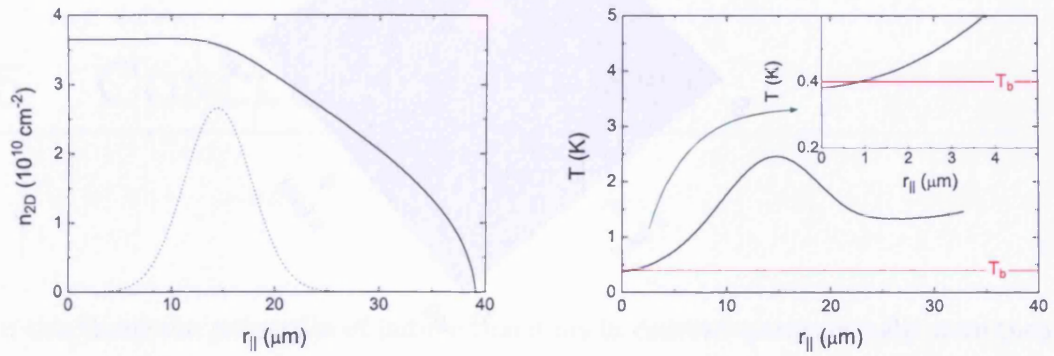
(a) The concentration plotted against radius. The excitation profile is also shown with a dotted line.

(b) The exciton temperature plotted against radius.
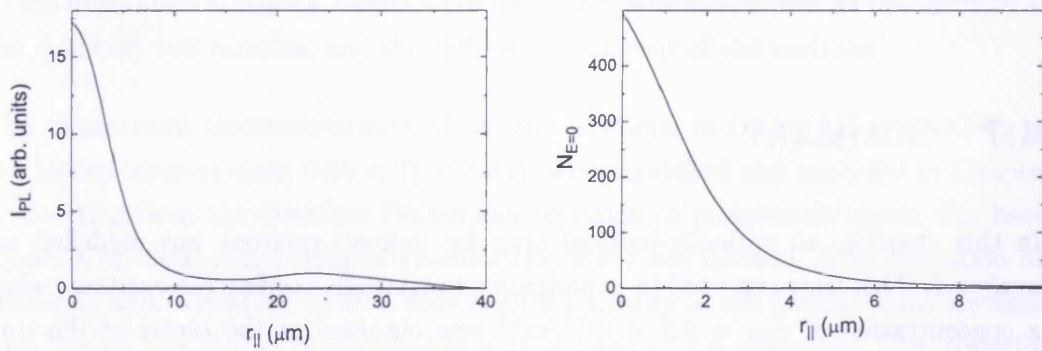
(c) PL signal plotted against radius.

(d) Occupation number of the ground state plotted against radius. Note the different x-axis scale.

Figure 4.9: n_{2D}, T, I_{PL} and $N_{E=0}$ plotted against radius for $T_b = 0.4$ K, $T_i = 100$ K and $\Lambda_0 = 0.56 \times 10^{10}$ cm^{-2}ns-1.
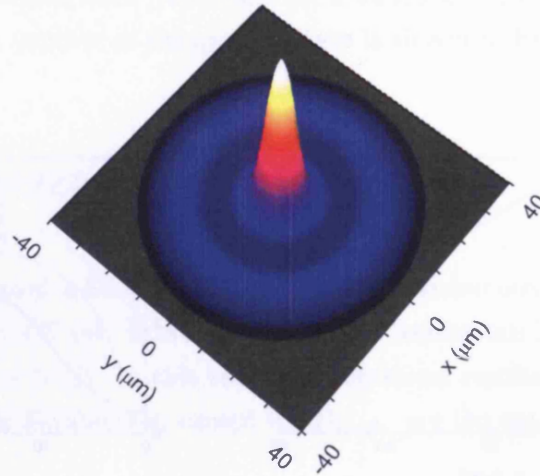
Figure 4.10: The PL signal intensity in the $x - y$ plane for $T_b = 0.4\,\mathrm{K}$, as in Fig. 4.9(c). The height represents the intensity of the PL signal, and the colours vary from white (maximum PL signal) to black (no PL signal).

4.7 SUMMARY

In this chapter, an optically-induced trap for indirect excitons was modelled and analysed. This trap was used in experiments to spatially confine the excitons, where a concentration of $n_{2D} = 4.7 \times 10^{10}\,\mathrm{cm}^{-2}$ was obtained at the centre of the trap. These experiments were modelled theoretically, and results were calculated numerically, giving a maximum occupation number of the ground state of $N_{E=0} \sim 8$.

Even though a Bose-Einstein condensate cannot exist in finite 2D systems, a kind of a Bose-Einstein condensate can exist, where a considerable fraction of particles are in the ground state. An equation for T_c was derived for a homogeneous trap in 2D, and simulations for lower lattice temperatures (Figs. 4.6(a) and (b)) show that $N_{E=0}$ increases dramatically, and that nearly all of the excitons in the trap would occupy the ground state if T_b is sufficiently small ($T_b \lesssim 0.1\,\mathrm{K}$).

5 CONCLUSIONS

In this thesis the properties of indirect excitons in coupled quantum wells were theoretically investigated. These properties included their temperature, their distribution in space, their optical lifetime and velocity. Their behaviour under various conditions was analysed theoretically. The theoretical results presented in this thesis were compared with experimental results where possible, and by fitting the theoretical results to the experimental results, values were found for parameters such as the disorder in the quantum well samples, and the diffusion coefficient of the excitons.

The relaxational thermodynamics of indirect excitons in GaAs/AlGaAs CQWs at low lattice temperatures, $0.05 < T_b < 1.8\,\mathrm{K}$, were modelled and analysed in Chapter 2. Starting from the quantum Boltzmann equation in momentum space, the basic equation of relaxational thermodynamics (Eq. 2.51) was derived. The derivation includes an approximation, so that only excitons already in the ground state are dealt with, which can couple in anti-Stokes with a band of LA phonons. This equation was used to model the temperature, $T(t)$, of a constant concentration of excitons, n_{2D}. An equation for the characteristic thermalization time (Eq. 2.54) was derived from Eq. 2.51, which holds when the exciton temperature, T, is close to the lattice temperature, T_b. A more complete microscopic equation (Eq. 2.64), which includes less approximations, was then derived from the quantum Boltzmann equation in energy space. This equation was modelled numerically, but proved to be very difficult to work with as it included three-fold integration over very irregular and spiky functions, which became more irregular at lower temperatures. The temperature variation with time, $T(t)$, was calculated with both Eq. 2.51 and Eq. 2.64, and the results were compared for a range of lattice temperatures. Results for $T_b = 0.35$ and $1.8\,\mathrm{K}$ were shown

103

in Figs. 2.7 and 2.8. The microscopic equation was not used in further simulations because of its complexity; instead, a *modified* version of Eq. 2.51 was used, with E_0 changed to E_0^*, where E_0^* was chosen to be a fit parameter. The value for E_0^* was found by fitting the results obtained with Eq. 2.51 with $E_0 \rightarrow E_0^*$ to the results of Eq. 2.64. This substituted value for E_0^* was used in all further calculations, and was deduced to be $E_0^* = E_0/2$.

The creation and decay of excitons were taken into account, so that their concentration varied with time, $n_{2D}(t)$. In addition to this, both the heating due to the laser and the recombination heating and cooling effect were modelled theoretically and included into the modified basic equation of relaxation thermodynamics, giving Eq. 2.72. The recombination heating and cooling effect proved to be very interesting. When $T_b > 2\,\mathrm{K}$ the effect is rather weak, but at lower temperatures it becomes an increasingly stronger effect. At very low lattice temperatures, $T_b \sim 50\,\mathrm{mK}$, only a cooling effect was observed, but at intermediate temperatures, $T_b \sim 1\,\mathrm{K}$, both heating and cooling effects were observed: after the switch off of the pump an initial cooling effect, but at longer time delays a heating effect.

In Chapter 3, the relaxational thermodynamics and optical creation and decay equations were combined with a diffusion equation for excitons, and a 2D system of excitons was modelled theoretically. The system was assumed to be cylindrically-symmetric and was modelled in the radial direction, with a laser pump situated at $r_{\parallel} = 0$. The excitons created by the laser then travelled outwards due to drift and diffusion, becoming more optically-active as their temperature lowered. The origin of the internal ring of PL was found to be due to the cooling of excitons travelling outwards from the excitation spot, and is a classical phenomenon. Results in this chapter were obtained for a lattice temperature, $T_b \simeq 1.5\,\mathrm{K}$.

The disorder in QW samples was taken into account by using a thermionic model for the diffusion coefficient (Eq. 3.6). The mean-field energy conversion effect was introduced and modelled. Theoretical results were compared with experimental results from experiments conducted by Butov *et al.* specifically for the purpose of modelling the internal ring of PL. By fitting the theoretical results to the experimental results taken at $T_b = 1.5\,\mathrm{K}$, values for the disorder in the structure and the diffusion coefficient of excitons were obtained. The disorder was found to have an amplitude of $U^0 = 0.9\,\mathrm{meV}$. The theoretical results did not fit the experimental results when using a constant diffusion coefficient, D_x^c, and even when the thermionic model was

incorporated into the diffusion coefficient, giving D_x^d, it was still difficult to obtain a good fit. An improved diffusion coefficient was used, $\tilde{D}_x^d$, where the exciton-exciton scattering and the exciton-phonon scattering were taken into account. The diffusion coefficient was found to vary between 0.06 and $\sim 25\,\mathrm{cm^2/s}$.

The suppression of optical decay of excitons due to their velocity was discussed and modelled theoretically. For diffusion coefficients, $D_x^c < 100\,\mathrm{cm^2/s}$ and concentrations, $n_{2D} \lesssim 2.5 \times 10^{10}\,\mathrm{cm^{-2}}$ the effects of suppression of optical decay of excitons was negligible. However, by increasing n_{2D} the effect became noticeable, and the PL profile, I_{PL}, formed a distinctly different, two peaked structure. This means that the internal ring of PL in the $x - y$ plane splits into two distinct rings. When D_x^c was increased further, the exciton optical lifetime profile, $\tau_{opt}(r_{\parallel})$, developed a different structure: a prominent minimum occurred at the position of maximum exciton velocity.

The equations used in Chapter 3 to model indirect excitons in CQWs can also be used to model direct excitons in single QWs. This is done by using a very short ground state optical lifetime ($\tau_R = 25\,\mathrm{ps}$ was used in this case) and setting the mean-field energy, u_0, equal to zero, because the excitons are not dipole-oriented in the same direction. The same internal ring of PL was found for direct excitons, when their diffusion coefficient, $D_x = D_x^c = 100\,\mathrm{cm^2/s}$, and the focus of the laser beam was such that its intensity profile had a FWHM $\lesssim 2\,\mu\mathrm{m}$.

In Chapter 4, the trapping of excitons by a ring-shaped laser profile was discussed. This novel way of trapping indirect excitons takes advantage of the fact that they are all dipole-oriented in the same direction. The excitons' spatial profile created a trap with a potential minimum at $r_{\parallel} = 0$. Experiments and theoretical calculations were carried out for this trap, and in experiments, a concentration of $n_{2D}(r_{\parallel} = 0) = 4.7 \times 10^{10}\,\mathrm{cm^{-2}}$ was obtained. Theoretical calculations show that the exciton temperature at the centre of the trap, $T(r_{\parallel} = 0) \simeq T_b$, and that for the highest concentration obtained in the experiments, the occupation number of the ground state, $N_{E=0} \simeq 8$. This is a very small fraction of the number of excitons in the trap, but a much higher occupation number of the ground state was predicted for higher concentrations and/or lower lattice temperatures. The trap was modelled for $T_b = 0.4\,\mathrm{K}$ and $n_{2D}(r_{\parallel} = 0) = 3.65 \times 10^{10}\,\mathrm{cm^{-2}}$, and the occupation number of the ground state in this case was nearly 500, which is 0.35 % of the total number of excitons in the trap. Theoretical predictions for lower T_b were shown in Fig. 4.6, where $N_{E=0}$ is plotted against T_b. A very large fraction of the excitons in the trap would occupy the ground state at low

lattice temperatures, $T_b \lesssim 0.1\,\mathrm{K}$, and they would all eventually occupy the ground state as $T_b \to 0$.

REFERENCES

[1] G. Modugno, G. Ferrari, G. Roati, R. J. Brecha, A. Simoni and M. Inguscio. Bose-Einstein condensation of potassium atoms by sympathetic cooling. *Science*, **294**, 1320 (2001).

[2] A. V. Soroko, A. L. Ivanov and L. V. Butov. Thermalization and photoluminescence kinetics of statistically-degenerate indirect excitons in GaAs/AlGaAs coupled quantum wells. *Phys. stat. sol. (a)*, **190**, 719 (2002).

[3] L. V. Butov, A. Imamoglu, A. V. Mintsev, K. L. Campman and A. C. Gossard. Photoluminescence kinetics of indirect excitons in GaAs/Al$_x$Ga$_{1-x}$As coupled quantum wells. *Phys. Rev. B*, **59**, 1625 (1999).

[4] L. V. Butov, A. A. Shashkin, V. T. Dolgopolov, K. L. Campman and A. C. Gossard. Magneto-optics of the spatially separated electron and hole layers in GaAs/Al$_x$Ga$_{1-x}$As coupled quantum wells. *Phys. Rev. B*, **60**, 8753 (1999).

[5] L. V. Butov, A. C. Gossard and D. S. Chemla. Macroscopically ordered state in an exciton system. *Nature*, **418**, 751 (2002).

[6] C. E. Lai. *Spatially Indirect Excitons in Coupled Quantum Wells*. Ph.D. thesis, University of California, Berkeley (2004).

[7] W. Ketterle and N. J. van Druten. Bose-Einstein condensation of a finite number of particles trapped in one or three dimensions. *Phys. Rev. A*, **54**, 656 (1996).

[8] D. L. Mills. Ground-state occupancy of an ideal Bose-Einstein gas confined to a finite volume. *Phys. Rev.*, **134**, A306 (1963).

[9] D. L. Dexter and R. S. Knox. *Excitons* (John Wiley and Sons, New York, 1965).

[10] C. Weisbuch and B. Vinter. *Quantum Semiconductor Structures: Fundamentals and Applications* (Academic Press, Inc., 1991).

[11] J. M. Ziman. *Principles of the Theory of Solids* (Cambridge University Press, 1979).

[12] Y. E. Lozovik and I. V. Ovchinnikov. Controlling spatially indirect exciton condensate in coupled quantum wells by external fields and phonon laser. *Solid State Commun.*, **118**, 251 (2001).

[13] J. E. Golub, K. Kash, J. P. Haribson and L. T. Florez. Long-lived spatially indirect excitons in coupled GaAs/$Al_x Ga_{1-x}$As quantum wells. *Phys. Rev. B*, **41**, 8564 (1990).

[14] A. Alexandrou, J. A. Kash, E. E. Mendez, M. Zachau, J. M. Hong, T. Fukuzawa and Y. Hase. Electric-field effects on exciton lifetimes in symmetric coupled GaAs/$Al_{0.3} Ga_{0.7}$As double quantum wells. *Phys. Rev. B*, **42**, 9225 (1990).

[15] S. Charbonneau, M. L. W. Thewalt, E. S. Koteles and B. Elman. Transformation of spatially direct to spatially indirect excitons in coupled double quantum wells. *Phys. Rev. B*, **38**, 6287 (1988).

[16] A. V. Larionov, V. B. Timofeev, J. Hvam and K. Soerensen. Interwell excitons in GaAs/AlGaAs double quantum wells and their collective properties. *JETP*, **90**, 1093 (2000).

[17] A. L. Ivanov, P. B. Littlewood and H. Haug. Bose-Einstein statistics in thermalization and photoluminescence of quantum-well excitons. *Phys. Rev. B*, **59**, 5032 (1999).

[18] M. Levinshtein, S. Rumyantsev and M. Shur, editors. *Handbook Series on Semiconductor Properties (Vol. 1)* (World Science Publishing Co., Singapore, 1996).

[19] T. C. Damen, K. Leo, J. Shah and J. E. Cunningham. Spin relaxation and thermalization of excitons in GaAs quantum wells. *Appl. Phys. Lett.*, **58**, 1902 (1991).

[20] H. Zhao and H. Kalt. Direct measurement of acoustic-phonon scattering of hot quantum-well excitons. *Phys. Rev. B*, **69**, 233305 (2004).

[21] C. Piermarocchi, F. Tassone, A. Quattropani and P. Schwendimann. Nonequilibrium dynamics of free quantum-well excitons in time-resolved photoluminescence. *Phys. Rev. B*, **53**, 15834 (1996).

[22] W. Ketterle. Nobel lecture: When atoms behave as waves: Bose-Einstein condensation and the atom laser. *Rev. Mod. Phys.*, **74**, 1131 (2002).

[23] E. A. Cornell and C. E. Wieman. Nobel Lecture: Bose-Einstein condensation in a dilute gas, the first 70 years and some recent experiments. *Rev. Mod. Phys.*, **74**, 875 (2002).

[24] G. M. Kavoulakis. Bose-Einstein condensation of indirect excitons in coupled quantum wells. *J. Low Temp. Phys.*, **132**, 297 (2003).

[25] J. C. Kim and J. P. Wolfe. Bose-Einstein statistics of an excitonic gas in two dimensions: Excitons and biexcitons in a GaAs quantum well. *Phys. Rev. B*, **57**, 9861 (1998).

[26] A. Swarup and B. Cowan. Fermi-Bose correspondence and Bose-Einstein condensation in the two-dimensional ideal gas. *J. Low Temp. Phys.*, **134**, 881 (2004).

[27] B. G. Levich. *Theoretical Physics: An Advanced Text, Volume 4: Quantum Statistics and Physical Kinetics* (North-Holland Publishing Company, 1973).

[28] L. D. Landau and E. M. Lifshitz. *Statistical Physics Vol. 5: Course of Theoretical Physics* (Pergamon Press, 1980).

[29] M. H. Anderson, J. R. Ensher, M. R. Matthews, C. E. Wieman and E. A. Cornell. Observation of Bose-Einstein condensation in a dilute atomic vapour. *Science*, **269**, 198 (1995).

[30] C. C. Bradley, C. A. Sackett, J. J. Tollet and R. G. Hulet. Evidence of Bose-Einstein condensation in an atomic gas with attractive interactions. *Phys. Rev. Lett.*, **75**, 1687 (1995).

[31] K. B. Davis, M. O. Mewes, M. A. Joffe, M. R. Andrews and W. Ketterle. Evaporative cooling of sodium atoms. *Phys. Rev. Lett.*, **74**, 5202 (1995).

[32] A. Griffin, D. W. Snoke and S. Stringari, editors. *Bose-Einstein Condensation* (Cambridge University Press, 1995).

[33] T. Weber, J. Herbig, M. Mark, H. C. Nägerl and R. Grimm. Bose-Einstein condensation of cesium. *Science*, **299**, 232 (2003).

[34] D. G. Fried, T. C. Killian, L. Willmann, D. Landhuis, S. C. Moss, D. Kleppner and T. J. Greytak. Bose-Einstein condensation of atomic hydrogen. *Phys. Rev. Lett.*, **81**, 3811 (1998).

[35] A. Ashkin. Acceleration and trapping of particles by radiation pressure. *Phys. Rev. Lett.*, **24**, 156 (1970).

[36] T. Kuga, Y. Torii, N. Shiokawa, T. Hirano, Y. Shimizu and H. Sasada. Novel optical trap of atoms with a doughnut beam. *Phys. Rev. Lett.*, **78**, 4713 (1997).

[37] D. M. Stamper-Kurn, M. R. Andrews, A. P. Chikkatur, S. Inouye, H. J. Miesner, J. Stenger and W. Ketterle. Optical confinement of a Bose-Einstein condensate. *Phys. Rev. Lett.*, **80**, 2027 (1998).

[38] H. Ott, J. Fortagh, G. Schlotterbeck, A. Grossmann and C. Zimmermann. Bose-Einstein condensation in a surface microtrap. *Phys. Rev. Lett.*, **87**, 230401 (2001).

[39] S. A. Moskalenko. Reversible optico-hydrodynamic phenomena in a nonideal exciton gas. *Fiz. Tverd. Tela*, **4**, 276 (1962).

[40] J. M. Blatt, K. W. Böer and W. Brandt. Bose-Einstein condensation of excitons. *Phys. Rev.*, **126**, 1691 (1962).

[41] L. V. Keldysh and A. N. Kozlov. Collective properties of excitons in semiconductors. *Sov. Phys. JETP*, **27**, 521 (1968).

[42] L. V. Butov, C. W. Lai, A. L. Ivanov, A. C. Gossard and D. S. Chemla. Towards Bose-Einstein condensation of excitons in potential traps. *Nature*, **417**, 47 (2002).

[43] D. Hulin, A. Mysyrowciz and C. B. à la Guillaume. Evidence for Bose-Einstein statistics in an exciton gas. *Phys. Rev. Lett.*, **45**, 1970 (1980).

[44] D. Snoke, J. P. Wolfe and A. Mysyrowicz. Quantum saturation of a Bose gas: Excitons in Cu_2O. *Phys. Rev. Lett.*, **59**, 827 (1987).

[45] D. W. Snoke, J. P. Wolfe and A. Mysyrowicz. Evidence for Bose-Einstein condensation of a two-component exciton gas. *Phys. Rev. Lett.*, **64**, 2543 (1990).

[46] M. Hasuo, N. Nagasawa, T. Itoh and A. Mysyrowicz. Progress in the Bose-Einstein condesation of biexcitons in CuCl. *Phys. Rev. Lett.*, **70**, 1303 (1993).

[47] E. Fortin, S. Fafard and A. Mysyrowicz. Exciton transport in Cu_2O: Evidence for excitonic superfluidity? *Phys. Rev. Lett.*, **70**, 3951 (1993).

[48] T. Goto, M. Y. Shen, S. Koyama and T. Yokouchi. Bose-Einstein statistics of orthoexcitons generated by two-photon resonant absorption in cuprous oxide. *Phys. Rev. B*, **55**, 7609 (1997).

[49] G. M. Kavoulakis, G. Baym and J. P. Wolfe. Quantum saturation and condensation of excitons in Cu_2O: A theoretical study. *Phys. Rev. B*, **53**, 7227 (1996).

[50] G. M. Kavoulakis and A. Mysyrowicz. Auger decay, spin exchange, and their connection to Bose-Einstein condensation of excitons in Cu_2O. *Phys. Rev. B*, **61**, 16619 (2000).

[51] M. Kuwata-Gonokami, M. Kubouchi, R. Shimano and A. Mysyrowicz. Time-resolved excitonic Lyman spectroscopy of Cu_2O. *J. Phys. Soc. Japan*, **73**, 1065 (2003).

[52] K. Johnsen and G. M. Kavoulakis. Bose-Einstein condensation of excitons with electromagnetic radiation. *Phys. Rev. Lett.*, **86**, 858 (2001).

[53] M. Nagai, R. Shimano, K. Horiuchi and M. Kuwata-Gonokami. Creation of supercooled exciton gas and transformation to electron-hole droplets in diamond. *Phys. Rev. B*, **68**, 081202(R) (2003).

[54] C. Ell, A. L. Ivanov and H. Haug. Relaxation kinetics of a low-density exciton gas in Cu_2O. *Phys. Rev. B*, **57**, 9663 (1998).

[55] A. L. Ivanov, C. Ell and H. Haug. Phonon-assisted Boltzmann kinetics of a Bose gas: Generic solution for $T \leq T_c$. *Phys. Rev. E*, **55**, 6363 (1997).

[56] J. P. Wolfe and J. I. Jang. New perspectives on kinetics of excitons in Cu_2O. *Solid State Commun.*, **134**, 143 (2005).

[57] K. E. O'Hara, L. O. Súilleábhain and J. P. Wolfe. Strong non-radiative recombination of excitons in Cu_2O and its impact on Bose-Einstein statistics. *Phys. Rev. B*, **60**, 10565 (1999).

[58] V. Bagnato and D. Kleppner. Bose-Einstein condensation in low-dimensional traps. *Phys. Rev. A*, **44**, 7439 (1991).

[59] A. Görlitz, J. M. Vogels, A. E. Leanhardt, C. Raman, T. L. Gustavson, J. R. Abo-Shaeer, A. P. Chikkatur, S. Gupta, S. Inouye, T. Rosenband and W. Ketterle. Realization of Bose-Einstein condensates in lower dimensions. *Phys. Rev. Lett.*, **87**, 130402 (2001).

[60] M. F. M. Osborne. The Bose-Einstein condensation for thin films. *Phys. Rev.*, **76**, 396 (1949).

[61] D. S. Petrov, M. Holzmann and G. V. Shlyapnikov. Bose-Einstein condensation in quasi-2D trapped gases. *Phys. Rev. Lett.*, **84**, 2551 (2000).

[62] W. J. Mullin. A study of Bose-Einstein condensation in a two-dimensional trapped gas. *J. Low Temp. Phys.*, **110**, 167 (1998).

[63] R. M. May. Quantum statistics of ideal gases in two dimensions. *Phys. Rev.*, **135**, A1515 (1964).

[64] L. V. Butov, A. L. Ivanov, A. Imamoglu, P. B. Littlewood, A. A. Shashkin, V. T. Dolgopolov, K. L. Campman and A. C. Gossard. Stimulated scattering of indirect excitons in coupled quantum wells: signature of a degenerate Bose-gas of excitons. *Phys. Rev. Lett.*, **86**, 5608 (1998).

[65] V. Negoita, D. W. Snoke and K. Eberl. Huge density-dependent blueshift of indirect excitons in biased coupled quantum wells. *Phys. Rev. B*, **61**, 2779 (2000).

[66] A. V. Larionov, V. B. Timofeev, J. Hvam and C. Soerensen. Collective behavior of interwell excitons in GaAs/AlGaAs double quantum wells. *JETP Lett.*, **75**, 200 (2002).

[67] A. V. Larionov, V. B. Timofeev, J. Hvam and K. Soerensen. Collective state of interwell excitons in GaAs/AlGaAs double quantum wells under pulse resonance excitation. *JETP Letters*, **75**, 200 (2002).

[68] D. Snoke, S. Denev, Y. Liu, L. Pfeiffer and K. West. Long-range transport in excitonic dark states in coupled quantum wells. *Nature*, **418**, 754 (2002).

[69] Y. Naveh and B. Laikhtman. Excitonic instability and electric-field-induced phase transition towards a two-dimensional exciton condensate. *Phys. Rev. Lett.*, **77**, 900 (1996).

[70] V. Negoita, D. W. Snoke and K. Eberl. Harmonic-potential traps for indirect excitons in coupled quantum wells. *Phys. Rev. B*, **60**, 2661 (1999).

[71] V. Negoita, D. W. Snoke and K. Eberl. Stretching quantum wells: A method for trapping free carriers in gaas heterostructures. *Appl. Phys. Lett.*, **75**, 2059 (1999).

[72] R. Rapaport, G. Chen, S. Simon, O. Mitrofanov, L. Pfeiffer and P. M. Platzman. Electrostatic traps for dipolar excitons. *Phys. Rev. B*, **72**, 075428 (2005).

[73] A. T. Hammack, N. A. Gippius, G. O. Andreev, L. V. Butov, M. Hanson and A. C. Gossard. Excitons in electrostatic traps. *J. Appl. Phys.*, **99**, 066104 (2006).

[74] A. Schmeller, W. Hansen, J. P. Kotthaus, G. Tränkle and G. Weimann. Franz-keldysh effect in a two-dimensional system. *Appl. Phys. Lett.*, **64**, 330 (1993).

[75] S. Zimmermann, A. O. Govorov, W. Hansen, J. P. Kotthaus, M. Bichler and W. Wegscheider. Lateral superlattices as voltage-controlled traps for excitons. *Phys. Rev. B*, **56**, 13414 (1997).

[76] S. Zimmermann, G. Schedelbeck, A. O. Govorov, A. Wixforth, J. P. Kotthaus, M. Bichler, W. Wegscheider and G. Abstreiter. Spatially resolved exciton trapping in a voltage-controlled lateral superlattice. *Appl. Phys. Lett.*, **73**, 154 (1998).

[77] M. Hagn, A. Zrenner, G. Böhm and G. Weimann. Electric-field-induced exciton transport in coupled quantum well structures. *Appl. Phys. Lett.*, **67**, 232 (1995).

[78] A. Parlangeli, P. C. M. Christianen, J. C. Maan, I. V. Tokatly, C. B. Soerensen and P. E. Lindelof. Optical observation of the energy-momentum dispersion of spatially indirect excitons. *Phys. Rev. B*, **62**, 15323 (2000).

[79] Y. E. Lozovik, L. V. Ovchinnikov, S. Y. Volkov, L. V. Butov and D. S. Chemla. Quasi-two-dimensional excitons in finite magnetic fields. *Phys. Rev. B*, **65**, 235304 (2002).

[80] N. E. Kaputkina and Y. E. Lozovik. Two-dimensional exciton with spatially-separated carriers in coupled quantum wells in external magnetic fields. *Physica E*, **12**, 323 (2002).

[81] M. Orlita, R. Grill, M. Zvára, G. H. Döhler, S. Malzer, M. Byszewski and J. Soubusta. Luminescence of coupled quantum wells: Effects of indirect excitons in high in-plane magnetic fields. *Phys. Rev. B*, **70**, 075309 (2004).

[82] S. A. Moskalenko, M. A. Liberman, D. W. Snoke, V. V. Boţan and B. Johansson. Bose-Einstein condensation of excitons in ideal two-dimensional system in a strong magnetic field. *Physica E*, **19**, 278 (2003).

[83] L. V. Butov, C. W. Lai, D. S. Chemla, Y. E. Lozovik, K. L. Campman and A. C. Gossard. Observation of magnetically induced effective-mass enhancement of quasi-2D excitons. *Phys. Rev. Lett.*, **87**, 216804 (2001).

[84] L. V. Butov, A. V. Mintsev, Y. E. Lozovik, K. L. Campman and A. C. Gossard. From spatially indirect excitons to momentum-space indirect excitons by an in-plane magnetic field. *Phys. Rev. B*, **62**, 1548 (2000).

[85] D. Yoshioka and A. H. Macdonald. Double quantum well electron-hole systems in strong magnetic fields. *J. Phys. Soc. Japan*, **59**, 4211 (1990).

[86] S. B.-T. de Leon and B. Laikhtman. Exciton-exciton interactions in quantum wells: Optical properties and energy spin relaxation. *Phys. Rev. B*, **63**, 125306 (2001).

[87] A. L. Ivanov. Quantum diffusion of dipole-oriented indirect excitons in coupled quantum wells. *Europhys. Lett.*, **59**, 586 (2002).

[88] L. V. Butov. Condensation and pattern formation in cold exciton gases in coupled quantum wells. *J. Phys.: Condens. Matter*, **16**, R1577 (2004).

[89] J. Lee, E. S. Koteles and M. O. Vassell. Luminescence linewidths of excitons in GaAs quantum wells below 150 K. *Phys. Rev. B*, **33**, 5512 (1986).

[90] U. Bockelmann. Phonon scattering between zero-dimensional electronic states: Spatial versus Landau quantization. *Phys. Rev. B*, **50**, 17271 (1994).

[91] P. Stenius and A. L. Ivanov. Relaxation kinetics of quasi two-dimensional excitons coupled to a bath of bulk acoustic phonons. *Solid State Commun.*, **108**, 117 (1998).

[92] A. V. Soroko and A. L. Ivanov. Phonon-assisted relaxation kinetics of statistically degenerate excitons in high-quality quantum wells. *Phys. Rev. B*, **65**, 165310 (2002).

[93] M. Neuberger. *III-V Semiconducting compounds* (Plenum, New York, 1971).

[94] L. R. Weisberg and J. Blanc. Measurements of the density of gaas. *J. Appl. Phys.*, **34**, 1002 (1963).

[95] L. C. Andreani, F. Tassone and F. Bassani. Radiative lifetime of free excitons in quantum wells. *Solid State Commun.*, **77**, 641 (1991).

[96] P. Roussignol, C. Delalande, A. Vinattieri, L. Carraresi and M. Colocci. Dynamics of exciton relaxation in $GaAs/Al_xGa_{1-x}As$ quantum wells. *Phys. Rev. B*, **45**, 6965 (1992).

[97] M. H. Zhang, Q. Huang and J. M. Zhou. Calculations of the time taken for excitons to form in GaAs quantum wells. *J. Phys.: Condens, Matter*, **9**, 10185 (1997).

[98] H. W. Yoon, D. R. Wake and J. P. Wolfe. Effect of exciton-carrier thermodynamics on the GaAs quantum well photoluminescence. *Phys. Rev. B*, **54**, 2763 (1996).

[99] J. Kusano, Y. Segawa, Y. Aoyagi, S. Namba and H. Okamoto. Extremely slow energy relaxation of a two-dimensional exciton in a GaAs superlattice structure. *Phys. Rev. B*, **40**, 1685 (1989).

[100] T. C. Damen, J. Shah, D. Y. Oberli, D. S. Chemla, J. E. Cunningham and J. M. Kuo. Dynamics of exciton formation and relaxation in GaAs quantum wells. *Phys. Rev. B*, **42**, 7434 (1990).

[101] P. W. M. Blom, P. J. van Hall, C. Smit and J. P. C. andJ H Wolter. Selective exciton formation in thin $GaAs/Al_xGa_{1-x}As$ quantum wells. *Phys. Rev. Lett.*, **71**, 3878 (1993).

[102] D. Robart, X. Marie, B. Baylac, T. Amand, M. Brousseau, G. Bacquet, G. Debart, R. Planel and J. M. Gerard. Dynamical equilibrium bewteen excitons and free carriers in quantum wells. *Solid State Commun.*, **95**, 287 (1995).

[103] R. Kumar, A. S. Vengurlekar, S. S. Prabhu, J. Shah and L. N. Pfeiffer. Picosecond time evolution of free electron-hole pairs into excitons in GaAs quantum wells. *Phys. Rev. B*, **54**, 4891 (1996).

[104] A. Thilagam and J. Singh. Generation rate of 2D excitons in quantum wells. *J. Lumin.*, **55**, 11 (1993).

[105] I. K. Oh and J. Singh. Formation of excitons from free electron-hole pairs due to acoustic phonon interactions in quantum wells. *Superlattices Microstruct.*, **30**, 221 (2001).

[106] J. Szczytco, L. Kappei, J. Berney, F. Morier-Genoud, M. T. Portella-Oberli and B. Deveaud. Determination of the exciton formation in quantum wells from time-resolved interband luminescence. *Phys. Rev. Lett.*, **93**, 137401 (2004).

[107] J. Szczytco, L. Kappei, F. Morier-Genoud, T. Guillet, M. T. Portella-Oberli and B. Deveaud. Excitons or free carriers? That is the question. *Phys. stat. sol. (c)*, **1**, 493 (2004).

[108] D. P. Trauernicht, J. P. Wolfe and A. Mysyrowicz. Highly mobile paraexcitons in cuprous oxide. *Phys. Rev. Lett.*, **52**, 855 (1984).

[109] M. A. Tamor and J. P. Wolfe. Drift and diffusion of free excitons in Si. *Phys. Rev. Lett.*, **44**, 1703 (1980).

[110] D. P. Trauernicht and J. P. Wolfe. Drift and diffusion of paraexcitons in Cu_2O: Deformation-potential scattering in the low-temperature regime. *Phys. Rev. B*, **33**, 8506 (1986).

[111] U. Bockelmann, G. Abstreiter, G. Weimann and W. Schlapp. Single-particle and transport scattering times in narrow $GaAs/Al_xGa_{1-x}As$ quantum-wells. *Phys. Rev. B*, **41**, 7864 (1990).

[112] H. Sakaki, T. Noda, K. Hirakawa, M. Tanaka and T. Matsusue. Interface roughness scattering in GaAs/AlAs quantum wells. *Appl. Phys. Lett.*, **51**, 1934 (1987).

[113] A. Gold. Electronic transport properties of a two-dimensional electron gas in a silicon quantum-well structure at low temperature. *Phys. Rev. B*, **35**, 723 (1987).

[114] B. Vinter. Low-temperature phonon-limited electron mobility in modulation-doped heterostructures. *Phys. Rev. B*, **33**, 5904 (1985).

[115] E. E. Mendez, P. J. Price and M. Heiblum. Temperature dependence of the electron mobility in GaAs-AlGaAs heterostuctures. *Appl. Phys. Lett.*, **45**, 294 (1984).

[116] H. Wang, M. Jiang and D. G. Steel. Measurement of phonon-assisted migration of localized excitons in GaAs/AlGaAs multiple-quantum-well stuctures. *Phys. Rev. Lett.*, **65**, 1255 (1990).

[117] H. W. Yoon, D. R. Wake, J. P. Wolfe and H. Morkoç. In-plane transport of photoexcited carriers in GaAs quantum wells. *Phys. Rev. B*, **46**, 13461 (1992).

[118] D. Oberhauser, K. H. Pantke, J. M. Hvam, G. Weimann and C. Klingshirn. Exciton scattering in quantum wells at low temperatures. *Phys. Rev. B*, **47**, 6827 (1993).

[119] G. D. Gilliland, M. S. Petrovic, H. P. Hjalmarson, D. J. Wolford, G. A. Northrop, T. F. Kuech, L. M. Smith and J. A. Bradley. Time-dependent heterointerfacial band bending and quasi-two-dimensional excitonic transport in GaAs structures. *Phys. Rev. B*, **58**, 4728 (1998).

[120] M. Achermann, B. A. Nechay, F. Morier-Genoud, A. Schertel, U. Siegner and U. Keller. Direct experimental observation of different diffusive transport regimes in semiconductor nanostructures. *Phys. Rev. B*, **60**, 2101 (1999).

[121] H. Zhao, S. Moehl, S. Wachter and H. Kalt. Hot exciton transport in ZnSe quantum wells. *Appl. Phys. Lett.*, **80**, 1391 (2002).

[122] H. Zhao, B. D. Don, S. Moehl and H. Kalt. Spatiotemporal dynamics of quantum-well excitons. *Phys. Rev. B*, **67**, 035306 (2003).

[123] Z. Vörös, R. Balili, D. W. Snoke, L. Pfeiffer and K. West. Long-distance diffusion of excitons in double quantum well structures. *Phys. Rev. Lett.*, **94**, 226401 (2005).

[124] R. Rapaport, G. Chen and S. H. Simon. Nonlinear dynamics of a dense two-dimensional dipolar exciton gas (2005). *cond-mat/0508203*.

[125] J. Hegarty, L. Goldner and M. D. Sturge. Localized and delocalized two-dimensional excitons in GaAs/AlGaAs multiple-quantum-well structures. *Phys. Rev. B*, **30**, R7346 (1984).

[126] F. Martelli, A. Polimeni, A. Patanè, M. Capizzi, P. Borri, M. Gurioli, M. Colocci, A. Bosacchi and S. Franchi. Exciton localization by potential fluctuations at the interface of InGaAs/GaAs quantum wells. *Phys. Rev. B*, **53**, 7421 (1996).

[127] G. Bastard, C. Delalande, M. H. Meynadier, P. M. Frijlink and M. Voos. Low-temperature exciton trapping on interface defects in semiconductor quantum wells. *Phys. Rev. B*, **29**, 7042 (1984).

[128] M. Zachau, J. A. Kash and T. Masselink. Relaxation of excitons in thin quantum wells. *Phys. Rev. B*, **44**, 8403 (1991).

[129] H. Hillmer, A. Forchel, S. Hansmann, M. Morohashi, E. Lopez, H. P. Meier and K. Ploog. Optical investigations on the mobility of two-dimensional excitons in $GaAs/Ga_{1-x}Al_xAs$ quantum wells. *Phys. Rev. B*, **39**, 10901 (1989).

[130] H. Tang. Influence of interface roughness on excitonic diffusion in semiconductor quantum well. *J. Phys.: Condens. Matter*, **15**, 8137 (2003).

[131] L. Schrottke, H. T. Grahn and K. Fujiwara. Excitonic properties of weakly coupled gaas single quantum wells investigated with high-resolution photoluminescence excitation spectroscopy. *Phys. Rev. B*, **56**, 13321 (1997).

[132] S. D. Baranovskii, R. Eichmann and P. Thomas. Temperature-dependent exciton luminescence in quantum wells by computer simulation. *Phys. Rev. B*, **58**, 13081 (1998).

[133] P. J. Price. Two-dimensional electron transport in semiconductor layers, 1. Phonon scattering. *Ann. Phys.*, **133**, 217 (1981).

[134] G. Woan. *The Cambridge Handbook of Physics Formulas* (Cambridge University Press, 2000).

[135] A. L. Ivanov. Thermalization and photoluminescence dynamics of indirect excitons at low bath temperatures. *J. Phys.: Condens. Matter*, **16**, S3629 (2004).

[136] L. V. Butov, A. L. Ivanov, A. Imamoglu, P. B. Littlewood, A. A. Shashkin, V. T. Dolgopolov, K. L. Campman and A. C. Gossard. Stimulated scattering of indirect excitons in coupled quantum wells: Signature of a degenerate Bose-gas of excitons. *Phys. Rev. Lett.*, **86**, 5608 (2001).

[137] D. Snoke. Spontaneous Bose coherence of excitons and polaritons. *Science*, **298**, 1368 (2002).

[138] R. Rapaport, G. Chen, D. Snoke, S. H. Simon, L. Pfeiffer, K. West, Y. Liu and S. Denev. Charge separation of dense two-dimensional electron-hole gases: mechanism for exciton ring pattern formation. *Phys. Rev. Lett.*, **92**, 117405 (2004).

[139] M. H. Szymanska and P. B. Littlewood. Excitonic binding in coupled quantum wells. *Phys. Rev. B*, **67**, 193305 (2003).

[140] L. V. Butov, L. S. Levitov, A. V. Mintsev, B. D. Simons, A. C. Gossard and D. S. Chemla. Formation mechanism and low-temperature instability of exciton rings. *Phys. Rev. Lett.*, **92**, 117404 (2004).

[141] D. Snoke, Y. Liu, S. Denev, L. Pfeiffer and K. West. Luminescence rings in quantum well structures. *Solid State Commun.*, **127**, 187 (2003).

[142] D. Snoke, S. Denev, Y. Liu, S. Simon, R. Rapaport, G. Chen, L. Pfeiffer and K. West. Moving beyond a simple model of luminescence rings in quantum well structures. *J. Phys.: Condens. Matter*, **16**, S3621 (2004).

[143] S. Denev, S. H. Simon and D. W. Snoke. Luminescence ring formation in quantum wells – a model with Coulomb interaction. *Solid State Commun.*, **134**, 59 (2005).

[144] G. Chen, S. H. Simon, L. Pfeiffer and K. West. Dynamics of the in-plane charge separation front in a two-dimensional electron-hole gas. *Phys. Rev. B*, **71**, 041301 (2005).

[145] L. V. Butov. *Unpublished* (2005).

[146] A. L. Ivanov, L. E. Smallwood, A. T. Hammack, S. Yang, L. V. Butov and A. C. Gossard. Origin of the inner ring in photoluminescence patterns of quantum well excitons. *Europhys. Lett.*, **73**, 920 (2006).

[147] L. E. Smallwood and A. L. Ivanov. Photoluminescence and in-plane diffusion of indirect excitons. *Phys. stat. sol. (c)*, **2**, 3932 (2005).

[148] R. Eccleston, R. Strobel, W. W. Rühle, J. Kuhl, B. F. Feuerbacher and K. Ploog. Exciton dynamics in a GaAs quantum well. *Phys. Rev. B*, **3**, 1395 (1991).

[149] A. Ashkin. Trapping of atoms by resonance radiation pressure. *Phys. Rev. Lett.*, **40**, 729 (1978).

[150] W. D. Phillips. Laser cooling and trapping of neutral atoms. *Rev. Mod. Phys.*, **70**, 721 (1998).

[151] C. N. Cohen-Tannoudji. Manipulating atoms with photons. *Rev. Mod. Phys.*, **70**, 707 (1998).

[152] S. Chu. The manipulation of neutral particles. *Rev. Mod. Phys.*, **70**, 685 (1998).

[153] A. Ashkin. History of optical trapping and manipulation of small-neutral particle, atoms and molecules. *IEEE J. Sel. Topics Quantum Electron.*, **6**, 841 (2000).

[154] A. T. Hammack, M. Griswold, L. V. Butov, L. E. Smallwood, A. L. Ivanov and A. C. Gossard. Trapping of cold excitons in quantum well structures with laser light (2006). *cond-mat/0603597*.

[155] S. Grossmann and M. Holthaus. λ-transition to the Bose-Einstein condensate. *Z. Naturforsch.*, **50a**, 921 (1995).